SISSA

SCUOLA INTERNAZIONALE
SUPERIORE di STUDI AVANZATI
International School
for Advanced Studies

Spectral And Dynamical Properties Of Strongly Correlated Systems

Methods And Applications

Candidate
Giuseppe Carleo

Advisors
Prof. Stefano Baroni
Dr. Federico Becca
Dr. Saverio Moroni

Thesis submitted for the Degree of *Doctor Philosophiæ*
October 2011

Contents

Introduction 5

Part I Imaginary-Time Dynamics
Equilibrium Properties

1 The Imaginary-Time Connection
A Stochastic Bridge Between the Classical and the Quantum Worlds 13
- 1.1 Classical Diffusion and Quantum Mechanics 13
  - 1.1.1 Fokker-Planck Equation 14
  - 1.1.2 The Classical-Quantum Mapping 15
  - 1.1.3 Classical Stochastic Dynamics of a Quantum Problem 16
- 1.2 Path-Integrals 18
- 1.3 Exact Properties of Quantum Systems 20
  - 1.3.1 Ground-state Expectation Values 21
  - 1.3.2 Static Response Functions 22
  - 1.3.3 Correlations in Imaginary-Time and Spectral Functions 23
  - 1.3.4 Analytical Continuation and Maximum Entropy Method 24
- 1.4 Perturbative Expansions for the Imaginary-Time Evolution 25
  - 1.4.1 The Dyson Series 26
  - 1.4.2 Path-Integrals and Rayleigh-Schrödinger Perturbation Theory 27

2 Sampling Imaginary-Time Paths
Reptation Monte Carlo for Lattice Hamiltonians 29
- 2.1 General Formalism 30
- 2.2 Reptation Quantum Monte Carlo 32
  - 2.2.1 Directed Updates 34
  - 2.2.2 Continuous-Time Propagator 36
  - 2.2.3 Non-Diagonal Observables 36

2.2.4 Fixed-Node Approximation and Systematic Improvements 40
2.3 Case Studies 42
2.3.1 Low-Energy Excitations and Spin Correlations of the Heisenberg Model . 42
2.3.2 Ground-State Properties of the Fermionic Hubbard Model 45
2.4 Conclusions 46

3 Quantum Spectral Properties From Imaginary-Time Dynamics
Lattice Dynamics of Helium 4 49
3.1 Lattice Dynamics 50
3.1.1 Long Wave-Lengths 50
3.1.2 Shorter Wave-Lengths 51
3.2 Numerical Methods 53
3.3 Results 55
3.3.1 Long Wave-length Excitations 55
3.3.2 Intermediate Wave-length Excitations 60
3.4 Concluding Remarks 63

4 Exact Fermionic Properties From Spectral Functions
The Itinerant Ferromagnetic Phase of the Hubbard Model 65
4.1 Fermionic-Correlations Method 66
4.2 A Model for Itinerant Ferromagnetism 67
4.3 Ground-State Phase Diagram 68
4.3.1 Back-Flow Variational Wave Function 68
4.3.2 Infinite-Order Phase Transition 72
4.4 Effect of a Density Interaction 73
4.5 Conclusions 74

5 Finite-Temperature Susceptibilities
Bose-Einstein Condensation in Quantum Glasses 77
5.1 Finite-Temperature Methods for Strongly Correlated Systems 78
5.1.1 Stochastic Sampling of the Canonical Partition Function 78
5.1.2 The Quantum Cavity Method 80
5.2 Quantum Glasses, Localization and the Superglass Phase 80
5.3 A Model for the Superglass Phase and the Role of Frustration 82
5.3.1 Results 84
5.4 Ground-State Degeneracy and Spin-Glass Nature 86
5.5 Conclusions 87

Part II Real Time Dynamics
Out-of-Equilibrium Properties

6 Exact Dynamics After A Quantum Quench
Localization and Glassy Dynamics of Many-Body Quantum Systems 91
- 6.1 Exact Methods for the Quantum Dynamics 93
  - 6.1.1 Series Expansion for the Schrödinger Evolution 93
  - 6.1.2 Time-Evolving Block Decimation 94
  - 6.1.3 Lanczos Basis 95
- 6.2 The Bose-Hubbard Model 97
- 6.3 Inhomogeneous Initial States and Dynamical Localization 98
  - 6.3.1 Lanczos-Basis Analysis 100
  - 6.3.2 Lanczos-Basis Analysis of an Integrable Model 101
  - 6.3.3 Inhomogeneous States Dynamics at $n = 2/3$ 102
- 6.4 Homogeneous Initial States and Quantum Quenches 104
- 6.5 Discussion 105

7 Time-Dependent Variational Monte Carlo
Non-Thermal Behavior of the Bose-Hubbard Model After a Quench 107
- 7.1 Time-Dependent Ground states 109
- 7.2 Real-Time Evolution of the Variational Parameters 111
  - 7.2.1 Minimal Hilbert Space Distance 111
  - 7.2.2 Variational Principle 114
  - 7.2.3 Norm and Energy Conservation 115
  - 7.2.4 Real-Time Variational Monte Carlo 116
- 7.3 Examples of Exactly Solvable Quantum Dynamics 118
  - 7.3.1 Harmonic Oscillator 118
  - 7.3.2 Tomonaga-Luttinger Liquid 119
- 7.4 Quantum Quenches in the Bose-Hubbard Model 121
  - 7.4.1 Gutzwiller Wave Function 122
  - 7.4.2 Jastrow Wave Function 123
- 7.5 Two-Dimensional Systems 127
- 7.6 Discussion 128

Epilogue 131

Acknowledgements 135

References 137

A Directed Updates Probabilities And Efficiency Of The Lattice Reptation Monte Carlo 147
A.1 Derivation of the Probabilities for the Directed-Update Scheme 147
A.2 Bounce Algorithm, Directed Updates, and Efficiency 149

Introduction

Advancing Numerical Methods for Strong Correlations

Strongly interacting quantum systems constitute physical prototypes in which unexpected macroscopic phenomena emerge. These phenomena stem from many particles experiencing very well known interactions—mainly of electrostatic nature—and influenced by quanto-mechanical correlations. Noticeable behaviors largely due to quantum correlations are the high-temperature superconductivity in cuprates,[13] and the emergence of unconventional localized magnetic moments in fermionic systems.[3] The study of the physical mechanisms inducing such unconventional properties is a fundamental task of both theoretical and technological importance. The discovery and the engineering of new materials is indeed bound to a mature understanding and control of the effects of correlations.

Much of the dedicated theoretical analysis concerns the search for some universal, system-independent, macroscopic traits and their rationalization in terms of minimal models. An example of this process is the study of the quantum phases of the Hubbard model—the archetypal model for correlations, believed to describe the impressive phenomenon of high-Tc superconductivity. [4] Despite the microscopic simplicity of these models, a complete characterization of their properties is a challenging program to be pursued. The elusive manifestations of strong correlations are indeed poorly described or even completely missed by approximate theoretical approaches and specifically devised treatments have to be envisaged. In the last years, advances in this direction have been twofold, both in the *experimental* and in the *numerical* simulation of correlated models.

On the experimental side, the impressive advances in the manipulation of cold atoms are allowing for a controlled study of the effects of quantum correlations. The possibility to artificially engineer the prototypical models for correlations and the ability to probe their properties is indeed giving a new momentum to the clarification of long-debated problems in condensed-matter physics and fundamental questions on quantum coherence. [21]

On the theoretical side, the numerical simulation of quantum many-body systems is benefiting from a continuous progress in both the algorithmic methods and the computational resources available. Its traditional role as an essential tool in the research on quantum correlations has therefore been consolidated. However, the very mathematical foundations of quantum Mechanics still pose serious restrictions on the current possibility to treat, without approximations, many relevant problems. Whereas exact ground-state properties of bosons can be accurately studied in any dimensionality, exact ground-state properties of fermions in more than one dimension are currently out of the scope of existing methods. Serious limitations exist also in the study of excited-states and dynamical properties of correlated models. These methodological issues constitute, for many respects, the major unsolved problems in modern quantum computational physics and hinder a complete understanding of the physics of strong correlations.

A large part of this Thesis is dedicated to the introduction and extension of suitable numerical methodologies aimed to these traditionally hard problems. In particular, we focus on the development of novel quantum Monte Carlo methods and their application to models of strong correlations. The resulting schemes we introduce provide reliable and accurate answers to specific problems which have been previously biased by the nature of the approximate approaches adopted.

Quantum Monte Carlo methods are amongst the few available methods able to treat without approximations a large class of quantum systems. In particular, the existence of a deep connection between quantum mechanics and classical stochastic mechanics allows to map (and solve) a complex quantum problem of bosons into a corresponding classical stochastic problem. The application of Quantum Monte Carlo methods to bosonic problems at the equilibrium is therefore a well consolidated achievement of modern computational physics. [36, 54] However, numerous problems have to be faced when trying to extend these methodologies to other relevant systems. In particular, unveiling excited states properties of strongly correlated materials is a task of prime importance in which suitable computational schemes should succeed. Excited state properties are greatly relevant both to make a contact with experimental measurements and for the advancement of a general theoretical understanding of high energy processes.

In this Thesis we show how experimentally relevant spectral features can be extracted from the imaginary-time dynamics of a quantum system. This program is pursued by means of both a novel quantum Monte Carlo method for systems with discrete spatial degrees of freedom and a combination of other existing techniques. As applications of these ideas, we have studied the density excitations of Helium crystals at zero-temperature[33] thus obtaining, for the first time *ab-initio,* complete phonon dispersions in excellent agreement with experimental results. Our study of the surprising phenomenon of Bose-Einstein condensation in quantum glasses [35] constitutes a further physically relevant application of the imaginary-time dynamics. In the latter case, we have introduced and validated a theoretical mechanism for the existence of a super-glass phase. The experimental observation of this novel phase of matter with cold atoms is an intriguing possibility which our study has put forward.

Another major source of challenges for modern computational methods is the study of systems with fermionic statistics. In this case, the stochastic connection breaks down and, at variance with bosons, often uncontrolled *approximations* need to be introduced in their simulation. Fermions do however constitute a substantial part of the matter surrounding us and the description of most phenomena due to strong correlation suffers from the approximations needed in their numerical study. Advances in this direction should therefore concern both the improvement of the existing approximate schemes and the introduction of unbiased novel tools. In this Thesis relevant steps in both directions have been undertaken. As for the advancement of existing approximations, we have introduced a scheme to systematically improve upon the so-called *fixed-node* approximation by means of the Hamiltonian moments.[30] Whereas, as for the introduction of novel unbiased schemes for fermions, we have exploited the spectral properties of an auxiliary bosonic system in order to infer exact ground-state, equilibrium properties of corresponding strongly interacting fermions.[34] In the latter case we have been able to characterize with unprecedented accuracy one of the most debated phases of the Hubbard model, namely the ferromagnetic order in the large interaction limit. Within our study we have established the stability of a purely itinerant saturated ferromagnetism accompanied by an unexpected phase transition of infinite-order.

A possibly even more challenging field of application for numerical methods to physically relevant quantum problems is to be found in the context of the out-of-equilibrium dynamics. At variance with the huge momentum towards the improvement of the numerical simulation of systems at equilibrium, in this case the lack of a stochastic connection has voided most of the formal basis on which to build-up appropriate Monte Carlo schemes. The dynamics of strongly correlated systems is indeed a very hard problem in which the specific structure of the energy eigenspectrum plays a decisive role. Nonetheless, important experimental achievements in the context of cold atoms have recently made possible the study of closed systems in a regime of full quantum coherence and for relatively long times. These exciting experimental advances have lead to the possibility to probe very fundamental aspects of quantum Mechanics and the mechanisms beyond the approach to equilibrium. From a theoretical point of view, it is however particularly challenging to assess the validity of one of the most important axioms of Statistical Mechanics, namely the ergodic principle and its physical consequences.

In this Thesis we have examined this problem both from a phenomenological and a more methodological point of view. Concerning the first one, we have provided convincing evidences that a form of long-lived metastability can be observed in realistic experiments with cold atoms.[31] The nature of this metastability is merely due to strong correlation and has surprising analogies with the sharp transition observed in structural glasses. Concerning the methodological advancements, we have introduced an extension of the Variational Monte Carlo to out-of-equilibrium problems.[32] The importance of this novel scheme resides in its range of applicability and in its accuracy. The applicability is indeed not limited to one-dimensional geometries and short time scales as most of the existing exact methods, whereas its accuracy is highly competitive with renormalization-based numerical tools.

Outlook

In the first part of the Thesis we mostly concentrate on spectral properties of strongly correlated systems and on their equilibrium properties. This is accomplished by the general concept of *imaginary-time* dynamics which we apply to a number of different problems in which different strengths of this approach emerge.

- In Chapter 1 we introduce the formalism that allows for a connection between the quantum and the classical worlds. The connection is established by means of the imaginary-time quantum evolution which, under certain circumstances, is shown to be equivalent to a classical stochastic process. It is further shown that exact static and spectral properties of correlated systems can be obtained when this mapping is feasible. The relationship between the imaginary-time dynamics in different frameworks such as the path-integral and the perturbative one is also underlined.

- In Chapter 2 we present a specific implementation of the general ideas previously presented. In particular we introduced an extension to lattice systems of the Reptation Monte Carlo algorithm [30] which benefits of a sampling scheme based on directed updates. Specific improvements over the existing methodologies consist in the unbiased evaluation of the imaginary-time path integrals for bosons and a systematic scheme to improve over the Fixed-node approximation for fermions. Applications to the Hubbard and the Heisenberg models are presented.

- In Chapter 3 we demonstrate the application of the imaginary-time dynamics to the exact study of spectral properties. Subject of our attention is a highly anharmonic and correlated quantum crystal such as Helium 4 at zero temperature.[33] Concerning this system, we have obtained the first *ab-initio* complete phonon dispersion in good agreement with neutron spectroscopy experiments. Moreover, we have also studied the density excitations of solid helium in a region of wave-vectors in between the collective (phonon) and the single-particle regimes, where the presence of residual coherence in the dynamics shows analogies between the highly anharmonic crystal and the superfluid phase.

- In Chapter 4 we introduce a novel method, based on the imaginary-time dynamics, to obtain unbiased estimates of fermionic properties.[34] By means of this method and of a very accurate variational state, we provide strong evidence for the stability of a saturated ferromagnetic phase in the high-density regime of the two-dimensional infinite-U Hubbard model. By decreasing the electron density, we observe a discontinuous transition to a paramagnetic phase, accompanied by a divergence of the susceptibility on the paramagnetic side.

This behavior, resulting from a high degeneracy among different spin sectors, is consistent with an infinite-order phase transition scenario.

- In Chapter 5 the use of imaginary-time dynamics in the context of finite-temperature response functions is highlighted. As an application, we study an intriguing quantum phase featuring both glassy order and Bose-Einstein condensation. [35] We introduce and validate a model for the role of geometrical frustration in the coexistence of off-diagonal long range order with an amorphous density profile. The exact characterization of the response of the system to an external density perturbation is what allows here to establish the existence of a spin-glass phase. The differences between such a phase and the otherwise insulating "Bose glasses" are further elucidated in the Chapter.

In the second part of the Thesis we focus our attention on the dynamics of closed systems out of equilibrium. This is accomplished by both non-stochastic exact methods for the dynamics and the introduction of a novel time-dependent Variational Monte Carlo scheme.

- In Chapter 6 exact diagonalization schemes and renormalization-based methods for one-dimensional systems are introduced. We identify key phenomenological traits resulting from the many-body correlation in closed systems driven sufficiently away from equilibrium.[31] We provide evidences that the dynamics of interacting lattice bosons away from equilibrium can be trapped into extremely long-lived inhomogeneous metastable states. The slowing down of incoherent density excitations above a threshold energy, much reminiscent of a dynamical arrest on the verge of a glass transition, is identified as the key feature of this phenomenon.

- In Chapter 7 we present an extension to dynamical properties of the Variational Quantum Monte Carlo method.[32] This is accomplished by introducing a general class of time-dependent variational states which is based on the mapping of the many-body dynamics onto an instantaneous ground-state problem. The application of the method to the experimentally relevant quantum quenches of interacting bosons reveals the accuracy and the reliability of the introduced numerical scheme. We indeed obtain for the first time a consistent variational description of the approach to the equilibrium of local observables and underline the origin of the metastability and glassy behavior previously identified.

In the very last part we draw our conclusions and show some possible paths for stimulating future research.

Part I
Imaginary-Time Dynamics

Equilibrium Properties

> Sans l'imagination, il n'y aurait pas
> de ressemblance entre les choses
>
> Michel Foucault, "*Les mots et les choses*"

Chapter 1

The Imaginary-Time Connection

A Stochastic Bridge Between the Classical and the Quantum Worlds

The so-called *imaginary* time is a rather unfamiliar concept which nonetheless constitutes an essential tool to establish a *connection* among the classical and the quantum worlds. This mathematical object is of paramount importance in providing such a link and it is at the basis of the interpretation of quantum mechanics in terms of classical and more intuitive concepts. The resulting connection is moreover a the very roots of the possibility to study numerically quantum phenomena by means of a class of methods that generally goes under the name of *quantum Monte Carlo*. Despite the numerous flavors of the numerical algorithms within this class of techniques, the imaginary-time connection is the common inspiring paradigm and therefore deserves a special treatment. In this Chapter we discuss and concentrate on the most general concepts underlying the imaginary-time connection, whereas a practical numerical implementation of the ideas shown here will be given in the next Chapter.

Hereinafter, we present two different contexts in which the imaginary-time connection manifests itself, namely classical diffusion and the path-integral representation of quantum mechanics. We show how these concepts are of great importance in offering an unbiased access to both spectral and response properties of interacting quantum systems. Finally, we underline the connection between the imaginary-time representation of quantum mechanics and different types of perturbation theories.

1.1 Classical Diffusion and Quantum Mechanics

The somehow abstract notion of imaginary time is in reality at the very roots of a connection between the classical and the quantum world which is for many aspects surprising. Indeed, the stochastic diffusion of a purely classical particle is in rigorous connection with the imaginary-time dynamics of an otherwise quantum particle. [110]

To demonstrate this connection, we consider a classical particle suspended in a fluid and subject to a given external potential $U(\mathrm{x})$ which depends on the particle coordinates. The Newtonian dynamics of this particle is well described as a stochastic Brownian motion at a given temperature T.[74] The equation of motion that the particle coordinates obey is therefore the Langevin equation

$$\gamma \frac{d\mathbf{x}}{dt} = -\frac{\partial}{\partial \mathbf{x}} U(\mathbf{x}) + \boldsymbol{\eta}(t), \tag{1.1.1}$$

where γ is the friction coefficient for the diffusion of the particle in the environment and $\boldsymbol{\eta}(t)$ is a Gaussian noise with zero mean and covariance $\langle \eta^{\alpha}(t)\eta^{\beta}(t')\rangle = 2T\gamma\delta_{\alpha,\beta}\delta(t-t')$. In the following, for simplicity we set the friction coefficient to $\gamma = 1$.

The Langevin equation is a stochastic differential equation in the variables x and a mathematically unambiguous meaning to its solutions can be given through the theory of stochastic calculus.[74] However, it is more appropriate for our purposes to consider here the time-discretized version of this equation. We therefore integrate both sides of Eq. (1.1.1) over a small time-step ϵ and obtain

$$\mathbf{x}(t_{n+1}) - \mathbf{x}(t_n) = -\epsilon \left.\frac{\partial}{\partial \mathbf{x}} U(\mathbf{x})\right|_{\mathbf{x}(t_n)} + \int_{t_n}^{t_{n+1}} dt \boldsymbol{\eta}(t), \tag{1.1.2}$$

where the discretized time is $t_n = \epsilon n$ and we have neglected higher order terms in ϵ. The integral on the right hand side can be explicitly performed considering that an integral of a Gaussian variable is itself normally distributed. Indeed one can show that $\int_{t_n}^{t_{n+1}} dt \boldsymbol{\eta}(t) = \sqrt{2\epsilon T}\boldsymbol{\xi}(t_n)$, where $\boldsymbol{\xi}(t_n)$ are random variables normally distributed, i.e. with zero average and unitary variance.

1.1.1 Fokker-Planck Equation

The discretized formulation of the Langevin equation is particularly useful because it takes the form of a Markov process, where at each time step the particle coordinates change according to

$$\mathbf{x}(t_{n+1}) = \mathbf{x}(t_n) - \epsilon \frac{\partial}{\partial \mathbf{x}} U(\mathbf{x}) + \sqrt{2\epsilon T}\, \boldsymbol{\xi}(t_n). \tag{1.1.3}$$

By the theory of Markov processes it is well known that the time evolution of the probability distribution for the variable x is given by the master equation

$$P(\mathbf{x}, t_{n+1}) = \int K(\mathbf{x}|\mathbf{y}) P(\mathbf{y}, t_n) d\mathbf{y}, \tag{1.1.4}$$

where $K(\mathbf{x}|\mathbf{y})$ is the conditional probability that the particle is in a configuration x after a jump in which the particle was in a initial configuration y. Due to the particular form of the Gaussian transition in (1.1.3), the conditional probability reads

$$K(\mathbf{x}|\mathbf{y}) \propto \int d\mathbf{z}\, e^{-\frac{\mathbf{z}^2}{2}} \delta\left(\mathbf{x} - \mathbf{y} + \epsilon \frac{\partial}{\partial \mathbf{y}} U(\mathbf{y}) - \sqrt{2\epsilon T}\,\mathbf{z}\right). \tag{1.1.5}$$

Replacing the form of the conditional probability in the master equation and considering the small ϵ expansion of the Dirac delta, we can determine the equation of motion for the probability density, which reads

$$P(\mathbf{x}, t_{n+1}) = P(\mathbf{x}, t_n) + \epsilon \left[T \frac{\partial^2}{\partial \mathbf{x}^2} P(\mathbf{x}, t_n) + \frac{\partial}{\partial \mathbf{x}} \left(\frac{\partial}{\partial \mathbf{x}} U(\mathbf{x}) P(\mathbf{x}, t_n) \right) \right]. \tag{1.1.6}$$

In the continuous-time limit and generalizing the formalism to an ensemble on N particles, we can write a first-order differential equation for the probability density in the form

$$\partial_t P = -\mathcal{F} P, \tag{1.1.7}$$

where we have introduced the Fokker-Planck operator [53, 104]

$$\mathcal{F} = -\sum_i \frac{\partial}{\partial \mathbf{x}_i} \left[\frac{\partial}{\partial \mathbf{x}_i} U(\mathbf{x}_1, \dots \mathbf{x}_N) + T \frac{\partial}{\partial \mathbf{x}_i} \right]. \tag{1.1.8}$$

The Fokker-Planck operator is non-hermitian and it can be shown that its eigenvalues are larger than or equal to zero.[110] In particular, the lowest eigenvalue is vanishing and correspond to the classical canonical ensemble probability density, namely

$$P_0(\mathbf{x}_1, \dots \mathbf{x}_N) = \frac{1}{Z_N} e^{-\frac{U(\mathbf{x}_1, \dots \mathbf{x}_N)}{T}}, \tag{1.1.9}$$

where Z_N is the partition function that normalizes the probability. The equilibrium distribution for the Langevin process is therefore just the Gibbs measure at the given temperature T.

1.1.2 The Classical-Quantum Mapping

A deep connection exists between the dynamical evolution of classical particles described by the Langevin equation and a set of quantum particles described by a particular Hamiltonian operator. This connection [97, 152] is particularly suggestive because it shows that the *real-time* dynamics of classical particles in an external medium actually corresponds to the *imaginary-time* dynamics of an associated quantum system. The imaginary time therefore enters as a link between the classical and the quantum worlds.

Such a connection is realized upon considering a mapping of the Fokker-Planck operator into a hermitian Hamiltonian operator, by means of the similarity transformation

$$\tilde{\mathcal{H}} = e^{\frac{1}{2T}U} \mathcal{F} e^{-\frac{1}{2T}U}, \tag{1.1.10}$$

which leads to the quantum Hamiltonian

$$\tilde{\mathcal{H}} = -\sum_i \frac{\nabla_i^2}{2m} + \mathcal{V}(\mathbf{x}_1, \ldots \mathbf{x}_N), \tag{1.1.11}$$

where the particle masses are $m = 1/2T$ and the interaction potential has the form

$$\mathcal{V}(\mathbf{x}_1, \ldots \mathbf{x}_N) = \sum_i \left[\frac{(\nabla_i U)^2}{4T} - \frac{1}{2} \nabla_i^2 U \right]. \tag{1.1.12}$$

The eigenvalues and the eigenvectors of the introduced quantum Hamiltonian are in correspondence with the eigenvalues and eigenvector of the Fokker-Planck operator. More specifically, due to the particular form of the transformation introduced, they have the same eigenvalues while their eigenvectors are related through

$$\Psi_k(\mathbf{x}) \propto e^{U/2T} P_k(\mathbf{x}), \tag{1.1.13}$$

where Ψ_k are the eigenfunctions of the quantum Hamiltonian. In particular, the ground state of the quantum Hamiltonian will have zero energy and directly correspond to the Gibbs measure, being equal to

$$\Psi_0(\mathbf{x}) = \frac{1}{\sqrt{Z_N}} e^{-\frac{U(\mathbf{x}_1, \ldots \mathbf{x}_N)}{2T}}. \tag{1.1.14}$$

Such a mapping explicitly shows that the stochastic dynamics of a classical systems corresponds to the imaginary-time dynamics of a quantum systems of interacting particles. The price to be paid is that the quantum interaction potential is not simply the original interaction potential of the classical system but it includes kinetic corrections which might be not trivial to deal with. In particular, the Fokker-Planck quantum Hamiltonian satisfies an imaginary-time Schrödinger Equation of the form

$$\partial_\tau \Psi(\mathbf{x}, \tau) = -\tilde{\mathcal{H}} \Psi(\mathbf{x}, \tau), \tag{1.1.15}$$

where one can show that $\Psi(\mathbf{x}, \tau) = P(\mathbf{x}, \tau)/P_0(\mathbf{x})$.

1.1.3 Classical Stochastic Dynamics of a Quantum Problem

The previously established connection hints to the possibility of describing interacting quantum systems by means of an underlying purely *classical* stochastic dynamics. This analogy can be pushed further demonstrating that the mapping can take place in the other direction as well: the imaginary-time dynamics of a *generic* quantum Hamiltonian can be mapped, under certain assumptions, into a corresponding classical stochastic problem. The previous restriction on the particular form of the resulting quantum interaction can be therefore lifted and a quantum to classical mapping can be successfully realized.

Indeed, we can consider the differential equation associated to the imaginary-time evolution

$$\partial_\tau \Psi(\mathbf{x},\tau) = -\mathcal{H}\Psi(\mathbf{x},\tau), \tag{1.1.16}$$

which in an integral form is equivalent to

$$\Psi(\mathbf{x},\tau+\epsilon) = \int G^\epsilon(\mathbf{x},\mathbf{y})\Psi(\mathbf{y},\tau)d\mathbf{y}, \tag{1.1.17}$$

where we have introduced the propagator in imaginary time

$$G^\epsilon(\mathbf{x},\mathbf{y}) = \langle\mathbf{x}|\, e^{-\epsilon\mathcal{H}}\, |\mathbf{y}\rangle\,. \tag{1.1.18}$$

As long as the wave-function is positive-defined, we can therefore immediately recover in Eq. (1.1.17) the same structure of the master equation for a Markov process, such as (1.1.4), with the imaginary-time propagator, once correctly normalized, playing the role of a conditional probability. This very general idea is at the basis of the oldest developed numerical stochastic methods for interacting quantum systems, such as the the green-function Monte Carlo method [73]. In particular, a simple Markov process can be devised in order to mimic the imaginary-time evolution of the quantum Hamiltonian.

At each step of the discretized imaginary-time evolution a new spatial configuration for the system is generated according to the probability

$$T_{\mathbf{x}(\tau)\to\mathbf{x}(\tau+\epsilon)} = \frac{G_\epsilon\left[\mathbf{x}(\tau+\epsilon),\mathbf{x}(\tau)\right]}{w(\mathbf{x}(\tau))}, \tag{1.1.19}$$

where we have introduced the normalization factor

$$w(\mathbf{x}(\tau)) = \int G_\epsilon(\mathbf{y},\mathbf{x}(\tau))d\mathbf{y}. \tag{1.1.20}$$

Due to the presence of these time-dependent normalization factors, it can be easily realized that a Markov process in which transitions are done according to (1.1.19) will determine a time-dependent probability which does not coincide with $\Psi(x,\tau)$. To overcome this issue one has indeed to consider an enlarged configurational space determined by both the particle coordinates $\mathrm{x}(\tau)$ *and* some residual weights $\bar{W}(\tau)$. The residual weights are evolved according to $\bar{W}(\tau+\epsilon) = \bar{W}(\tau)\times w(\mathbf{x}(\tau))$, with the corresponding conditional probability given by

$$K\left[\mathbf{y},\bar{W}'|\mathbf{x},\bar{W}\right]=T_{\mathbf{x}\rightarrow\mathbf{y}}\delta\left[\bar{W}'-\bar{W}\times w(\mathbf{x})\right], \tag{1.1.21}$$

and the master equation for this enlarged space reads

$$P_{\tau+\epsilon}(\mathbf{x},\bar{W})=\int K\left[\mathbf{x},\bar{W}|\mathbf{y},\bar{W}'\right]\times P_{\tau}(\mathbf{y},\bar{W}')d\mathbf{y}d\bar{W}'. \tag{1.1.22}$$

In practice, even if formally correct, such a simple formulation of the Markov process is numerically unstable due to the large fluctuations of the residual weights. Methods to overcome this issue have been introduced and successfully applied in a number of different contexts and basically amount to generate a sequence of Markov chains of which only those with a sufficiently large weight are propagated whereas the others are conveniently terminated and reinitialized with the information carried in the other chains. Details of this process, known in literature as the *branching scheme*, can be found elsewhere [54, 130] and will not be discussed here.

1.2 Path-Integrals

The path-integral formulation of quantum mechanics, due to the successful elaboration by Richard Feynman [50] of Paul Dirac's original idea,[47] is in many ways another important bridge between the classical and the quantum world. In this respect it is natural to foresee an application of this idea to the simulation of the intriguing properties of quantum systems by means of an auxiliary classical problems. Whereas this program is at the very foundation of the previous discussions on the correspondence between a classical, stochastic system, and a quantum one, it is with the path integral formulation that such a useful correspondence can be pushed further.

In the path-integral formalism the imaginary-time evolution of a quantum state is mapped into a superposition of classical trajectories (paths) in space-time. We again consider the imaginary-time Schrödinger equation

$$\partial_{\tau}\Psi(\mathbf{x},\tau)=-\mathcal{H}\Psi(\mathbf{x},\tau), \tag{1.2.1}$$

with initial condition $\Psi(\mathbf{x},\tau=0)=\Phi_0(\mathbf{x})$, which we assume to be a known state being a linear superposition of eigenstates of $\mathcal{H}$. We can formally write the evolved state at a certain time as

$$\Psi(\mathbf{x},\tau)=\langle\mathbf{x}|\,e^{-\tau\mathcal{H}}\,|\Phi_0\rangle\,, \tag{1.2.2}$$

which, at variance with the real-time dynamical evolution is not a conservative unitary dynamics, therefore not conserving neither the energy nor the norm. Indeed, in the limit of large imaginary time τ, the evolved state will be proportional to the lowest eigenstate of $\mathcal{H}$ non-orthogonal to $\Phi(\mathbf{x})$. To elucidate this point, we consider the representation of the initial state in the eigenstates of the Hamiltonian,

$$\Phi_0(\mathbf{x}) = \sum_k c_k \Psi_k(\mathbf{x}), \tag{1.2.3}$$

with coefficients c_k. The evolved state thus reads

$$\Psi(\mathbf{x}, \tau) = \sum_k e^{-\tau E_k} \Psi_k(\mathbf{x}) c_k, \tag{1.2.4}$$

which we can as well rewrite arranging the energies E_k in ascending order and isolating the lowest eigenvalue as

$$\Psi(\mathbf{x}, \tau) = e^{-\tau E_0} \left[c_0 \Psi_0(\mathbf{x}) + \sum_{k \neq 0} e^{-\tau \Delta_k} c_k \Psi_k(\mathbf{x}) \right], \tag{1.2.5}$$

where $\Delta_k = E_k - E_0 > 0$ having assumed that the lowest eigenstate is non-degenerate. In the limit of large τ it is easily recognized that the terms appearing in the summation are exponentially suppressed and that

$$\Psi(\mathbf{x}, \tau \to \infty) \simeq e^{-\tau E_0} c_0 \Psi_0(\mathbf{x}), \tag{1.2.6}$$

in other words, the long-time evolution of our initial state approaches an *exact* and possibly unknown eigenstate of $\mathcal{H}$. For this reason, the application of the long imaginary-time evolution onto an arbitrary state is often regarded as a *projection* of the initial state onto the exact eigenstate of the Hamiltonian.

The connection of $\Psi(\mathbf{x}, \tau)$ with the classical trajectories of an auxiliary classical system is realized when considering a time-discretization of the imaginary propagation, namely $\tau = M \times \epsilon$ which leads to

$$\Psi(\mathbf{x}, \tau) = \langle \mathbf{x} | \underbrace{e^{-\epsilon \mathcal{H}} e^{-\epsilon \mathcal{H}} \dots e^{-\epsilon \mathcal{H}}}_{M \text{ times}} | \Phi \rangle, \tag{1.2.7}$$

and upon insertion of a set of M completeness relations $\int d\mathbf{x}_k \left| \mathbf{x}_k \right\rangle \left\langle \mathbf{x}_k \right|$ we arrive to the integral expression

$$\Psi(\mathbf{x}, \tau) = \int d\mathbf{x}_1 \dots d\mathbf{x}_M \prod_{i=1}^{M} G^\epsilon(\mathbf{x}_{i-1}, \mathbf{x}_i) \Phi(\mathbf{x}_M), \tag{1.2.8}$$

where $\mathbf{x}_0 \equiv \mathbf{x}$ and having considered the previously introduced short-time propagators $G^\epsilon(\mathbf{x}, \mathbf{y}) = \langle \mathbf{x} | e^{-\epsilon \mathcal{H}} | \mathbf{y} \rangle$ which are typically analytically known in the limit of small time-step ϵ.

Such a representation leads both to a suggestive interpretation of the quantum evolution and to a fundamental tool for practical computational schemes. Concerning the first one, we notice that the amplitude of the evolved wave-function on a given configuration is the sum over an (infinite) set of trajectories in imaginary time, namely at variance with the classical case, there does not exist a unique dynamical trajectory that connects configurations at different times, but a superposition of them, with a quantum trajectory therefore regarded as a sum of many classical ones. On the other hand, as long as such trajectories carry a positive weight it is possible and straightforward to identify the imaginary-time propagation with a stochastic process. We mention here that this deep connection is at the core of numerical methods such as the path integral quantum Monte Carlo at finite temperature [36] and its zero temperature counterparts such as the path integral ground-state method [118] or the reptation quantum Monte Carlo.[8, 30] Instead of entering into the details of all of these numerical schemes, we defer the reader to more specific literature on the subject. However, in the next Chapter, we will give a full account of a novel path-integral based method, therefore also giving further details on how a path-integral scheme can be successfully devised and applied by means of a stochastic approach.

1.3 Exact Properties of Quantum Systems

In the previous section we have shown that in the long imaginary-time limit the projected state approaches an exact eigenstate of the Hamiltonian and, more specifically, the lowest-energy eigenstate non orthogonal to the initial state. Taking advantage of this very important result, it is possible to exploit the time projection in order to obtain exact properties of quantum systems.

We now introduce a pseudo partition function

$$\mathcal{Z}(\tau) = \langle \Phi_0 | \, e^{-\tau\mathcal{H}} \, | \Phi_0 \rangle \,, \tag{1.3.1}$$

which plays the role of a generating function for a number of exact properties of the system, much as for ensemble partition functions in statistical mechanics. A path-integral expression for the pseudo partition function can be immediately recovered and in the continuous imaginary time limit reads

$$\mathcal{Z}(\tau) = \int \mathcal{D}[\mathbf{X}] \Pi^{\tau}(\mathbf{X}), \tag{1.3.2}$$

where the weight of each imaginary-time path is obtained considering small time steps such that $\tau = \epsilon \times M$ and then taking the limit:

$$\varPi^\tau(\mathbf{X}) = \lim_{\substack{\epsilon\to 0\\ M\to\infty}} \varPhi_0(\mathbf{x}_0)\prod_{i=1}^{M} G_\epsilon(\mathbf{x}_{i-1},\mathbf{x}_i)\varPhi_0(\mathbf{x}_M). \tag{1.3.3}$$

The above introduced $\varPi^\tau(\mathbf{X})$ is in general *not* normalized and *not* positive defined, and should therefore be regarded as a *pseudo* probability density. While a proper normalization can be generally achieved as long as $\mathcal{Z}(\tau)$ is a finite quantity, the condition of positiveness is generally achieved only for bosonic species of quantum particles. A strictly probabilistic interpretation closely paralleling classical statistical mechanics is therefore only possible when these two conditions are achieved. Implications and limitations arising from the above mentioned limited probabilistic interpretation will be detailed in the next Chapter.

1.3.1 Ground-state Expectation Values

We assume in this context that $\varPhi_0$ is non-orthogonal to the ground state of $\mathcal{H}$ and also expand the initial state in eigenstates of the Hamiltonian as done before obtaining

$$\mathcal{Z}(\tau) = |c_0|^2 e^{-\tau E_0} + \sum_{k\neq 0} |c_k|^2 e^{-\tau E_k}. \tag{1.3.4}$$

From this expansion we can immediately realize that the exact ground-state energy E_0 is given by

$$E_0 = -\lim_{\tau\to\infty}\left\{\frac{1}{\tau}\log\left[\mathcal{Z}(\tau)\right]\right\}. \tag{1.3.5}$$

Ground-state expectation values of a local observable $\mathcal{O}$ can be as well obtained upon considering the perturbed Hamiltonian $\mathcal{H}(\lambda) = \mathcal{H} + \lambda\mathcal{O}$ and using the Hellmann-Feynman theorem,[49, 67] according to which

$$\langle\varPsi_0|\,\mathcal{O}\,|\varPsi_0\rangle = \left.\frac{dE_0(\lambda)}{d\lambda}\right|_{\lambda=0}, \tag{1.3.6}$$

where $E_0(\lambda)$ is the ground-state energy of $\mathcal{H}(\lambda)$. To explicitly evaluate the ground-state energy of the perturbed Hamiltonian, we consider the modified propagators $G^\epsilon(\mathbf{x},\mathbf{y};\lambda) = \langle\mathbf{x}|\,e^{-\epsilon\mathcal{H}(\lambda)}\,|\mathbf{y}\rangle$ and use the Trotter decomposition of such propagators which reads

$$G^\epsilon(\mathbf{x},\mathbf{y};\lambda) = G^\epsilon(\mathbf{x},\mathbf{y})\left[1-\epsilon\lambda\mathcal{O}(\mathbf{x})\right] + \mathcal{O}(\lambda^2). \tag{1.3.7}$$

The path-integral representation of the corresponding perturbed pseudo partition function is therefore

$$\mathcal{Z}(\tau;\lambda) = \mathcal{Z}(\tau) - \lambda \underbrace{\sum_j \epsilon \int d\mathbf{x}_0 \dots d\mathbf{x}_M \Phi_0(\mathbf{x}_0)\mathcal{O}(\mathbf{x}_j) \prod_{i=1}^{M} G_\epsilon(\mathbf{x}_{i-1},\mathbf{x}_i)\Phi_0(\mathbf{x}_M)}_{\Delta\mathcal{Z}} + \mathcal{O}(\lambda^2), \tag{1.3.8}$$

and to first-order in λ the perturbed ground-state energy is

$$E_0(\lambda) = E_0 + \lim_{\tau\to\infty} \frac{\lambda}{\tau}\frac{\Delta\mathcal{Z}}{\mathcal{Z}}. \tag{1.3.9}$$

In the continuous imaginary-time limit, the expectation value of the observable will therefore be equal to

$$\begin{aligned} \langle\Psi_0|\,\mathcal{O}\,|\Psi_0\rangle &= \lim_{\tau\to\infty} \frac{1}{\tau} \frac{\int_0^\tau d\tau_1 \,\langle\Phi_0|\, e^{-\tau\mathcal{H}}\mathcal{O}(\tau_1)\,|\Phi_0\rangle}{\mathcal{Z}(\tau)} && (1.3.10) \\ &= \lim_{\tau\to\infty} \frac{1}{\tau} \frac{\int_0^\tau d\tau_1 \int \mathcal{D}[\mathbf{X}]\Pi_\tau[\mathbf{X}]\mathcal{O}(\mathbf{x}(\tau_1))}{\mathcal{Z}(\tau)}, && (1.3.11) \end{aligned}$$

where we have introduced the Heisenberg time evolution of the observable, namely $\mathcal{O}(\tau) = e^{\mathcal{H}\tau}\mathcal{O}e^{-\mathcal{H}\tau}$.

1.3.2 Static Response Functions

In order to experimentally study the physical properties of a quantum system, one has to act on it with some external probe. This amounts to add to the original Hamiltonian of the isolated system an external perturbation. We can consider for example a set of external classical fields λ_i coupled to some observables $\mathcal{O}_i$, in a way that the resulting interaction is described by the Hamiltonian

$$\mathcal{H}_\lambda = \mathcal{H} + \sum_i \lambda_i \mathcal{O}_i. \tag{1.3.12}$$

Due to the presence of the external perturbation, the expectation values of the observables will change accordingly. It is therefore desirable to quantify the response of the quantum system to the external fields and compute the susceptibilities

$$\chi_{i,j} = \left.\frac{\partial\langle\mathcal{O}_i\rangle}{\partial\lambda_j}\right|_{\lambda=0}, \tag{1.3.13}$$

where angular brackets denote ground-state expectation values. Extending the previous analysis on the ground-state expectation values, we can express the ground-state expectation values in terms of energy derivatives and therefore $\chi_{i,j} = \left.\frac{\partial^2 E(\lambda)}{\partial\lambda_i\partial\lambda_j}\right|_{\lambda=0}$, where $E(\lambda)$ is the ground-state energy of the perturbed Hamiltonian. It is therefore possible to express the susceptibilities as imaginary-time integrals of the form

$$\chi_{i,j} = -\lim_{\tau \to \infty} \frac{1}{\tau} \int_0^\tau d\tau_1 \int_0^\tau d\tau_2 \left[\langle \mathcal{O}_i(\tau_1) \mathcal{O}_j(\tau_2) \rangle_{\Pi^\tau} - \langle \mathcal{O}_i(\tau_1) \rangle_{\Pi^\tau} \times \langle \mathcal{O}_j(\tau_2) \rangle_{\Pi^\tau} \right], \quad (1.3.14)$$

where angular brackets denote expectation values over the pseudo probability density Π^τ, namely for a generic function in the path space we define:

$$\langle F \rangle_{\Pi^\tau} = \frac{\int \mathcal{D}[\mathbf{X}] \Pi^\tau[\mathbf{X}] F[\mathbf{X}]}{\mathcal{Z}(\tau)}. \quad (1.3.15)$$

1.3.3 Correlations in Imaginary-Time and Spectral Functions

Static susceptibilities such as the ones introduced before provide precious information on the time-independent response of quantum systems subject to an external field. However, when the perturbation is itself time dependent it can induce specific spectral transitions that provide additional information on the excited states properties of the system. A quantity often appearing in linear response theory and that further relates the quantum fluctuations to the time-dependent dissipation are the so-called structure factors. Structure factors in imaginary-time take the form of two-point correlators on the path-integrals pseudo probabilities:

$$\mathcal{S}_{i,j}(\bar{\tau}) = \lim_{\tau \to \infty} \frac{1}{\tau} \int_0^{\tau - \bar{\tau}} d\tau_1 \left\{ \langle \mathcal{O}_i(\tau_1) \mathcal{O}_j(\tau_1 + \bar{\tau}) \rangle_{\Pi_\tau} - \langle \mathcal{O}_i(\tau_1) \rangle_{\Pi_\tau} \times \langle \mathcal{O}_j(\tau_1) \rangle_{\Pi_\tau} \right\}, (1.3.16)$$

where $\bar{\tau}$ is an imaginary-time lag. In the large τ limit the integrand above is equivalent to the ground-state average of the time correlations, namely

$$S_{i,j}(\bar{\tau}) = \langle \mathcal{O}_i(\bar{\tau}) \mathcal{O}_j \rangle - \langle \mathcal{O}_i \rangle \times \langle \mathcal{O}_j \rangle. \quad (1.3.17)$$

This expression can in turn be expressed in terms of eigenfunctions of the Hamiltonian, leading to the so-called Lehman spectral representation

$$\mathcal{S}_{i,j}(\bar{\tau}) = \sum_k e^{-\Delta_k \bar{\tau}} \langle \Psi_0 | \delta\mathcal{O}_i | \Psi_k \rangle \langle \Psi_k | \delta\mathcal{O}_j | \Psi_0 \rangle, \quad (1.3.18)$$

where we have introduced the fluctuations over the ground-state value of the observables, namely $\delta\mathcal{O}_i = \mathcal{O}_i - \langle \mathcal{O}_i \rangle$. The spectral representation of the imaginary-time structure factors is particularly enlightening on their deepest physical meaning. The matrix elements appearing in the Lehman representation correspond, respectively, to excitation processes in which the operator $\mathcal{O}_i$ drives the initial (ground)-state into an excited state Ψ_k, whereas the corresponding de-excitation process occurs through the operator $\mathcal{O}_j$. Structure factors are of paramount importance for experimental measurements in which a probe induces an absorption of energy in the analyzed sample. Indeed in most relevant cases the external probe is a beam of incoming particles, either photons, neutrons or others and the physical system adsorbs energy due to a coupling with the beam mediated by some operator $\mathcal{O}_A$ (which can be, for example, the density or some spin degrees of freedom). The adsorption rate per unit time of an energy $\hbar\omega$ is in this case a key measurable quantity and it is given by the Fermi golden rule. The Fourier transform of the associated structure factor is proportional to the absorption rate $P_A(\omega) \propto \int S_{A,A}(t)e^{-i\omega t}$ and therefore much of the physical information accessible in the experiment is parallely accessible in path-integral based numerical simulations, provided that an analytical continuation of the imaginary-time structure factors is realized. The amount of information that can be extracted from imaginary-time correlations is therefore bound to the accuracy of the analytical continuation, which we discuss more thourougly in the following.

1.3.4 Analytical Continuation and Maximum Entropy Method

The Fourier trasform of the real-time structure factors, in imaginary time takes the form of a Laplace transform. The energy-resolved structure factors are related to the imaginary-time structure factors through the integral equation

$$S(\bar{\tau}) = \int_0^\infty P(\omega) e^{-\omega\bar{\tau}} d\omega. \tag{1.3.19}$$

In numerical simulations, $S(\bar{\tau})$ is typically accessible only for a discrete set of values of $\bar{\tau}$ (which we call $\bar{\tau}_k$) and with an associated statistical incertitude. In particular, we imagine that N measurements of the imaginary-time structure factors at the given time values have been performed, which we denote as $S^i(\bar{\tau}_k)$, with $i = 1, \ldots N$. Numerical schemes to invert the Laplace transform and obtain the spectral function $P(\omega)$ are therefore concerned with the search for some optimal solution $P^{\text{opt}}(\omega)$, in turn related to some associated optimal values of the correlations via

$$S^{\text{opt}}(\bar{\tau}_k) = \int_0^\infty P^{\text{opt}}(\omega) e^{-\omega\bar{\tau}_k} d\omega. \tag{1.3.20}$$

There exist however numerous solutions for $P(\omega)$ which both satisfy Eq. (1.3.20) and that are statistically compatible with the measured values $S^i(\bar{\tau}_k)$. The maximum-likelood estimator for a given pairs of S and G satisfying Eq. (1.3.20) reads

$$\chi^2(S,G) = \sum_{i,j}^{N} \left[S^i(\bar{\tau}_k) - S(\bar{\tau}_k)\right] C^{-1}_{i,j} \left[S^j(\bar{\tau}_k) - S(\bar{\tau}_k)\right], \tag{1.3.21}$$

and it is a measure of the statistical deviation of a given solution with respect to the measured values, $C_{i,j}$ being the covariance matrix of the measurements.

However, it is not always the case that the best physical solution for the spectral functions is found amongst the many possible ones that minimize the χ^2 function. Indeed, it has been proven useful to include some prior knowledge on the required features of the spectral functions (such as their high-frequency behavior or more general regularity constraints) in order to obtain physically sound solutions. In particular, the Maximum Entropy Method amounts to maximize the quantity

$$Q(S,G) = \alpha \Sigma(G) - \chi^2(S,G), \tag{1.3.22}$$

where α is a positive constant, and $\Sigma(G)$ is the *entropy* associated to a given solution. The entropy term measures the deviation of a proposed spectral function from a given regular model imposed a-priori. The optimal solutions S^{opt},G^{opt} are therefore the ones that maximize $Q(S,G)$, and represent an optimal compromise between the need for a regular solution and the need of statistical compatibility with the measured values. The choice of the entropy form and of the models are fully discussed in Ref. [64], to which we defer the interested reader.

As a general consideration, the Maximum Entropy method is suitable to recover important physical properties of the spectral functions such as the position of their peaks (which are physically associated to the excitation processes described previously). However, thiner spectral feature are, in pratice, dependent on the chosen model for the Maximum Entropy procedure and therefore constitute a not particularly accurate quantitaty to be extracted from imaginary-time correlations.

1.4 Perturbative Expansions for the Imaginary-Time Evolution

Perturbative methods have played a major role in the advancement of the theoretical understanding of many body interacting quantum systems. The aim of this class of methods is to express the exact properties of a complicated many body problem in terms of an auxiliary one which can be more easily solved. Whereas this program is generally only partially accomplished in the framework of approximate diagrammatic analysis,[1] in recent years it has been possible to devise numerical methods that allow for an exact evaluation of the perturbative expansions. In the following, we put the quantum imaginary-time evolution in connection with two distinct perturbative methods.

We first show the representation of the imaginary-time dynamics in terms of the perturbative Dyson series. Such a representation offers yet another way of looking at the quantum-classical mapping. Furthermore, it provides an alternative and often powerful formal basis for the numerical analysis of a large class of quantum systems with discrete spatial degrees of freedom.

We then establish a connection between the path-integral representation and the Rayleigh-Schrödinger perturbation theory. This last connection, often neglected, is of general interest in the analysis of the response to small perturbations acting on a system at equilibrium.

1.4.1 The Dyson Series

A conceptually different way of looking at the quantum imaginary-time evolution is offered by the Dyson perturbative expansion.[1] The basic idea underlying the expansion is to consider an unperturbed Hamiltonian $\mathcal{H}_0$ whose eigenstates are known and some perturbation $\mathcal{W}$, such that the full Hamiltonian reads $\mathcal{H} = \mathcal{H}_0 + \mathcal{W}$. The imaginary-time evolution is then factorized as

$$e^{-\tau\mathcal{H}} = e^{-\tau\mathcal{H}_0}\mathcal{S}(\tau) \tag{1.4.1}$$

where we have introduced the so-called $\mathcal{S}$ matrix which satisfies the equation of motion

$$\frac{d}{d\tau}\mathcal{S}(\tau) = -\mathcal{W}(\tau)\mathcal{S}(\tau). \tag{1.4.2}$$

The time evolution of the perturbation is considered in the so-called “interaction representation”, which reads $\mathcal{W}(\tau) = e^{\mathcal{H}_0\tau}\mathcal{W}e^{-\mathcal{H}_0\tau}$. This equation of motion can be iteratively solved resulting in an expansion in terms of powers of the interaction strength

$$\mathcal{S}(\tau) = \sum_{k=0}^{\infty}\mathcal{S}_k(\tau), \tag{1.4.3}$$

where the k-th perturbative order reads

$$\mathcal{S}_k(\tau) = \frac{(-1)^k}{k!}\int_0^\tau \Pi_{i=1}^k d\tau_i T_\tau\left[\mathcal{W}(\tau_1)\mathcal{W}(\tau_2)\ldots\mathcal{W}(\tau_k)\right], \tag{1.4.4}$$

and the time ordered product T_τ chronologically orders the product of k perturbation operators.

The expression introduced above does not only constitute a formally exact basis for analytic perturbative expansions but also for successful numerical schemes.[106, 24, 112, 115] One of the major advantages of the Dyson representation with respect to the path-integral one is that there is no explicit zero time step limit to be considered (see Eq. 1.3.3). This circumstance is of great practical importance for numerical schemes in which the path-integral limit of exactly zero time step is only approximately achieved by increasingly small discretizations of time.

On the other hand, the Dyson expansion is generally applicable only when the matrix elements of the perturbation in the unperturbed basis, $\langle \Phi_0^k|\mathcal{W}|\Phi_0^{k'}\rangle$, are non-singular. This condition is met when considering the lattice kinetic energy as a perturbation of a classical Hamiltonian in which the potential energy is diagonal. However, this is instead not generally the case for a system living in a continuous space, for which the former matrix elements are singular. This circumstance leads to an application of the Dyson series expansions mainly to quantum problems characterized by discrete spatial degrees of freedom.

1.4.2 Path-Integrals and Rayleigh-Schrödinger Perturbation Theory

We conclude the discussion on the perturbative expansions showing an instructive connection between the path-integral formalism introduced in 1.2 and the ordinary Rayleigh-Schrödinger perturbation theory. Indeed, we have seen that in the limit of large imaginary time projection the evolved state does approach en exact eigenstate of the Hamiltonian, therefore it is reasonable to expect that a kind of implicit resummation of a perturbative series takes place when considering the imaginary-time paths.

To elucidate this connection, we again consider the Hamiltonian $\mathcal{H}$ and suppose that its ground-state energy has to be determined. Moreover, we also introduce an "unperturbed" Hamiltonian $\mathcal{H}_0$ whose ground state $|\Phi_0\rangle$ is supposed to be known. The aim of the perturbation theory we want to pursue is therefore to determine the quantum properties of $\mathcal{H}$ considering the perturbation operator $\mathcal{W} = \mathcal{H} - \mathcal{H}_0$. If we call E the ground-state energy of the full Hamiltonian $\mathcal{H}$, then it is assumed that it is possible to write a series expansion in terms of the strength of the interaction $\mathcal{W}$, which we can imagine to enter via a coupling constant λ that we will eventually set equal to 1 at the end of the calculations, i.e. we have that $\mathcal{H} = \mathcal{H}_0 + \lambda\mathcal{W}$. In such a way, the perturbative expansion reads $E = E_0 + \lambda E_1 + \lambda^2 E_2 + \dots$ which is assumed to be "summable", either in the standard framework of the convergent series either in the framework of the asymptotic series.

The perturbed ground-state energy is derived considering the previously introduced Dyson expansion (1.4.3) and reads, also making use of (1.3.5),

$$E = E_0 - \lim_{\tau\to\infty} \frac{\log \langle \Phi_0|\, 1 + \lambda\mathcal{S}_1 + \lambda^2\mathcal{S}_2 + \dots |\Phi_0\rangle}{\tau}. \tag{1.4.5}$$

Assuming that E is an analytic function of λ, it is possible to identify the k-th order in the perturbation expansion for the energy with $E_k = \left.\frac{\partial^k E}{\partial \lambda^k}\right|_{\lambda=0}$. Defining the expectation values of the various orders of the $\mathcal{S}$ matrix, $\mathcal{S}_k$, over the unperturbed state:

$$
\begin{aligned}
\mathcal{S}^0_k(\tau) \;=\; & k! \langle \varPhi_0 | \, \mathcal{S}_k(\tau) \, | \varPhi_0 \rangle \;= \\
& \;=\; (-1)^k \langle \varPhi_0 | \int_0^\tau \varPi^k_{i=1} d\tau_i T_\tau \left[\mathcal{W}(\tau_1)\mathcal{W}(\tau_2)\ldots\mathcal{W}(\tau_k) \right] | \varPhi_0 \rangle \,, \quad (1.4.6)
\end{aligned}
$$

we can express the exact ground-state energy as

$$
E = E_0 - \lim_{\tau\to\infty} \frac{\log \sum_{k=1}^\infty \mathcal{S}^0_k(\tau)\frac{\lambda^k}{k!}}{\tau}. \qquad (1.4.7)
$$

Each order in standard Rayleigh-Schrödinger perturbation theory is therefore reconstructed considering a Taylor expansion of the logarithm in powers of λ, whose first few orders are:

$$
\begin{aligned}
E(\lambda) = E_0 - \lim_{\tau\to\infty} \frac{1}{\tau} \Bigg\{ & \lambda \left[S^0_1(\tau) \right] + \frac{\lambda^2}{2} \left[S^0_2(\tau) - S^0_1(\tau)^2 \right] + \\
& + \frac{\lambda^3}{3!} \left[S^0_3(\tau) - 3S^0_1(\tau)S^0_2(\tau) + 2S^0_1(\tau)^3 \right] \Bigg\} + O(\lambda^4), \qquad (1.4.8)
\end{aligned}
$$

where the terms in square brackets are the cumulants defined via the relation

$$
c_k = \frac{\partial^k}{\partial\lambda^k} \log \left[\sum_{j=1}^\infty S^0_j(\tau) \frac{\lambda^j}{j!} \right] \Bigg|_{\lambda=0} . \qquad (1.4.9)
$$

As we have seen before, the path-integral formalism gives access to the imaginary-time dynamics of generic observables and, in particular, gives access to the imaginary-time evolution of the interaction potential $\mathcal{W}(\tau) = e^{\mathcal{H}_0\tau}\mathcal{W}e^{-\mathcal{H}_0\tau}$. The various perturbative orders c_k are therefore in direct connection with the k-points imaginary-time correlations in (1.4.6). For example, the second-order correction to the ground-state energy reads

$$
E_2 = -\lim_{\tau\to\infty} \frac{1}{\tau} \int_0^\tau d\tau_1 \int_0^{\tau_1} d\tau_2 \left[\langle \varPhi_0 | \left(\mathcal{W}(\tau_1) - \langle \mathcal{W} \rangle \right) \left(\mathcal{W}(\tau_2) - \langle \mathcal{W} \rangle \right) | \varPhi_0 \rangle \right], \qquad (1.4.10)
$$

the k-th order containing imaginary-time correlation function of order k. It should be finally noticed that these kind of expressions is particularly useful when considering the action of an external perturbation over an equilibrium ground state. For example, the second-order correction to the ground-state energy is in direct connection with the susceptibilities (1.3.14), where the external field acting on the system is regarded as a small perturbation.

Chapter 2

Sampling Imaginary-Time Paths

Reptation Monte Carlo for Lattice Hamiltonians

The path-integral formulation of quantum mechanics introduced in the previous Chapter is the foundation of many numerical methods that allow one to study with great accuracy the rich physics of interacting quantum systems. The aim of this Chapter is to present a detailed description of a novel stochastic computational scheme based on the imaginary-time path integral formalism.

The first applications of a stochastic approach to the simulation of continuous systems trace back to Ceperley and Pollock [38, 36], whose path-integral Monte Carlo has provided the first exact results for the superfluid transition of Helium 4 at low temperatures and has given a huge momentum to the development of this class of computational methods. Recently, this finite-temperature approach has been renovated in a new class of methods known as worm algorithms, [106, 24] which allow for a consistently improved efficiency in the treatment of bosonic problems. At zero-temperature, alternative and more specific approaches have been developed on the lines of the formalism highlighted in the previous Chapter, with a variational state serving as the starting state for the imaginary-time projection. Zero-temperature counterparts of the path-integral Monte Carlo algorithm that have been developed in this spirit are the reptation quantum Monte Carlo [8] and the path-integral ground-state methods, [118] which have been demonstrated useful in a number of applications, such as the simulation of coupled electron-ion systems, [102] as well as to infer spectral properties from imaginary-time dynamics. [33]

A number of important physical problems—particularly in the fields of strongly correlated fermions and cold atoms—can be fruitfully modeled by lattice Hamiltonians. A first application of path-integral techniques to (boson) lattice models was proposed by Krauth *et al.* in 1991. [77] Few other attempts to apply path-integral Monte Carlo to lattice models have been made since, with a recent application of the reptation quantum Monte Carlo idea to the quantum dimer model Hamiltonian. [134] In this Chapter, we describe a method that generalizes and improves the approach of Ref. [134] in several ways. Our method is based on continuous-time random walks and is therefore unaffected by time-step errors resulting from the discretization of the imaginary-time propagation. Inspired by the work of Syljuasen and

Sandvik [135] and Rousseau, [114] we have adopted a generalization of the *bounce algorithm* of Pierleoni and Ceperley, [102] called *directed updates*, which helps to improve the overall computational efficiency by reducing the correlation time in path sampling. We also have introduced a worm-algorithm based method to calculate *pure* expectation values of arbitrary non-diagonal observables, which are generally out of the scope of existing lattice ground-state methods. The resulting algorithm naturally applies to fermions, using the so-called *fixed-node* approximation. We show here how to systematic improve this approximation, by means of the Hamiltonian moments.

In Sec. 2.1 we present the general formalism of ground-state path-integrals for lattice models; in Sec. 2.2 our implementation of the reptation quantum Monte Carlo algorithm on a lattice is presented. In particular, we give a detailed account of the above mentioned *directed update* technique (Sec. 2.2.1) and of the continuous-time propagator (Sec. 2.2.2); in Sec. 2.2.3, we introduce an extension of the algorithm to cope with non-diagonal observables, while in Sec. 2.2.4 a further extension to systems affected by sign problems is presented, including a strategy to improve systematically upon the fixed-node approximation. Sec. 2.3 contains a few case applications, including the simulation of the spectral properties and spin correlations of the one-dimensional Heisenberg model and the calculation of the ground-state energies of the fermionic Hubbard model with a significantly better accuracy than that achieved by the fixed-node approximation.

2.1 General Formalism

Let us consider a generic lattice Hamiltonian $\mathcal{H}$ and a complete and orthogonal basis set, whose states are denoted by $|x\rangle$. Given the generic wave function $|\Psi\rangle$, its amplitude on the configuration $|x\rangle$ will be denoted by $\Psi(x)$, namely $\Psi(x) = \langle x|\Psi\rangle$. As shown in the previous Chapter, the exact ground-state wave function $|\Psi_0\rangle$ can be obtained by the imaginary-time evolution of a variational state $|\Phi_0\rangle$:

$$|\Psi_0\rangle \propto \lim_{\tau\to\infty} |\Psi_\tau\rangle, \tag{2.1.1}$$

where $|\Psi_\tau\rangle \equiv e^{-\tau\mathcal{H}}|\Phi_0\rangle$, provided that the variational state is non-orthogonal to $|\Psi_0\rangle$, i.e., $\langle\Phi_0|\Psi_0\rangle \neq 0$. Then, the ground-state expectation value of a quantum operator $\mathcal{O}$ can be as well obtained by

$$\langle\mathcal{O}\rangle = \lim_{\tau\to\infty} \frac{\langle\Psi_\tau|\mathcal{O}|\Psi_\tau\rangle}{\langle\Psi_\tau|\Psi_\tau\rangle}. \tag{2.1.2}$$

At variance with the previously introduced estimator 1.3.11, the above expression exponentially converges to the exact ground-state expectation values for large values of τ, whereas in the previous case such a convergence is achieved only polynomially.

A practical computational scheme can be conveniently introduced by considering the path-integral representation of the imaginary-time evolution. To such a purpose, we split the total imaginary-time τ into M slices of "duration" $\delta = \tau/M$, in such a way that the value of the evolved wave function on a generic many-body state of the system reads

$$\Psi_\tau(x_0) = \sum_{x_1 \dots x_M} \prod_{i=1}^{M} G^\delta_{x_{i-1}x_i} \Phi_0(x_M), \tag{2.1.3}$$

where we have introduced the imaginary-time propagators

$$G^\delta_{x_{i-1}x_i} = \langle x_{i-1}|e^{-\tau\mathcal{H}}|x_i\rangle. \tag{2.1.4}$$

Within this approach, it is easy to write expectation values of operators $\mathcal{O}$ that are diagonal in the chosen basis $|x\rangle$, i.e., $\langle x|\mathcal{O}|y\rangle = O(x)\delta_{x,y}$. In fact, in this case we have that:

$$\langle\mathcal{O}\rangle = \lim_{\tau\to\infty} \frac{\sum_{\mathbf{X}} \Pi^\tau(\mathbf{X}) O(x_M)}{\sum_{\mathbf{X}} \Pi^\tau(\mathbf{X})}, \tag{2.1.5}$$

where the sum is extended to all possible imaginary-time paths $\mathbf{X} \equiv \{x_0, x_1, \dots, x_{2M}\}$, and the pseudo-probability $\Pi^\tau(\mathbf{X})$ is given by:

$$\Pi^\tau(\mathbf{X}) = \Phi_0(x_0) \left[\prod_{i=1}^{2M} G^\delta_{x_{i-1}x_i}\right] \Phi_0(x_{2M}). \tag{2.1.6}$$

The ground-state energy can be conveniently obtained by means of the so-called *mixed average* over the pseudo-probability, namely:

$$E_0 = \lim_{\tau\to\infty} \frac{\sum_{\mathbf{X}} \Pi^\tau(\mathbf{X}) E_L(x_0)}{\sum_{\mathbf{X}} \Pi^\tau(\mathbf{X})}, \tag{2.1.7}$$

where $E_L(x) = \langle x|\mathcal{H}|\Phi_0\rangle / \langle x|\Phi_0\rangle$ is referred as the *local energy*.

Besides the static (i.e., equal-time) correlation functions, this formalism allows one to calculate also the dynamical correlation functions (structure factors) in imaginary time $C_{AB}(\bar\tau) = \langle\mathcal{A}(\bar\tau)\mathcal{B}(0)\rangle$ introduced in 1.3.3, that can be computed as

$$C_{AB}(\bar\tau) = \lim_{\tau\to\infty} \frac{\sum_{\mathbf{X}} \Pi^\tau(\mathbf{X}) \mathcal{A}\left(x_{n+\bar\tau/\delta}\right) \mathcal{B}(x_n)}{\sum_{\mathbf{X}} \Pi^\tau(\mathbf{X})}, \tag{2.1.8}$$

where x_n is a coordinate of the path and the operators $\mathcal{A}$ and $\mathcal{B}$ are separated by an imaginary-time lag $\bar\tau$.

2.2 Reptation Quantum Monte Carlo

The expectation values in Eqs. (2.1.5), (2.1.7), and (2.1.8) suggest a probabilistic interpretation provided that $\Pi^\tau(\mathbf{X}) \geq 0$ for all the paths $\mathbf{X}$. Indeed, in this case, $\Pi^\tau(\mathbf{X})$ can be interpreted as a proper probability distribution that may be readily sampled by using Monte Carlo algorithms. This fact allows ground-state expectation values and dynamical correlations to be calculated exactly, within statistical errors.

The basic idea of the reptation quantum Monte Carlo algorithm is to sample the distribution probability $\Pi^\tau(\mathbf{X})$ by using a Markov process with simple moves. Given the path $\mathbf{X}_I \equiv \{x_0, x_1, \dots, x_{2M}\}$, a new path is proposed in two possible ways: either $\mathbf{X}_L \equiv \{x_F, x_0, \dots, x_{2M-1}\}$ (which we call "left move") or $\mathbf{X}_R \equiv \{x_1, \dots, x_{2M}, x_F\}$, (which we call "right move"). In both cases, x_F is a new configuration proposed according to a suitable transition probability $R^\delta(x_d \to x_F)$, where x_d stays for x_0 (x_{2M}) when the left (right) move is considered. Such "sliding moves" are depicted in Fig. 2.2.1. Ideally, the transition probability should guarantee the minimum possible statistical error on the desired observables and, to such a purpose, it has been proved useful to consider the propagator with importance sampling, i.e., $\tilde{G}^\delta_{xy} = G^\delta_{xy} \Phi_0(y)/\Phi_0(x)$ resulting in the following transition probability

$$R^\delta(x \to y) = \frac{\tilde{G}^\delta_{xy}}{w(x)}, \tag{2.2.1}$$

where

$$w(x) = \sum_{x'} \tilde{G}^\delta_{xx'} \tag{2.2.2}$$

is a normalization factor. The explicit form of $R^\delta(x_d \to x_F)$ will be discussed in more detail in Sec. 2.2.2. The proposed path $\mathbf{X}_d$ (where $d = L$ or R) is accepted or rejected according to the usual Metropolis algorithm, where the acceptance rate is given by:

$$A = \min\left\{1\,,\; \frac{\Pi^\tau(\mathbf{X}_d) R^\delta(x_F \to x_d)}{\Pi^\tau(\mathbf{X}_I) R^\delta(x_d \to x_F)}\right\}. \tag{2.2.3}$$

In this way, a sequence of configurations $\mathbf{X}^k$ is generated, k being the (discrete) sequential index of the Markov chain.

In order to reduce the auto-correlation time of the observables it is convenient to make several consecutive sliding moves along the same imaginary time direction. [8] To such a purpose, a recent development called "bounce" algorithm has been proposed. [102] The reptation quantum Monte Carlo algorithm with bounce moves can be then summarized in the following steps:

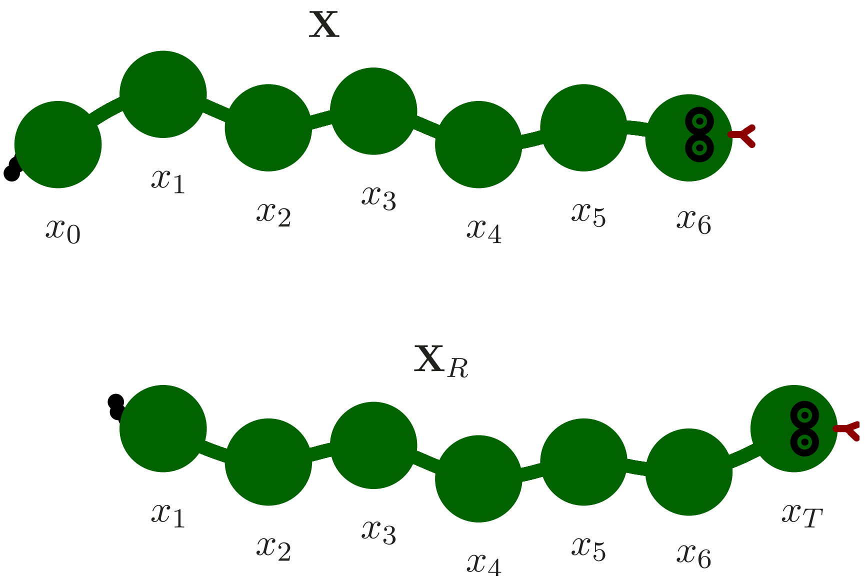

Fig. 2.2.1 Pictorial representation of the "sliding moves" along the right imaginary time direction. In the new configuration (bottom), a new head for the reptile is generated from the old configuration (top) and the tail is discarded.

1. For the current direction of the move and for the present configuration $\mathbf{X}^k$, propose x_F according to the transition probability $R^\delta(x_d \to x_F)$, where $x_d = x_0^k$ if $d = L$ and $x_d = x_{2M}^k$ if $d = R$.
2. Given the form of the acceptance ratio A of Eq. (2.2.3), accept the proposed configuration according to the probability
$$A_L = \min\left\{1\,,\ \frac{w(x_0^k)}{w(x_{2M-1}^k)}\right\}, \tag{2.2.4}$$
if $d = L$, or with probability
$$A_R = \min\left\{1\,,\ \frac{w(x_{2M}^k)}{w(x_1^k)}\right\}, \tag{2.2.5}$$
if $d = R$.
3. If the move is accepted, update the path configurations according to $\mathbf{X}^{k+1} = \mathbf{X}_d$ and continue along the same direction, otherwise $\mathbf{X}^{k+1} = \mathbf{X}^k$ and change direction.
4. Cycle to 1.

Although the bounce algorithm sampling procedure does not fulfill the microscopic detailed balance, the equilibrium probability distribution $\Pi^\tau(\mathbf{X})$ is nonetheless correctly sampled, as shown in Ref. [102].

2.2.1 Directed Updates

At this point we present a novel alternative sampling approach, which generalizes the bounce idea while strictly fulfilling the detailed balance condition. Such a scheme, which is largely inspired by the *loop algorithm* methods devised for the stochastic series expansion [117, 135] and for the *worm algorithm*, [114, 112] allows one to choose the time direction in a purely Markovian way, i.e., independently of the previous history.

In our algorithm, a Markov step consists of many simple consecutive "sliding moves", whose number is not fixed *a-priori* but is determined by a certain probability (see below). The actual Monte Carlo step takes place at the end of few consecutive updates along the currently chosen direction. In the examples below, we denote the number of these sliding moves between two Monte Carlo steps by s.

At the beginning of each Markov step we choose a direction d according to the probability $P\left(d\,|\,\mathbf{X}^k\right)$, whose form will be specified later. Assuming that the right direction has been chosen, we propose a new configuration x_F, according to the transition probability $R^\delta(x^k_{2M} \to x_F)$ and the configuration labels are shifted according to $\mathbf{X}^{k+1} = \{x^k_1, \dots, x^k_{2M}, x_F\}$, with $x^{k+1}_{2M} = x_F$. At this point, we continue the updates along this direction with probability $K\left(R\,,\,\mathbf{X}^{k+1}\right)$, or stop with probability $[1 - K\left(R\,,\,\mathbf{X}^{k+1}\right)]$. If it has been decided to continue the updates, then a new configuration is generated according to $R^\delta(x^{k+1}_{2M} \to x_F)$ and the labels of the configuration are again shifted according to $\mathbf{X}^{k+2} = \{x^{k+1}_1, \dots, x^{k+1}_{2M}, x_F\}$. The Markov step then finishes after a certain number of s consecutive updates along the right direction. At this stage a Metropolis test should be done, in order to accept or reject the sequence of intermediate s sliding moves:

$$A = \min\left\{1, \frac{q(\mathbf{X}^{k+s})}{q(\mathbf{X}^k)}\right\}, \tag{2.2.6}$$

where (see Appendix A.1 for details)

$$\begin{aligned} q(\mathbf{X}) &= \frac{P\left(L\,|\,\mathbf{X}\right)}{1 - K\left(R\,,\,\mathbf{X}\right)} w(x_{2M-1}) \\ &= \frac{P\left(R\,|\,\mathbf{X}\right)}{1 - K\left(L\,,\,\mathbf{X}\right)} w(x_1). \end{aligned} \tag{2.2.7}$$

However, in order to avoid time-consuming restorations of the original configuration, it is preferable to accept all the moves, while keeping track of the residual weight $q(\mathbf{X})$. This is possible since A only depends upon initial and final configurations, so that, given that all the intermediate moves are accepted, the sampled equilibrium distribution probability is $\Pi^\tau(\mathbf{X}) \times q(\mathbf{X})$. The contribution of the current configuration to statistical averages must be then weighted by the factor $1/q(\mathbf{X})$. To proceed to the next Markov step, a new direction d is chosen according to $P\left(d\,|\,\mathbf{X}^{k+s}\right)$ and the updates are carried along the extracted new direction.

In Appendix A.1, it is demonstrated that the detailed balance is satisfied if one chooses the probabilities for the directions as

$$P\,(L\,|\,\mathbf{X}) = \frac{1}{1+a(\mathbf{X})}, \tag{2.2.8}$$

$$P\,(R\,|\,\mathbf{X}) = \frac{a(\mathbf{X})}{1+a(\mathbf{X})}, \tag{2.2.9}$$

where

$$a(\mathbf{X}) = \frac{w(x_{2M-1})}{w(x_1)}\,\frac{1-K(L\,,\,\mathbf{X})}{1-K(R\,,\,\mathbf{X})}, \tag{2.2.10}$$

which is positive and, therefore, guarantees that the above defined quantities are well defined probabilities, i.e., $0 \leq P\,(L\,|\,\mathbf{X}) \leq 1$ and $0 \leq P\,(R\,|\,\mathbf{X}) \leq 1$, with the additional property that $P\,(L\,|\,\mathbf{X}) + P\,(R\,|\,\mathbf{X}) = 1$.

Regarding the probabilities to continue the updates along the current direction, we have a substantial freedom of choice, provided that the condition $\frac{K(L\,,\,\mathbf{X})}{K(R\,,\,\mathbf{X})} = \frac{w(x_1)}{w(x_{2M-1})}$, is satisfied. The particular choice we have adopted is

$$K(L\,,\,\mathbf{X}) = \alpha \min\left\{1, \frac{w(x_1)}{w(x_{2M-1})}\right\}, \tag{2.2.11}$$

$$K(R\,,\,\mathbf{X}) = \alpha \min\left\{1, \frac{w(x_{2M-1})}{w(x_1)}\right\}, \tag{2.2.12}$$

where $0 < \alpha < 1$ is an arbitrary parameter of the algorithm, which controls the average number of consecutive updates along the same direction.

Summarizing, the reptation quantum Monte Carlo algorithm with directed updates consists of a sequence of Markov steps determined by the following rules:

1. Choose a time direction d according to the probabilities of Eqs. (2.2.8) and (2.2.9).
2. Propose a new configuration x_F according to the transition probability $R^{\delta}(x_d \to x_F)$, where $x_d = x_0^k$ if $d = L$ and $x_d = x_{2M}^k$ if $d = R$.
3. Shift the configuration indexes according to $\mathbf{X}^{k+1} = \{x_F, x_0^k, \ldots, x_{2M-1}^k\}$ if $d = L$ or $\mathbf{X}^{k+1} = \{x_1^k, \ldots, x_{2M}^k, x_F\}$ if $d = R$.
4. According to the probability $K(L\,,\,\mathbf{X}^k)$ or $K(R\,,\,\mathbf{X})$, decide whether keep moving in the same direction or change direction. In the former case, go to 2, otherwise go to 5.
5. The Markov step ends here and the current configuration carries the weight $1/q(\mathbf{X}^{k+s})$, where s is the number of intermediate moves along the direction chosen.

The relationship between the directed update scheme and the bounce algorithm is further elucidated in the Appendix A.1, where general considerations about the efficiency of the algorithms are also presented.

2.2.2 Continuous-Time Propagator

One of the most striking differences between the original formulation of the reptation quantum Monte Carlo on the continuum and the present formulation on the lattice is the lack of the discretization error appearing in the Trotter decomposition of the propagator. Indeed it is easier to carry the propagation in continuous imaginary time on a lattice, [130] than on the continuum. [121] To such a purpose, let us consider the limit of an infinitesimal imaginary time ϵ, for which the transition probability of Eq. (2.2.1) can be written as

$$\begin{aligned} R^{\epsilon}(x \to y) &\simeq \frac{\delta_{xy} - \epsilon \Phi_0(y) H_{xy} / \Phi_0(x)}{1 - \epsilon E_L(x)} && (2.2.13) \\ &\simeq \delta_{xy}\left[1 + \epsilon E_L(x)\right] - \epsilon \left[H_{xy} \frac{\Phi_0(y)}{\Phi_0(x)}\right] + o(\epsilon^2), && (2.2.14) \end{aligned}$$

where $E_L(x)$ is the previously defined local energy and $H_{x,y} = \langle x|H|y\rangle$ denotes the matrix elements of the Hamiltonian. Whenever $\Phi_0(y)H_{xy}/\Phi_0(x)$ is *non positive* for all x and y, this equation takes the form of a continuous-time Markov process, whose analytical properties are well known. In particular, the probability distribution for the "waiting time" τ_w in a given state x, i.e., the average time that the system spends in the state x before making an off-diagonal transition to another state $y \neq x$, is exactly known, namely $P(\tau_w; x) = \exp\{-\tau_w [H_{xx} - E_L(x)]\}$. As a consequence, the finite-time propagator $R^{\delta}(x \to y)$ can be directly sampled, giving rise to a succession of a certain number n of consecutive transitions $x \to z_1 \to z_2 \to \cdots \to y$, with corresponding waiting times $\tau_w(z_i)$ (such that $\sum_i \tau_w(z_i) = \delta$). The normalization of the whole process is

$$w(x) = \exp\left[-\sum_i \tau_w(z_i) E_L(z_i)\right], \tag{2.2.15}$$

where the waiting times are extracted according to the exponential probability $P(\tau_w; z_i)$. The transitions between the intermediate configurations are done according to the off-diagonal elements of Eq. (2.2.14), i.e., z_{i+1} is chosen with probability proportional to $-H_{z_i z_{i+1}} \frac{\Phi_0(z_{i+1})}{\Phi_0(z_i)}$.

2.2.3 Non-Diagonal Observables

The formalism so-far developed allows one to successfully compute *pure* ground-state expectation values of operators that are *diagonal* in the local basis x, with the expectation values of non-diagonal operators restricted to the so-called *mixed averages*. [8, 118, 130] Nonetheless, it is often of great interest to remove such a limitation (whose result is biased by the quality of the variational wave function) and a dedicated sampling strategy has to be devised in order to cope with such a need. In the following, we show that a relatively easy modification of the sampling scheme can accomplish this task, providing us with a general tool to compute ground-state averages of operators that are non local in the chosen basis x.

We consider an arbitrary non-diagonal observable $\mathcal{O}$ and, in the spirit of Refs [112, 115], we introduce a *worm operator* defined by

$$\mathcal{W}_{x,y} = \delta_{x,y} + \lambda \mathcal{O}_{x,y}, \tag{2.2.16}$$

where λ is a positive constant and consider the extended configuration space spanned by the probability distribution

$$\begin{aligned} \Pi^{\tau}_{\mathcal{W}}(\mathbf{X}) = \Phi_0\left(x_0\right) \times \prod_{i=1}^{L} G^{\delta}_{x_{i-1}x_i} \times \mathcal{W}_{x_L x_R} \times \\ \times \prod_{i=R+1}^{2M+1} G^{\delta}_{x_{i-1}x_i} \times \Phi_0\left(x_{2M+1}\right). \end{aligned} \tag{2.2.17}$$

At variance with Eq. (2.1.6), the worm operator now breaks the imaginary-time paths into two distinct pieces. The discontinuity is realized at the imaginary time $0 \le \tau_{LR} \le \tau$, where the worm operator sits and the paths contain $2(M+1)$ configurations, including x_L and x_R that refer to the same imaginary time τ_{LR}. The path space in which Eq. (2.2.17) is defined is clearly larger than the support of Eq. (2.1.6), which is recovered whenever $x_L = x_R$, i.e., when the worm operator is *diagonal*.

The pure ground-state expectation value of the operator $\mathcal{O}$ is conveniently written in terms of the extended paths as

$$\langle \mathcal{O} \rangle = \frac{1}{\lambda} \lim_{\tau \to \infty} \frac{\sum_{\mathbf{X}} \Pi^{\tau}_{\mathcal{W}}(\mathbf{X}) \times \Theta(x_L \neq x_R)}{\sum_{\mathbf{X}} \Pi^{\tau}_{\mathcal{W}}(\mathbf{X}) \times \Theta(x_L = x_R)}, \tag{2.2.18}$$

where $\Theta(C) \neq 0$ whenever condition C is satisfied. The modulus of Eq. (2.2.17) can be in turn interpreted as a probability distribution and sampled stochastically by means of the elementary sliding moves considered before. Indeed, whenever the worm operator is far from the ends of the imaginary-time paths, the sampling scheme remains unchanged. In this case, a move along direction d will generate a new head (or tail) for the reptile according to $R^{\delta}(x \to x_F)$ while shifting the worm position of $\pm\delta$. On the other hand, whenever the worm operator reaches the ends of the reptile, a new worm configuration is proposed on the opposite side. In analogy with the previous analysis, new configurations are generated according to a transition probability

$$R^{\mathcal{W}}(x \to y) = \frac{1}{\bar{w}(x)} \left| \mathcal{W}_{xy} \frac{\Phi_0(y)}{\Phi_0(x)} \right|, \tag{2.2.19}$$

where $\bar{w}(x)$ is a normalization factor. Due to the particular form of the matrix elements (2.2.16), the transition probability will lead either to diagonal configurations $(x = y)$ or to non-diagonal configurations ($x \neq y$), thus generating continuous and discontinuous paths. The relative probability for diagonal and non-diagonal configurations depends on the value of λ that can be tuned in order to reach a balanced sampling frequency for the different sectors of the extended paths. In order to exemplify the worm updates, let us consider the case in which $d = R$ and a path with probability $\Phi_0(x_0)\,\mathcal{W}_{x_0 x_1}\left[\prod_{i=2}^{2M+1} G^{\delta}_{x_{i-1}x_i}\right]\Phi_0(x_{2M+1})$, after a sliding update in the right direction, we will have $\Phi_0(x_1)\left[\prod_{i=2}^{2M+1} G^{\delta}_{x_{i-1}x_i}\right]\mathcal{W}_{x_{2M+1}x_F}\Phi_0(x_F)$, where x_F is proposed according to the transition probability $R^{\mathcal{W}}(x_{2M+1} \to x_F)$ (see Fig. 2.2.2). In analogy with the previous case, the acceptance factor for the bounce moves reads $\bar{A}_R = \min\left\{1\,,\ \frac{\bar{w}(x_{2M+1})}{\bar{w}(x_1^k)}\right\}$.

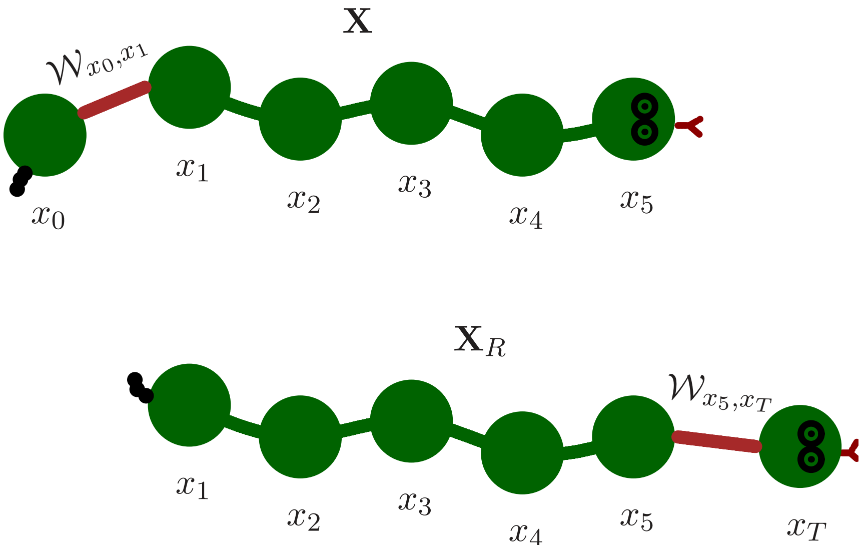

Fig. 2.2.2 Pictorial representation of the “sliding moves” along the right imaginary-time direction when the worm operator sits at the tail of the reptile. In the new configuration (bottom), a new head for the reptile is generated from the old configuration (top), the old tail configuration is discarded and the worm discontinuity is moved to the “neck” of the reptile.

Summarizing, the reptation quantum Monte Carlo with worm-updates consists of the following steps:

1. For the current direction of the move d and for the present configuration $\mathbf{X}^k$ consider the worm-operator position τ_{LR}.
2. If the worm is not at the ends of the reptile (i.e., $\tau_{LR} \neq 0$ when $d = L$ and $\tau_{LR} \neq \tau$ when $d = R$) go to step (a), otherwise go to step (b).

   a. Propose a new configuration x_F according to the transition probability $R^{\delta}(x_d \to x_F)$, where $x_d = x_0^k$ if $d = L$ and $x_d = x_{2M+1}^k$ if $d = R$. The new configuration is accepted with probability

$$A_L = \min\left\{1\,,\ \frac{w(x_0^k)}{w(x_{2M}^k)}\right\}, \qquad (2.2.20)$$

if $d = L$, or with probability

$$A_R = \min\left\{1\,,\ \frac{w(x^k_{2M+1})}{w(x^k_1)}\right\}, \tag{2.2.21}$$

if $d = R$. In the proposed state $\mathbf{X}_d$, all the configuration labels are shifted in the d direction, determining in turn a shift of the worm operator of a time interval $\pm\delta$, depending on d.

b. Propose a new configuration x_F according to the worm transition probability $R^{\mathcal{W}}(x_d \to x_F)$, where $x_d = x^k_L = x^k_0$ if $d = L$ and $x_d = x^k_R = x^k_{2M+1}$ if $d = R$. Accept the new configuration with probability

$$\bar{A}_L = \min\left\{1\,,\ \frac{\bar{w}(x^k_0)}{\bar{w}(x^k_{2M})}\right\}, \tag{2.2.22}$$

if $d = L$, or with probability

$$\bar{A}_R = \min\left\{1\,,\ \frac{\bar{w}(x^k_{2M+1})}{\bar{w}(x^k_1)}\right\}, \tag{2.2.23}$$

if $d = R$. In the proposed path $\mathbf{X}_d$, all the configuration labels are shifted in the d direction, and the worm operator is moved from the head (tail) to the tail (head) of the reptile, depending on d.

3. If the move is accepted, update the path configurations according to $\mathbf{X}^{k+1} = \mathbf{X}_d$ and continue along the same direction, otherwise $\mathbf{X}^{k+1} = \mathbf{X}^k$ and change direction.
4. Cycle to 1.

This scheme samples the probability density associated to the modulus of Eq. (2.2.17), and the expectation value of $\mathcal{O}$ can be recast as a statistical average over such a probability distribution, while keeping track of the overall sign of the extended paths. In particular the best estimate of the ground-state expectation values is obtained when the worm is in the central part of the path, at $\tau_{LR} = \tau/2$, leading to

$$\begin{aligned}\langle \mathcal{O} \rangle &= \frac{\sum_{\mathbf{X}} \Pi^{\tau}_{\mathcal{W}}(\mathbf{X}) \times \Theta\left(\mathcal{O}_{x_L x_R} \neq 0,\, \tau_{LR} = \frac{\tau}{2}\right)}{\sum_{\mathbf{X}} \Pi^{\tau}_{\mathcal{W}}(\mathbf{X}) \times \Theta\left(x_L = x_R,\, \tau_{LR} = \frac{\tau}{2}\right)} \\ &= \frac{1}{\lambda} \frac{\langle \Theta\left(\mathcal{O}_{x_L x_R} \neq 0\right) \times \text{sign}\left[\Pi^{\tau}_{\mathcal{W}}(\mathbf{X})\right] \rangle^{\text{center}}_{\text{OD}}}{N^{\text{center}}_D},\end{aligned} \tag{2.2.24}$$

where $\langle \ldots \rangle^{\text{center}}_{\text{OD}}$ denotes statistical averages over the non-diagonal distribution $|\Pi^{\tau}_{\mathcal{W}}(\mathbf{X})|\, \Theta(x_L \neq x_R,\, \tau_{LR} = \frac{\tau}{2})$ and N^{center}_D is the number of configurations sampled with a diagonal worm operator in the center of the paths.

2.2.4 Fixed-Node Approximation and Systematic Improvements

When the probability distribution of Eq. (2.1.6) is not positive defined, as is generally the case with fermions, the probabilistic interpretation of the imaginary-time paths breaks down. This circumstance, which is known as the *sign problem*, originates whenever $\Phi_0(y)H_{xy}/\Phi_0(x) > 0$ for some element $x \neq y$. In this case, it is not possible to have polynomial algorithms that are able to obtain an *exact* solution of the problem, which would imply to sample correctly the resulting signs. Therefore, approximated schemes are welcome and often adopted, the most widespread one being the so-called fixed-node approximation. For lattice systems, this approach relies on the definition of an effective Hamiltonian, which depends parametrically on the nodal structure of a variational wave function $\Phi_0(x) = \langle x|\Phi_0\rangle$. [140] The matrix elements of the fixed-node Hamiltonian are defined as

$$H^{\text{fn}}_{xy} = \begin{cases} H_{xx} + \nu_{\text{sf}}(x) & \text{if } x = y \\ H_{xy} & \text{if } \Phi_0(y)H_{xy}\Phi_0(x) \leq 0 \\ 0 & \text{if } \Phi_0(y)H_{xy}\Phi_0(x) > 0 \end{cases} \tag{2.2.25}$$

where the sign-flip potential is $\nu_{\text{sf}}(x) = \sum_{y:\text{sf}} \Phi_0(y)H_{xy}/\Phi_0(x)$, the sum being extended to all the sign-flip states defined by the condition $\Phi_0(y)H_{xy}\Phi_0(x) > 0$. With such a choice, the transition matrix $R^{\delta}(x \to y)$ of Eq. (2.2.14) is always positive definite and the sum of Eq. (2.1.3) is now restricted to a region of the configuration space in which imaginary-time paths have positive-definite weights, thus resulting in the fixed-node *approximation*. Therefore, within the fixed-node approximation, the ground-state wave function $|\Psi^{\text{fn}}\rangle$ of $\mathcal{H}^{\text{fn}}$ can be stochastically sampled without any sign problem. The fixed-node approximation becomes exact whenever the signs of the exact ground state are known and, most importantly, it has been proven [140] that the fixed-node ground-state energy $E^{\text{fn}} = \langle \mathcal{H}^{\text{fn}}\rangle$ gives a rigorous upper-bound to the exact ground-state one and improves the pure variational results.

At this point, we introduce a straightforward, although computationally expensive, way to improve upon the fixed-node energy. Our strategy amounts to compute the expectation values of arbitrary powers of the original Hamiltonian $\mathcal{H}$ on the fixed-node ground state $|\Psi_{\text{fn}}\rangle$, namely

$$L_k = \frac{\langle \Psi_{\text{fn}}|\mathcal{H}^k|\Psi_{\text{fn}}\rangle}{\langle \Psi_{\text{fn}}|\Psi_{\text{fn}}\rangle}. \tag{2.2.26}$$

The fixed-node ground state can be expanded in the basis set of the eigenstates of $\mathcal{H}$ as $|\Psi_{\text{fn}}\rangle = \gamma_0|\Psi_0\rangle + \gamma_1|\Psi_1\rangle + \gamma_2|\Psi_2\rangle + \ldots$ and $L_k = \gamma_0^2 E_0^k + \gamma_1^2 E_1^k + \gamma_2^2 E_2^k + \ldots$, with $\sum_i \gamma_i^2 = 1$. Since very often the fixed-node wave function has a considerable overlap with only few low-energy states, the knowledge of the first few moments of the Hamiltonian are enough to approximately reconstruct both the coefficients γ_i and the energies E_i. To such a purpose, let us consider a typical situation in which only the first $2n$ moments of the Hamiltonian have been numerically calculated and are therefore known. We can then truncate the expansion for L_k to the order $n-1$ having a closed system of $2n$ equations

$$L_k = \sum_{i=0}^{n-1} \gamma_{i,n}^2 E_{i,n}^k, \tag{2.2.27}$$

for $k = 0, \ldots 2n-1$ that can be solved for the unknowns $\gamma_{i,n}$ and $E_{i,n}$. In the limit of large n, the approximated $E_{0,n}$ converges to the exact ground-state energy. Moreover, we verified that $E_{0,n} \geq E_0$, as a result of a connection between the solutions of the Eq. (2.2.27) and the variational Lanczos procedure written in terms of the moments of the Hamiltonian. [150]

The Hamiltonian moments are non-diagonal operators and can, in principle, measured according to the sampling procedure detailed in Sec. 2.2.3. In the present implementation we are able to achieve sufficient statistical accuracy only for the first moment of the Hamiltonian, i.e., $L_1 = \langle \mathcal{H} \rangle$, while higher moments are too noisy. Yet, to our knowledge our algorithm is the only one that allows the calculation of the expectation value of the *original* Hamiltonian $\mathcal{H}$. This is known [140] to be a better upper bound than the expectation value of the fixed-node Hamiltonian accessible with other zero-temperature algorithms.

Although we are not currently in position to measure directly the Hamiltonian moments L_k we have a controlled access to the *mixed averages*

$$L_k^{\text{mix}} = \frac{\langle \Psi_{\text{fn}} | \mathcal{H}^k | \Phi_0 \rangle}{\langle \Psi_{\text{fn}} | \Phi_0 \rangle}, \tag{2.2.28}$$

which present optimal statistical uncertainty. Moreover, an improved estimate of the ground-state energy based on the knowledge of the first few moments L_k^{mix} can be obtained solving a system of equation similar to Eq. (2.2.27) that leads to the approximate ground-state energies $E_{i,n}^{\text{mix}}$. Unfortunately, it is difficult to prove (or disprove) that $E_{i,n}^{\text{mix}} \geq E_0$, for $n > 1$, requiring a generalization of the already non-trivial upper bound for $n = 1$ described in Ref. [140]. Nonetheless, we have numerically verified that, in all the cases discussed in this Chapter (where E_0 is *a-priori* known), the condition $E_{i,n}^{\text{mix}} \geq E_0$ is always verified. We are then led to conjecture that this may always be the case.

2.3 Case Studies

2.3.1 Low-Energy Excitations and Spin Correlations of the Heisenberg Model

Hereafter, we present a simple application of the previous ideas to sign-problem free spin Hamiltonians. Let us consider the one-dimensional quantum Heisenberg model

$$\mathcal{H} = J \sum_i \boldsymbol{\mathcal{S}}_i \cdot \mathbf{S}_{i+1}, \tag{2.3.1}$$

where $\boldsymbol{\mathcal{S}}_i = (\mathcal{S}_i^x, \mathcal{S}_i^y, \mathcal{S}_i^z)$ is the spin 1/2 operator on the site i and $J > 0$ is the nearest-neighbor super-exchange coupling.

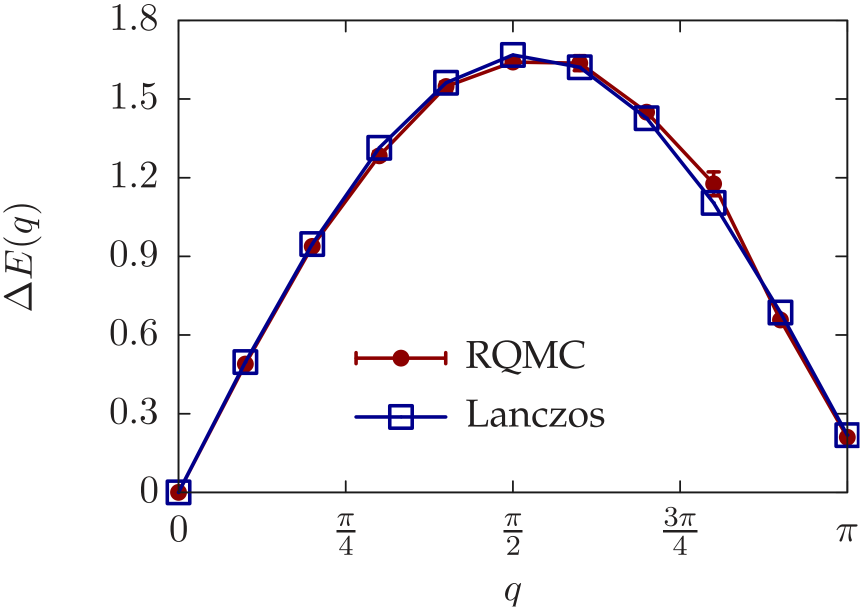

Fig. 2.3.1 Lowest-energy excitations as a function of the wave-vector q for an $L = 20$ Heisenberg chain. The energies are extracted from the dynamical structure factor $S(q, \omega)$ and are compared to exact results by the Lanczos method.

The total number of sites is denoted by L and periodic-boundary conditions are assumed. This model can be solved exactly by using the so-called Bethe ansatz technique. [See for example, 58] Information on the excitation spectrum can be obtained from the dynamic structure factor

$$S(q, \omega) = \int dt \langle \mathcal{S}_q^z(t) \mathcal{S}_{-q}^z(0) \rangle e^{i\omega t}, \tag{2.3.2}$$

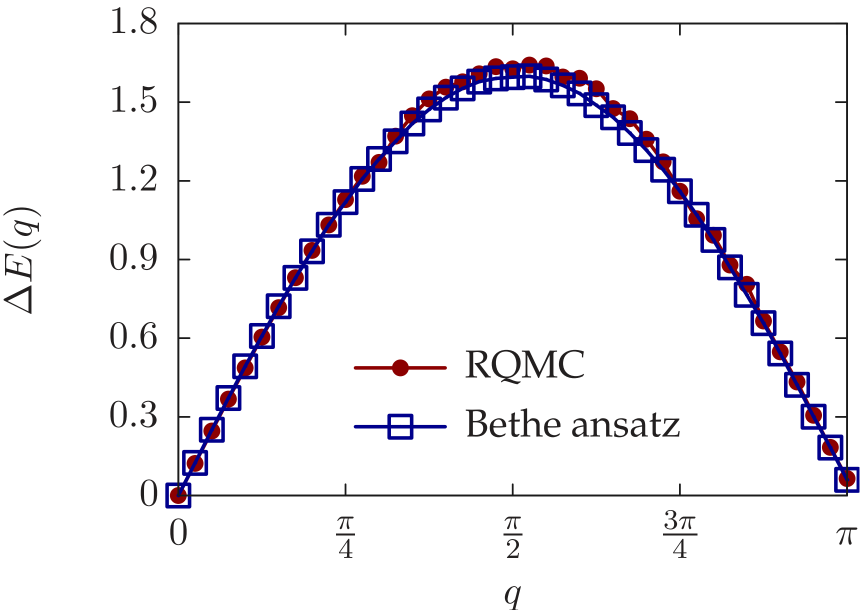

Fig. 2.3.2 The same as in Fig. 2.3.1 for $L = 80$. Exact results are given by Bethe ansatz.

where $\mathcal{S}^z_q(t) = 1/\sqrt{L}\sum_j \mathcal{S}^z_j(t)e^{iqj}$ is the Fourier transform of time-evolved z-component of the spin operator. By introducing a complete set of eigenstates of the Hamiltonian $|\Psi_n\rangle$ with eigenvalues E_n, we have that

$$S(q,\omega) = \sum_{n\neq 0} |\langle \Psi_0|\mathcal{S}^z_q|\Psi_n\rangle|^2 \delta(\omega - \omega_n), \tag{2.3.3}$$

where $\omega_n = (E_n - E_0)$. In the thermodynamic limit, the spin-1 states form a branch, which is very similar to spin waves in standard ordered systems, although no long-range order is found in one dimension.

Imaginary-time correlation functions of arbitrary (diagonal) operators can be efficiently evaluated via Eq. (2.1.8). This fact allows us to have a direct access to $S(q,\bar{\tau}) = \langle \mathcal{S}^z_q(\bar{\tau})\mathcal{S}^z_{-q}(0)\rangle$. This imaginary-time correlation function can be then analytically continued, by using the Maximum Entropy method described in 1.3.4. This procedure allows us to have a reasonably accurate numerical estimate for the dynamic structure factor of Eq. (2.3.3).

Before presenting the results, let us mention that we consider the following Jastrow state as a variational wave function: [84, 55]

$$|\Phi_0\rangle = \exp\left[\sum_{i,j} v_{ij}\mathcal{S}^z_i\mathcal{S}^z_j\right]|FM\rangle \tag{2.3.4}$$

where $|FM\rangle$ is the ferromagnetic state along the x direction, for which $\langle x|FM\rangle$ does not depend upon the spin configuration and the variational parameters v_{ij} are optimized by using the method of Ref. [128].

In Fig. 2.3.1, we show the results for a small ($L = 20$) system, where exact diagonalization is possible by using the Lanczos method. We report the energy excitations $\Delta E(q) = E_q - E_0$ for the lowest state with $S = 1$ and fixed momentum q. In this case an excellent agreement between our reptation quantum Monte Carlo results and the exact ones is found. Moreover, also on larger systems a very good accuracy is attained (see Fig. 2.3.2), demonstrating the performances of our numerical algorithm.

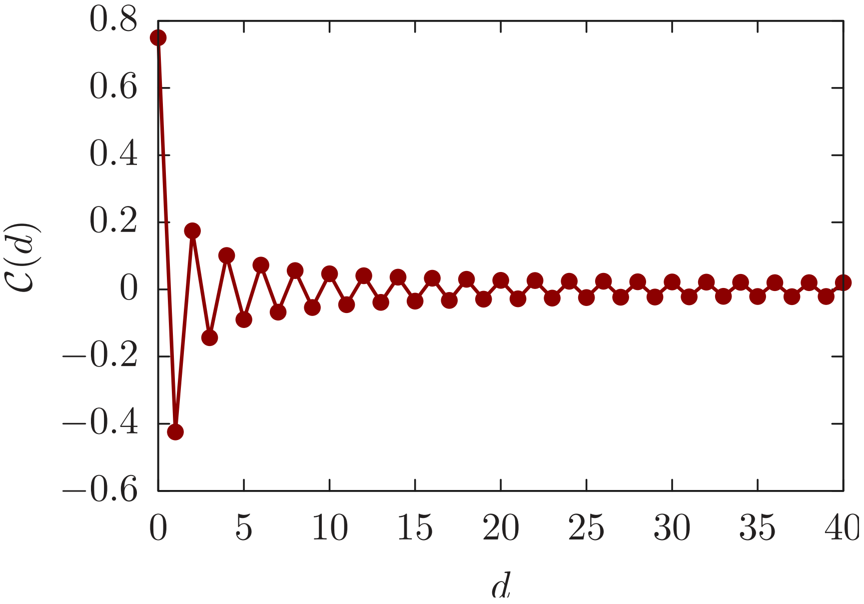

Fig. 2.3.3 Ground-state expectation value of the spin-spin correlation function $\mathcal{C}(d)$ for the Heisenberg model on a 80-site chain.

In order to exemplify the potentialities of the scheme outlined in 2.2.3, we conclude this part of the results devoted to the Heisenberg model showing the ground-state expectation value of the spin-spin correlation at distance d

$$\mathcal{C}(d) = \frac{1}{L}\sum_i \left(\hat{\mathbf{S}}_i \cdot \hat{\mathbf{S}}_{i+d}\right). \tag{2.3.5}$$

The desired observable is used as a worm operator and the value of the correlation function at the various distances is computed by means of the estimator of Eq. (2.2.24). In Fig. 2.3.3, we show the expectation value of $\mathcal{C}(d)$ for a 80-site one-dimensional lattice. In this case we are able to achieve very good statistics for the non-diagonal observable, with a relatively negligible computational effort, when compared to the evaluation of the ground-state expectation value of other diagonal observables.

2.3.2 Ground-State Properties of the Fermionic Hubbard Model

As an example of the application of the reptation quantum Monte Carlo to sign-problem affected Hamiltonians, we present some results for the fermionic Hubbard model on a square lattice, defined by:

$$\mathcal{H} = -t \sum_{\langle i,j \rangle,\sigma} \left(c^{\dagger}_{i,\sigma} c_{j,\sigma} + c^{\dagger}_{j,\sigma} c_{i,\sigma} \right) + U \sum_{i} n_{i,\uparrow} n_{i,\downarrow}, \tag{2.3.6}$$

where $\langle \dots \rangle$ indicate nearest-neighbor sites, $\hat{c}^{\dagger}_{i,\sigma}$ ($\hat{c}_{i,\sigma}$) creates (destroys) an electron on the site i with spin σ, and $n_{i,\sigma} = c^{\dagger}_{i,\sigma} c_{i,\sigma}$. As a variational state we consider

$$|\Phi_0\rangle = \exp\left[\sum_{i,j} v_{ij} n_i n_j \right] |FS\rangle \tag{2.3.7}$$

where $|FS\rangle$ is the non-interacting Fermi sea and the Jastrow factor involves density-density correlations. The variational parameters v_{ij} entering in the Jastrow factor may be optimized again by minimizing the variational energy with the method of Ref. [128]. In order to avoid open shells in $|FS\rangle$, we consider 45-degrees tilted lattices with $L = 2 \times l^2$ sites, such that both the half-filled case and selected holes-doped cases are closed shells.

Let us start by showing the results for 18 electrons on 18 sites, where Lanczos diagonalizations are possible. [11] In Fig. 2.3.4, we report our results for the ground-state energy. The fixed-node approach gives rather accurate results for small values the interaction ($U/t \lesssim 4$), where $(E_{\text{exact}} - E^{\text{fn}})/E_{\text{exact}} \lesssim 0.01$. By increasing the on-site interaction, the fixed-node approach becomes worse and worse. This fact is due to the choice of the variational wave function that does not contain antiferromagnetic order. Remarkably, a considerable improvement may be obtained by considering the *pure* expectation value of the Hamiltonian, which is systematically lower than the fixed-node energy, as demonstrated in Ref. [140] and now accessible within our algorithm. Further improvements to the fixed-node energy can be obtained upon considering few (up to three) higher moments of the Hamiltonian measured as mixed-averages, see Fig. 2.3.4. The scheme based upon the Hamiltonian moments (described in Sec. 2.2.4) allows us to reach a great accuracy for the ground-state energy, with a residual error almost independent of U/t. Indeed, in this way we have $(E_{\text{exact}} - E)/E_{\text{exact}} \lesssim 0.002$ up to $U/t = 8$.

This approach remains very effective also for larger systems, even though the variational wave function loses accuracy by increasing the cluster size (because the ground state has antiferromagnetic order in the thermodynamic limit, while the variational state is paramagnetic).

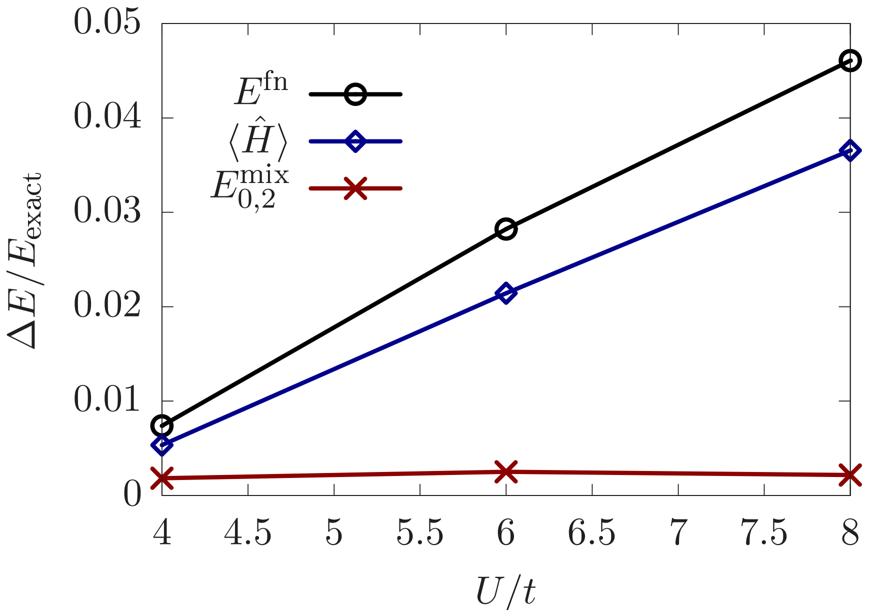

Fig. 2.3.4 Ground-state energy for the fermionic Hubbard model at half filling on a 18-sites tilted-square lattice. The energy difference $\Delta E = E_{\text{exact}} - E$ is computed with distinct approximations described in the text.

In Table 2.1, we report the ground-state energy for 50 sites for the half-filled case, while in Table 2.2 we report the ground-state energies for selected cases at finite hole-doping, where numerically exact results (for moderate values of U and moderate lattice sizes) can be obtained by the Auxiliary-Field Monte Carlo method. [129]

U/t	E^{fn}	$\langle\mathcal{H}\rangle$	$E_{0,2}^{\text{mix}}$
4	$-42.850(1)$	$-43.16(1)$	$-43.282(1)$
5	$-36.364(1)$	$-36.51(1)$	$-37.052(1)$
6	$-31.885(1)$	$-32.17(1)$	$-32.640(1)$
7	$-28.318(1)$	$-28.66(1)$	$-29.022(1)$
8	$-25.382(1)$	$-25.62(1)$	$-26.056(1)$

Table 2.1 Ground-state energy as a function of the Hubbard U repulsion on the 50-site lattice at half filling.

2.4 Conclusions

In this Chapter we have described an efficient and general formulation of the reptation quantum Monte Carlo technique on lattice models. In particular, we have shown an alternative sampling approach which generalizes the bounce algorithm, previously introduced to reduce

N	E^{fn}	$\langle\mathcal{H}\rangle$	$E^{\text{mix}}_{0,2}$	E_{AF}
50	$-42.850(1)$	$-43.16(1)$	$-43.282(1)$	$-43.983(1)$
42	$-53.402(1)$	$-53.57(1)$	$-53.769(1)$	$-54.001(1)$
26	$-55.4325(1)$	$-55.63(1)$	$-55.6112(1)$	$-55.782(1)$
18	$-50.4127(1)$	$-50.50(1)$	$-50.4383(1)$	$-50.474(1)$

Table 2.2 Ground-state energy as a function of the number of electrons N for Hubbard repulsion $U/t = 4$ on a 50-site lattice. The numerically exact results obtained by the Auxiliary-Field Monte Carlo method E_{AF} are also shown for comparison. [129]

auto-correlation time of the observables. Our scheme allows one to choose the time direction in a purely Markovian way. In addition, the average number of consecutive moves along the time directions may be optimized by a fine tuning of a certain parameter that has been expressly introduced in the transition probabilities. We reported benchmarks for two different models with pure bosonic and fermionic degrees of freedom, by showing to what extent it is possible to have accurate results both on the ground state and low-energy excitations. The introduction of a general method to compute ground-state expectation values of arbitrary non-diagonal observables also constitutes an important achievement, which will ease the study of relevant properties such as Bose-Einstein condensation and superconductivity phenomena in strongly interacting models. In addition, the possibility to directly measure the *pure* ground-state expectation values may open the way to a better optimization of the correlated wave function associated to the ground-state of an effective Hamiltonian which is not the fixed-node one.

Chapter 3

Quantum Spectral Properties From Imaginary-Time Dynamics

Lattice Dynamics of Helium 4

Particles obeying the Bose statistics often offer spectacular and unexpected manifestations of the quantum coherence on macroscopic scales, such as superfluidity and superconductivity. The structure of the excitations of strongly correlated bosonic systems determines in a substantial way their response to external probes and the very nature of the most purely quantum phenomena they give rise to. An intriguing case, in which such excited-state properties can be exploited by means of the imaginary-time dynamics methods outlined in the previous chapters, is the crystalline phase of Helium 4.[33]

Indeed, the non-trivial quantitative features of the excited-states play in this case a key role in the observed response to inelastic neutron scattering experiments which induce and therefore probe the collective density excitations. The lattice dynamics of solid ^{4}He has long been considered a major challenge to *ab initio* calculations, due to the strong anharmonicity of this highly quantum solid. Many calculations have been performed within the Self Consistent Phonon (SCP) approximation,[59, 61] which however may be rather unsatisfactory, due to the magnitude of anharmonic effects. A significant improvement has been later made possible by the application of a variational quantum Monte Carlo approach, based on the *shadow wave function* formalism, to *bcc* ^{3}He [86] and to *hcp* ^{4}He.[56] The variational nature of this approach, however, makes it not fully suitable at high energy where optical or zone-boundary longitudinal excitations exhibit broad multiphonon features. In this spectral regime, the calculation of the *full* dynamic structure factor is therefore in order. On the other hand, as we have seen in Chapter 1, quantum Monte Carlo path-integral techniques allow quite naturally for the calculation of imaginary-time correlation functions from which various spectral functions, such as the dynamic structure factor, can be obtained upon analytical continuation. This procedure has been successfully demonstrated for superfluid ^{4}He,[22, 8] as well as for the *bcc* crystalline phases of ^{4}He [131, 100] and ^{3}He.[132] In the latter studies the spectrum of the transverse excitations has also been obtained, albeit in the one-phonon approximation only.[61]

In this Chapter we present an application of the previously presented ideas to the lattice dynamics of solid helium. In particular, we will show an extensive study of the dynamical properties of *hcp* ^{4}He at zero temperature,[33] performed by estimating the dynamic structure factor from ground-state path-integral simulations. [36, 8, 118] This technique allows us to parallel to some extent the procedure followed experimentally to map phonon dispersions from the measured neutron scattering. In the long wave-length region—well approximated by a phonon picture of the collective density excitations—we thus obtain longitudinal as well as transverse modes for both acoustic and optical branches. For higher wave-vectors we analyze the dynamic structure factor in terms of corrections to the so-called *impulse approximation*,[62] finding a coherent response which is peculiar of both superfluid and solid helium.

In Sec. 3.1 we give an introductory account of the phonon theory of long wave-length excitations in solids. In Sec. 3.2 the reader is provided with an outline of the numerical methods we have adopted to best accomplish the study of density excitations. In Sec. 3.3 we report on the analysis of our quantum Monte Carlo results both in the phonon regime and in the intermediate momentum region. Sec. 3.4 is finally devoted to a few concluding remarks on this specific application of the quantum Monte Carlo methodology for excited-state properties.

3.1 Lattice Dynamics

3.1.1 Long Wave-Lengths

The long wave-length lattice dynamics of a solid is fully characterized by its dynamic structure factor, which is the space-time Fourier transform of the density-density correlation function. In real time and reciprocal space, the autocorrelation function of the density operator reads:

$$S(\mathbf{Q},t) = \frac{1}{N}\left\langle \sum_{kl} e^{-i\mathbf{Q}\cdot\mathbf{r}_k(t)} e^{i\mathbf{Q}\cdot\mathbf{r}_l(0)} \right\rangle , \tag{3.1.1}$$

where the brackets indicate equilibrium (ground-state or thermal) expectation values. In a weakly anharmonic system, it is convenient to expand $S(\mathbf{Q},t)$ into a sum of terms involving one-phonon processes, two-phonon scattering, interference processes and so on:[61]

$$S(\mathbf{Q},t) = S_1(\mathbf{Q},t) + S_2(\mathbf{Q},t) + S_{1,2}(\mathbf{Q},t) + \cdots . \tag{3.1.2}$$

The physical meaning of such an expansion is best appreciated by introducing the atomic displacements from the equilibrium lattice sites, $\{\mathbf{R}_l\}$: $\mathbf{u}_l(t) = \mathbf{r}_l(t) - \mathbf{R}_l$. In terms of the **u**'s and the **R**'s, the one-phonon contribution to the dynamic structure factor of a simple Bravais lattice reads:[61]

$$S_1(\mathbf{Q},t) = e^{-2W} \sum_l e^{-i\mathbf{Q}\cdot(\mathbf{R}_l - \mathbf{R}_0)} \times \langle \mathbf{Q}\cdot\mathbf{u}_l(t)\mathbf{Q}\cdot\mathbf{u}_0(0)\rangle , \tag{3.1.3}$$

where e^{-2W} is the Debye-Waller factor. For a harmonic crystal—to which only, strictly speaking, the phonon language applies—we consider the vibrational frequency $\omega_j(\mathbf{q})$ and polarization vector $\boldsymbol{\epsilon}(\mathbf{q}|j)$ of the j-th phonon branch at wave vector $\mathbf{q}$ in the first Brillouin zone. In terms of these quantities, the one-phonon contribution reads:[25]

$$S_{1H}(\mathbf{Q},t) = \sum_j g^2(\mathbf{Q}|j) e^{-i\omega_j(\mathbf{q})t}, \tag{3.1.4}$$

where $\mathbf{Q} = \mathbf{q}+\mathbf{G}$, $\mathbf{G}$ being a reciprocal-lattice vector, and $g^2(\mathbf{Q}|j) \propto |\mathbf{Q}\cdot\boldsymbol{\epsilon}(\mathbf{Q}|j)|^2$ is the so-called inelastic structure factor that filters out transverse vibrations. In the case of a non-primitive lattice, such as the *hcp* phase of Helium, the form of the inelastic structure factor is slightly more complicated:[25]

$$g^2(\mathbf{Q}|j) = e^{-2W}\frac{\hbar}{2m\omega_j(\mathbf{q})}\left|\sum_k \mathbf{Q}\cdot\boldsymbol{\epsilon}_k(\mathbf{q}|j)e^{i\mathbf{Q}\cdot\mathbf{d}_k}\right|^2, \tag{3.1.5}$$

where the $\mathbf{d}$'s are the positions of the atomic basis.

In a perfectly harmonic solid the Fourier transform of Eq. (3.1.4), $S_{1H}(\mathbf{Q},\omega)$ is merely a sum of Dirac delta functions centered at the phonon frequencies. In a real solid, things are more complicated: anharmonic interactions broaden the one-phonon peaks and give rise to non-vanishing multi-phonon and interference contributions to the dynamic structure factor (Eq. 3.1.4). When anharmonic effects are not too large, one-phonon excitations can still be long-lived—thus providing a reasonable description of the dynamics—and it is thus well justified to identify the positions of the finite-width peaks of $S_1(\mathbf{Q},\omega)$ with phonon frequencies. From an experimental point of view, phonon frequencies are generally extracted from the peaks of the full dynamic structure factor $S(\mathbf{Q},\omega)$. The cross section of inelastic neutron or X-ray scattering is in fact proportional to $S(\mathbf{Q},\omega)$ [144] and no direct access is possible to its one-phonon component. The latter dominates the cross section only at small transferred momentum, whereas multi-phonon contributions cannot in general be neglected when pursuing a comparison between calculated and measured phonon dispersions.

3.1.2 Shorter Wave-Lengths

The very concept of *phonon*, which lies at the basis of the theory of lattice dynamics sketched above, is most appropriate to describe the low-lying portion of the spectrum of solid ^{4}He, probed by inelastic neutron or X-ray scattering at long wave-lengths. In the opposite limit of short wave-lengths, the scattering process can be pictured as the creation of particle-hole (atom-vacancy) pairs, resulting from the high momentum transferred to the crystal from the incoming particle beam. [61] The atomic kinematics at high energies is affected by the single-particle momentum distribution, $n(\mathbf{Q})$, and neutron spectroscopy at large momentum transfer has in fact proven useful to probe off-diagonal long-range order, both in superfluid [124] and, more recently, in solid Helium. [46]

At intermediate wave-lengths both the phonon and a purely impulsive, particle-hole, picture of density excitations break down. In spite of the attention paid by both experimentalists and theorists to this peculiar intermediate regime, both in the superfluid [85, 137] and in the solid[60, 45] phases, it turns out that the neglect of interaction-induced coherence effects make previous theoretical studies not totally satisfactory. [60]

At small wave-length, the solid behaves like a collection of almost non-interacting atoms and the intermediate scattering function can be approximated by its incoherent part, [62] i.e.

$$S_{\text{inc}}(\mathbf{Q},t) = \frac{1}{N}\left\langle \sum_{l} e^{-i\mathbf{Q}\cdot\mathbf{r}_l(t)} e^{i\mathbf{Q}\cdot r_l(0)} \right\rangle, \tag{3.1.6}$$

which amounts to neglecting the interference terms involving different atoms. For a crystal, the incoherent part can be expressed in terms of the recoil frequency $\omega_R = \frac{\hbar}{2m}Q^2$ and of the phonon density of states $g(\omega)$, leading to

$$S_{\text{inc}}(\mathbf{Q},t) = \exp\left[\omega_R \int_0^\infty d\omega g(\omega)\frac{1}{\omega}(e^{-i\omega t}-1)\right]. \tag{3.1.7}$$

Such an expression has been used by Glyde [60] to compute the incoherent response of *bcc* ^{4}He. By its very nature, the incoherent approximation is only reliable at very high wave-vector,[60] roughly larger than $20\,\text{Å}^{-1}$. In order to account for the leading coherence effects on the short wave-length dynamics of an extended system, it is convenient to consider a cumulant expansion of the intermediate scattering function,[62]

$$S(\mathbf{Q},t) = S(\mathbf{Q})e^{-i\omega_R t}\exp\left[\sum_{n=1}^{\infty}\frac{\mu_n}{n!}(-it)^n\right], \tag{3.1.8}$$

where $S(\mathbf{Q})$ is the static structure factor and μ_n are the cumulants of the distribution $S(\mathbf{Q},\omega-\omega_R)$. Retaining the leading contribution to such an expansion yields the so-called *Impulse Approximation*, according to which the Fourier transform of the dynamic structure factor consists of a main Gaussian component centered at the recoil frequency ω_R, plus additive corrections: [6]

$$S(\mathbf{Q},\omega) = \tilde{S}_{IA}(\mathbf{Q},\omega) + \tilde{S}_1(\mathbf{Q},\omega) + +\tilde{S}_2(\mathbf{Q},\omega) + \tilde{S}_3(\mathbf{Q},\omega) + \cdots, \tag{3.1.9}$$

where the first terms of the expansion read

$$\tilde{S}_{IA}(\mathbf{Q},\omega) = \frac{S(\mathbf{Q})}{\sqrt{2\pi\mu_2}} e^{-\frac{\omega_d^2}{2}} \tag{3.1.10}$$

$$\tilde{S}_1(\mathbf{Q},\omega) = -\frac{\mu_3}{2\mu_2^2}\left(\omega-\omega'_R\right)\left[1-\frac{\omega_d^2}{3}\right]\tilde{S}_{IA}(\mathbf{Q},\omega) \tag{3.1.11}$$

$$\tilde{S}_2(\mathbf{Q},\omega) = \frac{\mu_4}{8\mu_2^2}\left[1-2\omega_d^2+\frac{\omega_d^4}{3}\right]\tilde{S}_{IA}(\mathbf{Q},\omega) \tag{3.1.12}$$

$$\tilde{S}_3(\mathbf{Q},\omega) = \frac{\mu_5}{8\mu_2^3}\left(\omega-\omega'_R\right)\left[1-\frac{2}{3}\omega_d^2+\frac{\omega_d^4}{15}\right]\tilde{S}_{IA}(\mathbf{Q},\omega) \tag{3.1.13}$$

with $\omega'_R = \omega_R/S(\mathbf{Q})$ and $\omega_d^2 = \left(\omega-\omega'_R\right)^2/\mu_2$.

3.2 Numerical Methods

The path integral quantum Monte Carlo methodology allows for the exact simulation of the imaginary-time dynamics of continuous bosonic systems at both finite [22] and zero [8] temperature. Specializing to the zero temperature case, a discretized path integral expression for the imaginary-time propagator can be used to project out the exact ground state Ψ_0 from a positive trial wave function Φ_0, according to by now familiar expression $\Psi_0 = \lim_{\tau\to\infty}\exp(-\tau\mathcal{H})\Phi_0$, thus mapping the imaginary-time evolution, from which ground-state expectation values can be obtained, onto a classical system whose fundamental variables are open quantum paths (or *reptiles* in the parlance of Refs. [8, 30] and [7]). The details of the formalism and its numerical realization for continuous systems are conceptually similar to the ones introduced in the previous Chapter. However, at variance with the imaginary-time diffusion of particles on a lattice, an exact expression for the small time propagators is recovered in this case only in the limit of small time step ϵ. A systematic error due to the small-time Trotter decomposition of the propagator has therefore to be carefully taken into account. Nonetheless, as also explained in detail in Ref. [7], unbiased ground-state expectation values are obtained when the projection time τ is large enough and the step ϵ of the time discretization is small enough. Conditions that are practically very well verified in most numerical simulations.

Our strategy is to simulate realistic models of ^{4}He atoms interacting through the Aziz [5] pair potential, placed in a cuboid cell accommodating an *hcp* lattice. The number N of particles is either 180 or 360, the latter corresponding to a cell with double extension in the ΓA direction. Although all the reported results refer to the larger system, we have found a full agreement between the relevant observables computed on the common set of wave vectors shared by the smaller and the larger simulation cells. For systems of this size, we find it more efficient to use the bisection algorithm [36, 118] rather than the reptation algorithm [8] for sampling the path space. We adopt the so-called *primitive approximation* for the imaginary-time propagator,[36] which requires a small time step $\epsilon = 10^{-3}$ inverse K for accurate results, and we set the projection time to $\tau = 0.3\,K^{-1}$.

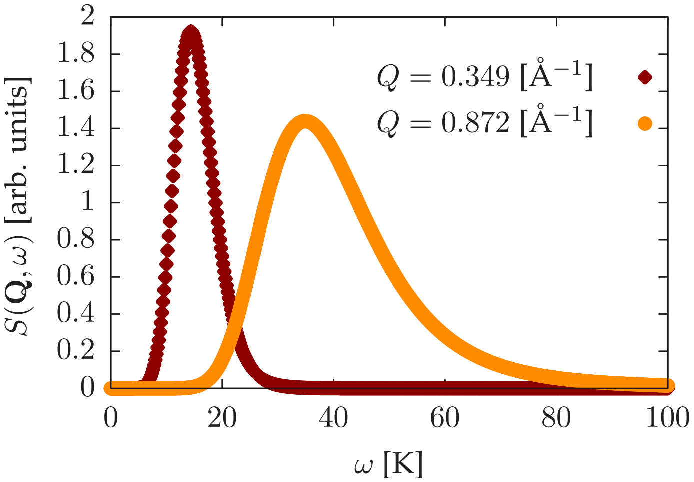

Fig. 3.2.1 Example of two reconstructed spectra at different wave-vectors along the ΓA direction at the melting density ρ_1.

The trial function which serves as a starting state for the imaginary-time projection is of the standard McMillan-Nosanow form,

$$\Phi_0(R) = \exp\left[-\sum_{k<l} a r_{kl}^{-b} - \sum_{l} c(\mathbf{r}_l - \mathbf{s}_l)^2\right] \tag{3.2.1}$$

where $\{\mathbf{r}_1, \ldots, \mathbf{r}_N\} \equiv R$ are the coordinates of the N atoms, and s_l is the l-th site of the *hcp* lattice. The three parameters a, b, and c are optimized by minimizing the variational energy and their numerical values for the densities considered hereby are shown in Table 3.1. The Gaussian localization terms in the trial function explicitly break Bose symmetry at the variational level. Even though the imaginary-time projection fully restores the Bose symmetry, the required projection time is extensive in the number of particles and particularly long in all the gapless density sectors of the spectrum we are interested in. Nonetheless, we believe that the lack of permutation symmetry cannot affect the determination of the density excitation energies due to the small frequency of particle exchanges in the crystal. This point can be further elucidated noticing that the presence of a vacancy in the simulation box greatly enhances the number of exchanges.[40] Therefore, if indistinguishability were important, one would expect a change in the frequency upon doping with vacancies. However, no such effect was found in in a variational calculation[56] where Bose symmetry was taken into account.

$\rho\ \left[\mathring{A}^{-3}\right]$	$a\ \left[\mathring{A}^{b}\right]$	b	$c\ \left[\mathring{A}^{-2}\right]$
0.028	156.0	5.74	0.565
0.037	139.4	5.75	0.993

Table 3.1 Optimal values of the variational parameters appearing in the McMillan-Nosanow wave-function.

In order to obtain $S(\mathbf{Q},\omega)$ from imaginary-time correlations, an inverse Laplace transform must be performed, for which we use the *maximum entropy* method described in 1.3.4. Although the reconstructed spectra are typically much too broad, this procedure gives good results, at least for the position of the peaks, when a single sharp feature exhausts most of the spectral weight. As a typical example, we show in Figure 3.2.1 two spectra at different wave-vectors for the longitudinal acoustic branch, calculated at the melting density $\rho_1 = 0.028\,[\mathring{A}^{-3}]$. Despite the fact that much of the width of the peaks is an artifact of the numerical inversion of the Laplace transform, it is nonetheless plausible that the broadening of the spectra shown in Figure 3.2.1 reflects stronger multiphonon effects at higher wave-vectors. In the following we refer to the position of the peaks of the reconstructed spectrum as to *phonon energies*. The reported error bar is the statistical uncertainty of the peak position, as estimated with the jackknife resampling method.[63]

3.3 Results

In this Section we present the results of our quantum Monte Carlo simulations for both the phonon dispersion energies and the higher wave-vectors response of the solid along high symmetry directions. A representation of the first Brillouin zone of the *hcp* crystal and its high symmetry points is shown in Figure 3.3.1.

3.3.1 Long Wave-length Excitations

Longitudinal Modes

The excitation energies of longitudinal vibrations can be straightforwardly obtained from the dynamic structure factor $S(\mathbf{Q},\omega)$, when available. In a lattice with a basis, such as *hcp* ^{4}He, multiple modes (acoustic and optic) exist at each point of the first Brillouin zone. Although for a generic wave-vector all the branches contribute to $S(\mathbf{Q},\omega)$, it often happens that—because of the explicit dependence of the inelastic structure factor 3.1.5 on both the wave-vector and the

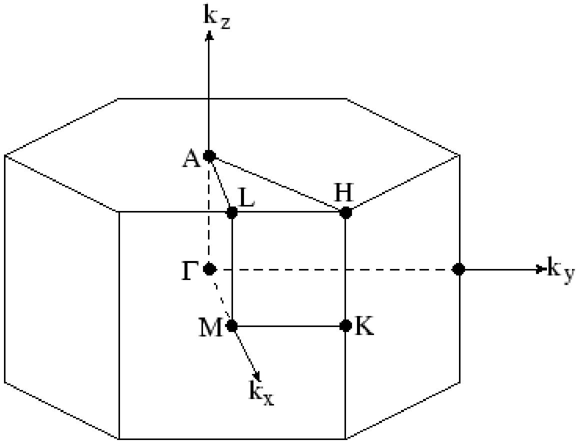

Fig. 3.3.1 First Brillouin zone of the hcp crystal. The high symmetry directions investigated in this Chapter are ΓA and ΓM.

branch index—along high-symmetry directions different branches dominate (and in practice are only visible) at different values of the wave-vector. As a consequence, there are regions of the reciprocal space in which the acoustic modes dominate while the optical modes are suppressed and vice-versa. To figure out the relative weights of the branches, the inelastic structure factor can be calculated in a number of (approximate) ways, as in Ref. [122] for beryllium, another *hcp* solid. By virtue of the strongly geometrical nature of $g^2(\mathbf{Q}|j)$, it is sufficient to look at one of these approximate calculations performed for the *hcp* geometry to realize that, with few exceptions, the relative weights do generally suppress one mode and privilege the other. Our results substantially confirm this picture, the calculated spectral functions being generally dominated by a single peak. Reconstructing a complete picture of the phonon dispersions thus require sampling the dynamic structure factor outside the first Brillouin zone.

We have calculated the phonon energies at the melting density $\rho_1 = 0.028\,[\text{Å}^{-3}]$—in a regime of strong quantum fluctuations signaled by a considerable Lindemann's ratio—and at the density $\rho_2 = 0.037\,[\text{Å}^{-3}]$, where the quantum fluctuations are less pronounced. Results are shown in Figures 3.3.2 and 3.3.3 using an extended-zone scheme reminiscent of the way the optic and acoustic modes are measured in the lab. The phonon energies extracted by $S(\mathbf{Q},\omega)$ are compared to experimental data. The phonon energies resulting from an analysis of the one-phonon contribution to the dynamic structure factor are also shown for comparison.

The main findings that emerge from the calculations of the longitudinal modes are the following:

1. The overall agreement between the calculated and measured peak energies is good. The estimated errors come from the intrinsic width of the peaks of the dynamic structure factor, which is larger for optic than for acoustic phonon. This feature is present in both the

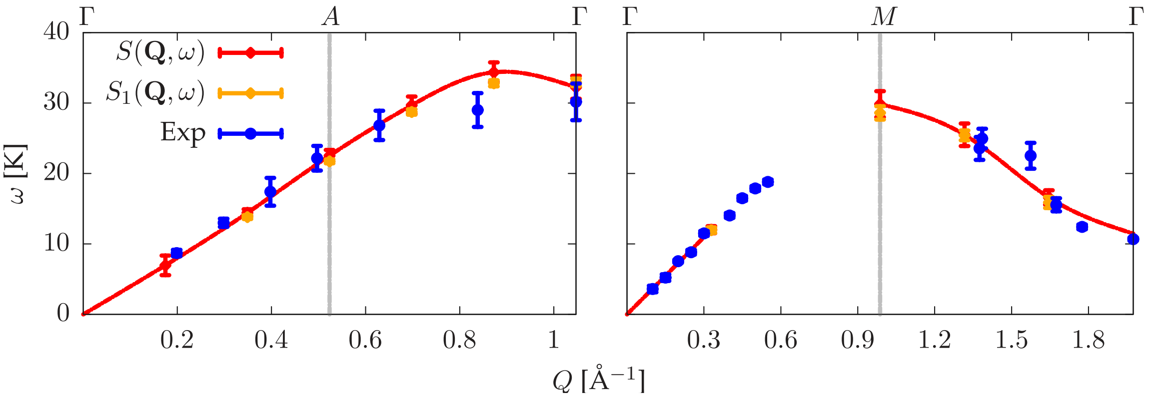

Fig. 3.3.2 Longitudinal phonon energies at the melting density ρ_1 extracted from $S(\mathbf{Q},\omega)$ and $S_1(\mathbf{Q},\omega)$, ΓA and ΓM directions (resp. left and right panel). The limit of the first Brillouin zone is indicated by a vertical gray line. Experimental data from [90] and [91]. Frequencies calculated at discrete wave-vectors are interpolated by cubic splines as a guide to the eye.

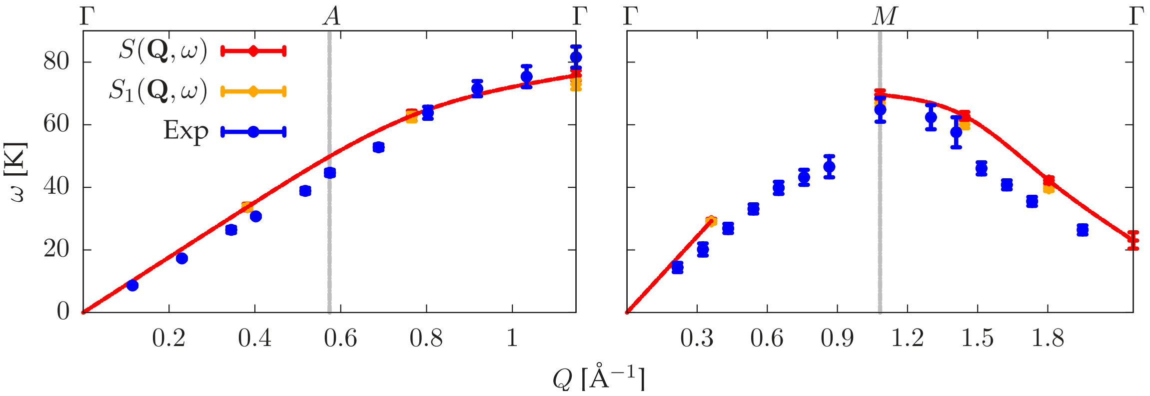

Fig. 3.3.3 Longitudinal phonon energies at the density $\rho_2 = 0.037\,[\text{Å}^{-3}]$ extracted from $S(\mathbf{Q},\omega)$ and $S_1(\mathbf{Q},\omega)$, ΓA and ΓM directions (resp. left and right panel). The limit of the first Brillouin zone is indicated by a vertical gray line. Experimental data from Ref. [108]. Frequencies calculated at discrete wave-vectors are interpolated by cubic splines as a guide to the eye.

theoretical and experimental spectra, although in the former the width is enhanced by the numerical difficulties in performing inverse Laplace transforms.

2. The discrepancy between the frequencies estimated in the one-phonon approximation and from the full dynamic structure factor is generally small. Multiphonon processes have clearly the effect of broadening the spectrum—particularly for large wave vectors—but they hardly affect peaks' positions.
3. In the ΓM direction at the melting density ρ_1, we obtain a substantial improvement over SCP results.[59] We are thus able to separate the optic from the acoustic branches, which appear as distinct peaks in the dynamic structure factor. We also obtain a significant improvement over previous variational quantum Monte Carlo results;[56] besides, in Ref. [56] optical branches are calculated only in the ΓA direction.

4. For the higher density ρ_2 we observe a stronger discrepancy between theoretical and experimental data, particularly in the ΓM direction, possibly due to the pair potential adopted here.[92]

Transverse Modes

The direct evaluation of transverse phonon modes from the dynamic structure factor is hindered by the $\mathbf{Q} \cdot \epsilon(\mathbf{q}|j)$ term appearing in its expression (Eqs. 3.1.4 and 3.1.5) that selects longitudinal modes. At least two strategies can be deployed to circumvent this problem. The most immediate solution consists in considering the peaks in the Fourier transform of the transverse counterpart of the one-phonon contribution to the dynamic structure factor:[131]

$$S_{1\perp}(\mathbf{Q},t) \propto \left\langle \sum_{l,m} u_{\perp,l}(t) u_{\perp,m}(0) e^{i\mathbf{Q}\cdot(\mathbf{R}_l - \mathbf{R}_m)} \right\rangle , \tag{3.3.1}$$

where $u_{\perp,}$ is the transverse component of the atomic displacement from equilibrium. Although legitimate in principle, this approach is limited to the weak anharmonic regime and only gives access to the positions of the peaks, not to their intensities. A better approach, which in principle also gives access to peaks intensities, is to mimic closely the experimental practice and calculate the dynamic structure factor at wave-vectors $\mathbf{Q} = \mathbf{G} + \mathbf{q}$ such that $\mathbf{q}$ is arbitrarily *quasi-perpendicular* to $\mathbf{Q}$, so that a lattice vibration polarized parallel to $\mathbf{Q}$ is actually quasi-transverse:[86] this is always possible, just choosing a large enough $\mathbf{G}$, *i.e.* looking at wave-vectors in the second, third, or successive Brillouin zones. In such a geometry transverse phonon energies at high-symmetry wave-vectors in the first Brillouin zone can be estimated from the position of the peaks in the dynamic structure factor. In order to achieve a close comparison between our results and experimental data, our simulations at the melting density have been performed along the same *quasi-transverse* wave-vector directions as used in Ref. [90]. The transverse phonon energies thus obtained are presented in Figures 3.3.4 and 3.3.5, in an extended zone scheme.

The main findings that emerge from the calculations of the transverse modes closely parallel the results obtained in the longitudinal case:

1. The overall agreement with the experimental data is good.
2. The discrepancy between the energy obtained from the full dynamic form factor and from its one-phonon component is small. Energies from the full form factor tend to be more noisy than in the longitudinal case, possibly due to larger multi-phonon effects related to the large wave-vector involved in the quasi-transverse geometry.
3. We find a substantial improvement over the SCP results, particularly in the ΓM direction, whilst there are no other quantum Monte Carlo results to compare with.

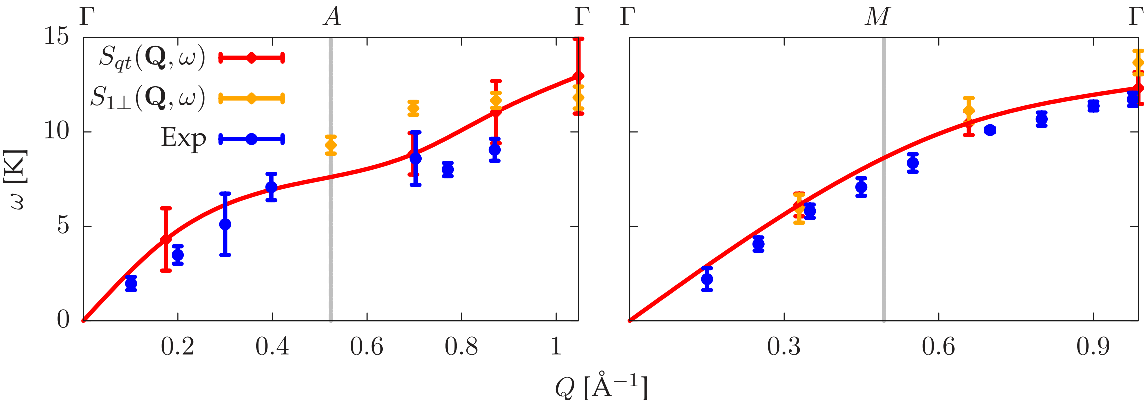

Fig. 3.3.4 Transverse phonon energies at the melting density ρ_1 extracted from the *quasi-transverse* geometry of $S(\mathbf{Q},\omega)$ and from the transverse components of $S_1(\mathbf{Q},\omega)$, ΓA direction and $T_{\|}$ branch of the ΓM direction (resp. left and right panel). The limit of the first Brillouin zone is indicated by a vertical gray line. Experimental data from [90] and [91]. Frequencies calculated at discrete wave-vectors are interpolated by cubic splines as a guide to the eye.

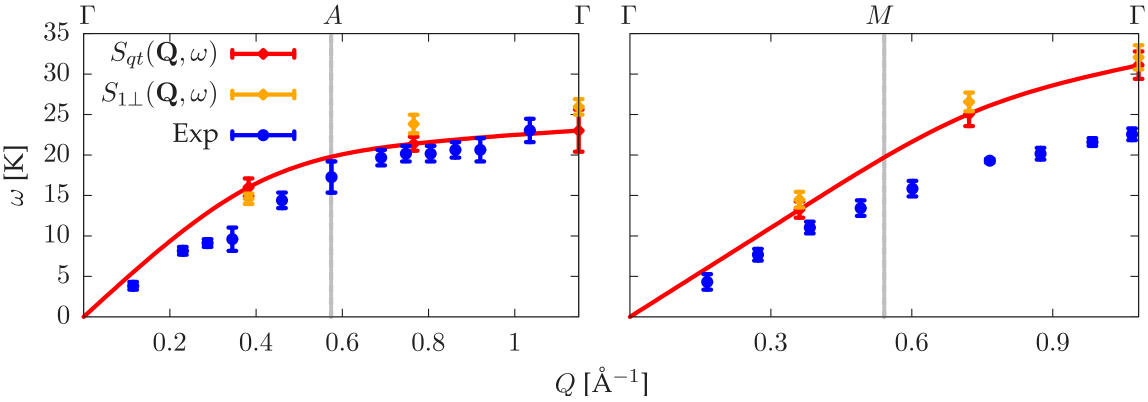

Fig. 3.3.5 Transverse phonon energies at the density $\rho_2 = 0.037\,[\text{Å}^{-3}]$ extracted from the *quasi-transverse* geometry of $S(\mathbf{Q},\omega)$ and from the transverse components of $S_1(\mathbf{Q},\omega)$, ΓA direction and $T_{\|}$ branch of the ΓM direction (resp. left and right panel). The limit of the first Brillouin zone is indicated by a vertical gray line. Experimental data from [108]. Frequencies calculated at discrete wave-vectors are interpolated by cubic splines as a guide to the eye.

4. We find a systematic degradation of the agreement with experimental results for increasing density, especially for the direction ΓM of Figure 3.3.5.

3.3.2 Intermediate Wave-length Excitations

Recent claims that solid ^{4}He may display a *supersolid* behavior closely related to superfluidity in the liquid phase have prompted a revived interest in the experimental investigation of density excitations at intermediate wave-lengths, from which valuable information on the atomic momentum distribution can be extracted.[46] These experimental efforts rely on the accurate determination of corrections to the Impulse Approximation (Eq. 3.1.9), a task which is facilitated in the large-momentum regime.[62]

Apart from the issues of off-diagonal long-range order and Bose-Einstein condensation in solid ^{4}He, the role of atomic interference—as emerging from the additive corrections to the bare Impulse Approximation—has not yet been the subject of detailed theoretical investigations. To our knowledge, the best quantitative account of the response of solid helium is limited to regions of small and very large wave-vectors.[60] Nonetheless in the *intermediate* region where the long-wavelength spectra of both the liquid and the solid merge into the large-momentum regime of nearly free-particle recoil, no *ab initio* results have been reported so far. Our quantum Monte Carlo methodology, instead, allows us to provide an accurate description of this regime as well, showing evidence of a phonon-like residual coherence, not dissimilar from what is found in the superfluid phase.[85] We have concentrated our attention on wave-vectors roughly ranging from $5\,\text{Å}^{-1}$ to $10\,\text{Å}^{-1}$, between the phonon and the purely *single particle* regimes. The transition between these two regions can be clearly seen looking at the dispersion of the peaks of the dynamic structure factor, as a function of the excitation wave-vector.

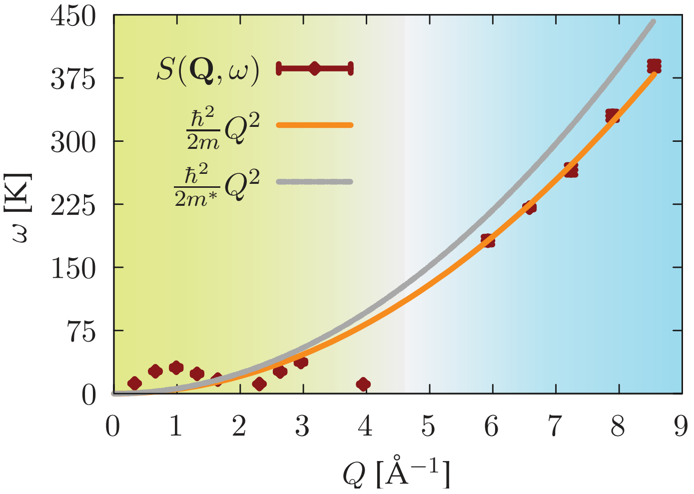

Fig. 3.3.6 Longitudinal excitations along the ΓM direction at the density ρ_1. The solid line is the fitted free-particle dispersion of a quasi-particle with effective mass $m*$, while the gray line is the free-particle dispersion of atomic Helium. The two different background colors ideally separate the phonon region from the intermediate region of wave-vectors.

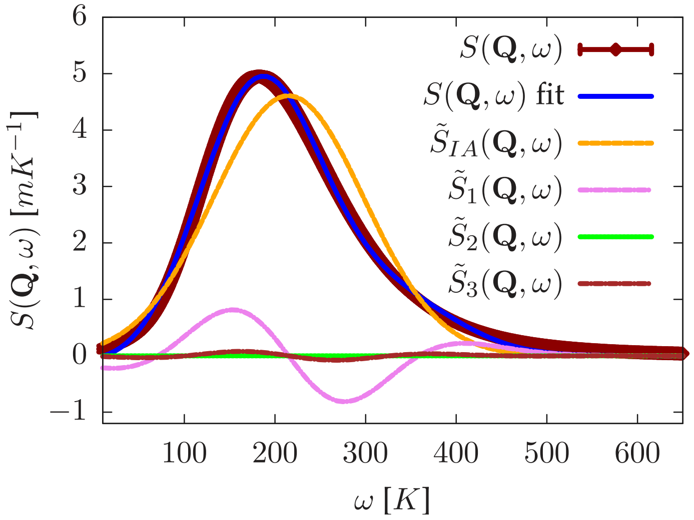

Fig. 3.3.7 Analysis of the dynamic structure factor into the Impulse Approximation and its additive corrections at the wave-vector $Q = 5.92\,\text{Å}^{-1}$ along the ΓM direction.

In Figure 3.3.6 the longitudinal excitation energies of the crystal at the melting density ρ_1 are shown. In the phonon-like regime (on the left of the figure with a yellowish background) we observe a periodic dispersion with soft modes corresponding to reciprocal-lattice vectors; for larger wave-vectors (on the right with a bluish background) we observe a free-particle parabolic dispersion, corresponding to an effective mass which is slightly larger than the bare Helium mass, with $M^\star \simeq 1.27\,M$.

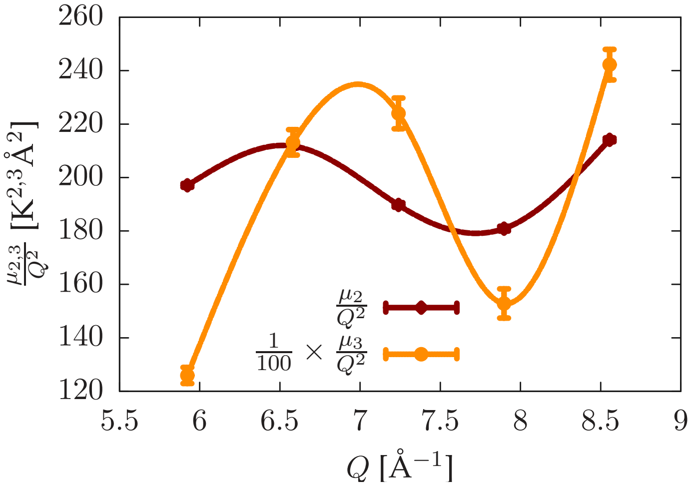

Fig. 3.3.8 Coherent oscillations of the cumulants μ_2 and μ_3 appearing in the additive corrections to the Impulse Approximation. Cumulants calculated at discrete wave-vectors are interpolated by cubic splines as a guide to the eye.

In order to characterize the density excitations of $^4\mathrm{He}$ in this region of momenta, we have analyzed the dynamic structure factor in terms of a cumulant expansion, Eq. (3.1.9), thus extending the scope of previous theoretical results, [60] which were essentially unable to predict the response of the solid in this intermediate regime. In Figure 3.3.7 the calculated dynamic structure factor at the melting density ρ_1 is shown along with its decomposition in terms of the leading Impulse Approximation and its additive corrections of Eqs. (3.1.10-3.1.13). The coefficients μ_n are taken as free parameters in the fitting procedure of the dynamic structure factor, much as it is done in the analysis of the experimental data.[62]

The bare Impulse Approximation of the dynamic structure factor overlooks quantum coherence effects in the density response functions, which are experimentally observed [85, 137] in superfluid $^4\mathrm{He}$. A better account of quantum coherence can be achieved including higher-order corrections in the cumulant expansion of Eq. (3.1.9) whose non-vanishing contribution is in fact recognized in the fitting of our reconstructed spectra, Figure 3.3.7. The presence of quantum coherence between Helium atoms in the solid is further appreciated upon looking for deviations from the incoherent approximation of Eq. (3.1.6). A cumulant expansion of the incoherent dynamic structure factor can be carried out, and it is known [61] that the cumulants μ_2^{inc} and μ_3^{inc} of such an expansion increase monotonically as Q^2 whereas μ_4^{inc} and μ_5^{inc} increase as Q^4. Characteristic Q-dependent oscillations in the ratios $\mu_{2,3}/Q^2$ and $\mu_{4,5}/Q^4$ can be therefore exploited to infer deviations from the purely incoherent response. Such oscillations have been observed in the superfluid phase [85] and theoretically justified within a T-matrix approximation of the He-He atom scattering. [137] A similar behavior has also been recently observed in solid $^4\mathrm{He}$, [45] although no satisfactory *ab-initio* theoretical description exists yet. The cumulant dissection of the spectral properties extracted from our quantum Monte Carlo simulations is a natural tool to examine the relics of quantum coherence in the intermediate wave-vector region, which closely parallels the experimental analysis. In Figure 3.3.8 we show the Q-dependent oscillations in the ratios μ_2/Q^2 and μ_3/Q^2 as found in our analysis of the dynamic structure factor, which are a quite clear manifestation of the residual coherence in the dynamics of solid helium in this intermediate region. The quantitative aspects of this analysis may be influenced by the quality of the Maximum Entropy reconstruction of the spectrum. However, the shift of the peak position with respect to the free particle recoil frequency should be reliable information, as suggested by the good agreement of the calculated and measured phonon dispersions previously shown.

3.4 Concluding Remarks

In this Chapter we have shown a completely *ab-initio* and unbasied study of the lattice dynamics of crystalline ^{4}He at zero temperature. Although the stochastic nature of quantum Monte Carlo methods limits us to explore the quantum imaginary-time dynamics, we have shown that quantitative accuracy can be nonetheless achieved. One of the most appealing features of our analysis is the possibility to directly parallel the experimental investigation based on neutron scattering. The study of the full dynamic structure factor has allowed us to describe both the phonon and the intermediate wave-length regions of excitations.

At lower density, where the quantum fluctuations substantially affect the dynamics, we have obtained satisfactory results for the phonon energies, whereas approximate quasi-harmonic theories have shown difficulties in the accurate determination of the vibrational dispersions. An interesting point deserving more research is the effect of the adopted pair-potential on the calculated phonon branches. Our study suggests a degradation of the agreement to experimental data at higher density which could probably be alleviated upon the inclusion of higher than two body terms in the interatomic potential.

In the intermediate regime of wave-vectors, where the density excitations are better understood in terms of corrections to the small wave-length behaviour, we have shown that residual coherence in the quasi-particle excitations is present as in superfluid helium. Altough much of the theoretical and experimental efforts on the merging between the phonon and the single particle regimes have concentrated on the archetypal quantum solid –^{4}He– we believe that an extension of such an analysis to other quantum solids such as ^{3}He or molecular hydrogens H_2 would surely be worthwhile.

Chapter 4

Exact Fermionic Properties From Spectral Functions

The Itinerant Ferromagnetic Phase of the Hubbard Model

The quantum Monte Carlo simulation of systems of interacting fermions is beset by the antisymmetry of the ground-state wave function which, at variance with bosons, prevents it from being treated as the stationary distribution of a classical stochastic process. The main attempt to cope with the ensuing difficulties is the *fixed-node* approximation, which we have introduced in 2.2.4. If complemented by an accurate variational ansatz for the wave function, the fixed-node approach provides a method to study the properties of large fermionic systems allowing for reliable extrapolations to the thermodynamic limit. Unfortunately, the nature of the approximation does not allow for an estimate of the residual error, which not rarely can lead to biased results. However, there exists an interesting class of non-trivial strongly correlated Hamiltonians whose eigenstates of fermionic symmetry are sufficiently close in energy to the bosonic ground state, to allow them to be treated on an equal footing; for this class of Hamiltonians we have proposed and demonstrated [34] a strategy to overcome the sign problem via the dissection of the excitation spectrum of the corresponding bosonic auxiliary problem, providing an essentially *unbiased* scheme for medium-size fermionic systems.

In the following we describe the above-mentioned methodology that exploits a suitable bosonic imaginary-time dynamics to provide exact information on the ground-state properties of the fermionic system of interest. By means of this novel scheme, we show that important advances in the understanding of an elusive model for itinerant ferromagnetism can be achieved. In particular, we obtain particularly accurate results for the ground-state properties of the fermionic Hubbard model in the large interacting limit. Our findings indicate that at high electron density a fully ferromagnetic (Nagaoka) state is stable not only with respect to the paramagnetic phase, but also with respect to other previously proposed partially polarized states. [12] A non-trivial transition to a paramagnetic phase is observed upon decreasing the electron density. Near the transition this phase is characterized by highly degenerate states with different values of the total spin, thus indicating a divergence of the magnetic susceptibility, consistent with an infinite-order phase transition. [15]

In Sec. 4.1 we present our novel approach to exact fermionic properties; in Sec. 4.2 the infinite-U Hubbard model and its relevance to itinerant ferromagnetism is explained, whereas in Sec. 4.3 the main findings of our analysis are presented. In 4.4 the effect of a realistic interaction for trapped cold atoms is shown and some concluding remarks on both the novel quantum Monte Carlo methodology introduced and the itinerant ferromagnetism and are finally drawn in 4.5.

4.1 Fermionic-Correlations Method

The spectrum of a Hamiltonian of identical particles, $\mathcal{H}$, can be classified according to the irreducible representations of the symmetric (permutation) group. The Pauli principle asserts that only totally antisymmetric states are physically allowed for fermions, but mathematical states of any symmetry can also be considered. In particular, the (unphysical) state of lowest energy is in general totally symmetric, so that the fermionic ground state can be formally considered as an excited state of a bosonic system. As such, it can be studied via excited-state techniques, provided the Bose-Fermi gap is not too large with respect to the physical gap in the fermionic sector of the spectrum. Let $|\Psi_0^{\mathrm{b}}\rangle$ be the bosonic ground state of the system and $\mathcal{A}$ an arbitrary observable. In Chapter 2 we have shown that a recent extension of the reptation quantum Monte Carlo method [8] to lattice models [30] allows for an efficient and unbiased evaluation of imaginary-time $\tau = it$ correlation functions, $\mathcal{C}_{\mathcal{A}}(\tau) = \langle\Psi_0^{\mathrm{b}}|\mathcal{A}^\dagger(\tau)\mathcal{A}|\Psi_0^{\mathrm{b}}\rangle/\langle\Psi_0^{\mathrm{b}}|\Psi_0^{\mathrm{b}}\rangle$, where $\mathcal{A}(\tau) = \mathrm{e}^{\mathcal{H}\tau}\mathcal{A}\mathrm{e}^{-\mathcal{H}\tau}$ is the Heisenberg representation of $\mathcal{A}$.

The connection of such correlation functions with the excited states $|\Psi_k\rangle$ of $\mathcal{H}$ is obtained by considering the Lehman spectral representation,

$$\mathcal{C}_{\mathcal{A}}(\tau) = \frac{\sum_k |\langle\Psi_0^{\mathrm{b}}|\mathcal{A}|\Psi_k\rangle|^2 e^{-\Delta_k\tau}}{\langle\Psi_0^{\mathrm{b}}|\Psi_0^{\mathrm{b}}\rangle}, \tag{4.1.1}$$

where $\Delta_k = E_k - E_0^{\mathrm{b}}$ are excitation energies with respect to the bosonic ground state. Selection rules act in such a way as to exclude from Eq. (4.1.1) those excited states whose symmetry is different from that of the state $\mathcal{A}|\Psi_0^{\mathrm{b}}\rangle$. In particular, if $\mathcal{A}$ is chosen to be totally antisymmetric with respect to permutations, only fermionic (ground and excited) states would contribute to $\mathcal{C}_{\mathcal{A}}(\tau)$. For example, if $\mathcal{A}$ is the local operator whose coordinate representation is the ratio between the fermionic and bosonic ground-state wave functions ($\mathcal{A}_f(n) = \langle n|\Psi_0^{\mathrm{f}}\rangle/\langle n|\Psi_0^{\mathrm{b}}\rangle$, where $|n\rangle$ denotes the many-body lattice configuration), the correlation function $\mathcal{C}_{\mathcal{A}}(\tau)$ would be proportional to the single exponential $\mathrm{e}^{-\Delta_0\tau}$.

In practice, neither the bosonic nor the fermionic ground state are known exactly and only variational approximations to them are available, which we denote here by $|\Phi_0^{\mathrm{b}}\rangle$ and $|\Phi_0^{\mathrm{f}}\rangle$, respectively. Correspondingly, the antisymmetric observable is defined as $\mathcal{A}_f(n) = \langle n|\Phi_0^{\mathrm{f}}\rangle/\langle n|\Phi_0^{\mathrm{b}}\rangle$. In this way, the leading coefficient of the expansion is given by $\langle\Psi_0^{\mathrm{b}}|\mathcal{A}_f|\Psi_0^{\mathrm{f}}\rangle \simeq \langle\Phi_0^{\mathrm{f}}|\Psi_0^{\mathrm{f}}\rangle$ and can be systematically maximized by improving the quality of the variational states. The energy of the fermionic ground state can be then extracted either directly by noticing that $E_0^{\mathrm{f}} = E_0^{\mathrm{b}} - \lim_{\tau\to\infty}\left[\partial_\tau \log \mathcal{C}_{\mathcal{A}}(\tau)\right]$ or, indirectly, by fitting the exponential decay of the correlation function of Eq. (4.1.1) and extracting the smallest energy gap.

In order for this procedure to make any sense, it is necessary that the (unphysical) Bose-Fermi gap is not too large with respect to the physical excitation energies in the fermionic sector of the spectrum. If this condition is not met, the anti-symmetric correlation function gets effectively extinguished before the selection of the fermionic ground state from its excitation background is attained by imaginary-time evolution.

This condition is actually verified for infinite-U fermionic Hubbard models of moderate size, of which we will present our analysis in the following and whose properties are not too dissimilar from those of a system of hard-core bosons. The condition of a small fermion-boson gap is also met in other interesting systems, where the effects of statistics on the total energy are overwhelmed by the effects of correlations, such as the low-density electron gas, liquid ^{3}He, quasi-unidimensional systems and mixtures of bosons and fermions. It should be however remarked that the Fermi-Bose gap is, in general, an extensive property, thus providing effective restrictions on the affordable systems size.

This fermion-correlations method is related to the *transient estimate* method for the fermionic ground state, [120] or its generalization for a few excitations. [37] However, the transient estimate method works with *ratios* of decaying correlation functions, thereby reducing the signal/noise ratio, and typically uses sub-optimal bosonic guiding functions, with increased fluctuations in the weights of the random walks. A crucial point for our method to succeed is instead the calculation of spectra directly from imaginary-time correlation functions. Although, in general, this is an ill-posed problem, in practice sharp peaks with strong spectral weight can be reliably extracted if the correlation function is known with good statistical precision for sufficiently long times. [8, 93] In the fermionic Hubbard models we have analyzed this condition is met even for systems of several tens particles, due to the relatively small Bose-Fermi gap, as well as to the good quality of the variational states.

4.2 A Model for Itinerant Ferromagnetism

Ever since classical antiquity, ferromagnetism has attracted the attention of natural philosophers. [82] A proper understanding of this phenomenon was only made possible by the advent of quantum mechanics, from the early interpretations [20, 133] to its modern realizations in *quantum simulators* engineered by means of cold atomic gases. [71] In some solids, such as transitions metals, the spin-independent nature of interactions has led to conjecture that long-range magnetic order is due to an itinerant mechanism in which the Coulomb interaction and the Pauli exclusion principle play a fundamental role. The single-band Hubbard model, possibly the simplest and most studied lattice model of correlated electrons, was first thought to encompass a minimal description of itinerant ferromagnetism. [68] Recent experiments on ultra-cold atoms hinted at the formation of ferromagnetic domains in a gas of repulsively interacting fermions. [71] This important result and subsequent numerical calculations in the continuum [42, 103] suggested that this phenomenon has some general features independent on the details of the repulsive interaction, thus renewing the interest in the understanding of a minimal model for itinerant ferromagnetism. In spite of its simplicity, exact solutions of the Hubbard model are not available in more than one spatial dimension, leaving the question of the stability of a ferromagnetic phase unsolved. One of the very few exact results that is known is due to Nagaoka, [94] who proved a theorem stating that, in the infinite-U limit, a single hole stabilizes a fully-polarized ground state. Following this pioneering work, much effort has been devoted to study the fully-polarized state for finite hole densities. [48, 127, 151, 57, 12, 107, 99]. However, the possible stability of ferromagnetic phases and the nature of the involved quantum phase transitions is still matter of debate. [14, 81]

The Hamiltonian of the infinite-U Hubbard model reads:

$$\mathcal{H}_f = -t \sum_{\langle i,j \rangle,\sigma} \mathcal{P}_G c^\dagger_{i,\sigma} c_{j,\sigma} \mathcal{P}_G + h.c., \tag{4.2.1}$$

where $c^\dagger_{i,\sigma}$ ($c_{i,\sigma}$) creates (destroys) an electron on site i with spin σ; $\langle i,j \rangle$ denotes nearest-neighbor site pairs and the Gutzwiller projector $\mathcal{P}_G$ forbids double-occupancy. In the following, we will consider a square lattice and take $t = 1$ as the energy scale. The total number of sites will be denoted by L and the number of electrons by N.

4.3 Ground-State Phase Diagram

4.3.1 Back-Flow Variational Wave Function

Relatively simple variational wave functions have been constructed, [127, 151] by flipping one (say up) spin with respect to the saturated ferromagnetic state. The flip of the spin leads to a gain of kinetic energy for the down spin, but also a loss in the spin-up kinetic energy (since the motion of spin up electrons is restricted by the necessity of avoiding double occupancy). Here, we consider

$$\langle n|\Phi^{\mathrm{f}}_0\rangle = \mathcal{J}^f(n) \times \mathbf{Det}\left[\phi_k(R_j^\uparrow)\right] \times \mathbf{Det}\left[\phi_k(R_j^\downarrow)\right], \tag{4.3.1}$$

where the Jastrow factor $\mathcal{J}^f(n) = \exp\left[\sum_{i,j} V^f_{ij} n_i n_j\right]$ multiplies two Slater determinants that are constructed by applying backflow correlations to single-particle orbitals for up and down spins. [141] The correlated orbitals are defined by $\phi_k(R_j^\sigma) = \phi_k^0(R_j^\sigma) + b_k \sum_{R_l,\sigma'} \phi_k^0(R_l^{\sigma'})$, where

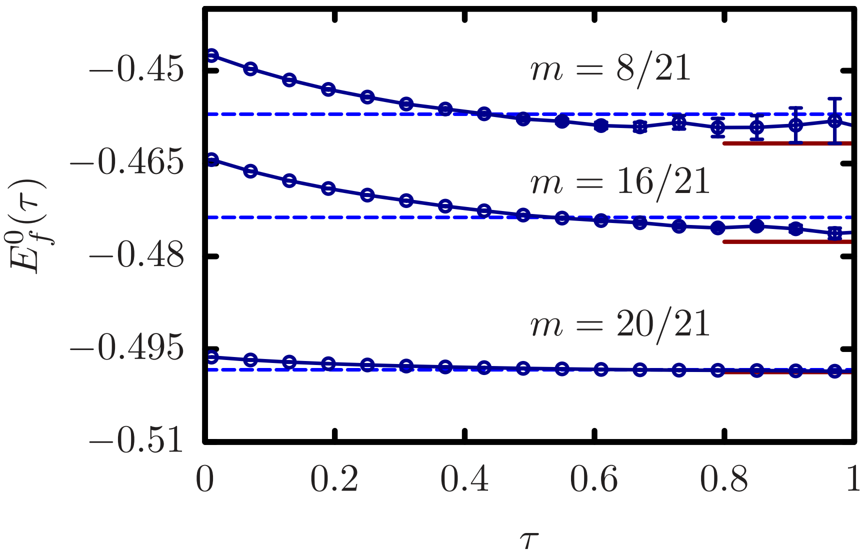

Fig. 4.2.1 Energy $E_0^{\mathrm{f}}(\tau) = E_0^{\mathrm{b}} - \partial_\tau \log \mathcal{C}_{\mathcal{A}}(\tau)$ as a function of the imaginary-time τ for $L = 50$ and $N = 42$ electrons and different magnetizations. The dashed horizontal lines are fixed-node energies, while the solid lines are the energies as obtained fitting the imaginary-time correlations.

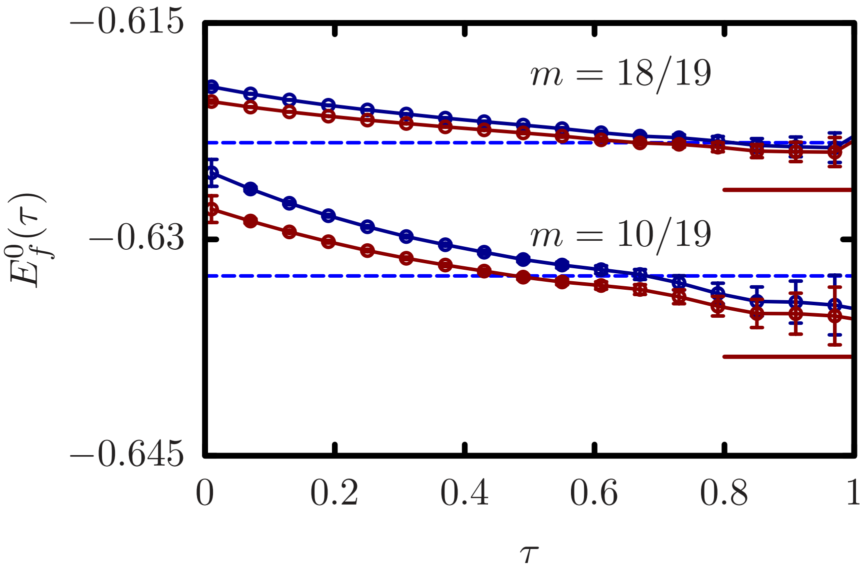

Fig. 4.2.2 Energy $E_0^{\mathrm{f}}(\tau) = E_b^0 - \partial_\tau \log \mathcal{C}_{\mathcal{A}}(\tau)$ as a function of the imaginary-time τ for $L = 50$ and $N = 38$ electrons and different magnetizations. The dashed horizontal lines are fixed-node energies, while the solid lines are the energies as obtained fitting the imaginary-time correlations.

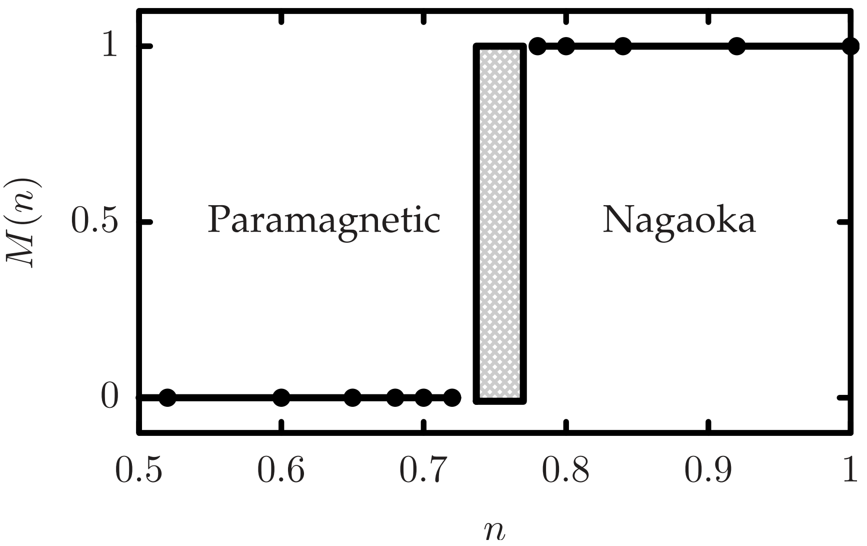

Fig. 4.3.1 Ground-state magnetization of the infinite-U Hubbard model on the square lattice. The shaded area represents a small region of uncertain attribution due to the effect of the residual Monte Carlo error.

b_k are orbital-dependent backflow parameters, $\phi_i^0(R_j^\sigma)$ are plane waves, and the sum includes all nearest neighbors of the j-th particle, thus preserving the spin rotational invariance. The proposed backflow wave function (4.3.1) encodes the effect of correlation on the deformation of the free-orbitals nodal structure and consistently catches much of the physics of previous treatments, [127, 151, 57] while leaving room for a systematic improvement with the quantum Monte Carlo methods.

The bosonic counterpart of the model studied is a purely kinetic hard-core bosons Hamiltonian, where the fermionic operators are substituted by bosonic ones. Our quantum Monte Carlo method is particularly suitable to study the high-density region, namely few holes close to full filling ($N = L$), where the boson-fermion gap is very small and increases upon decreasing the density. [11] The bosonic trial state is given by a Jastrow wave function $\langle n|\Phi_0^{\mathrm{b}}\rangle = \mathcal{J}^b(n)$, which is similar to the fermionic one (but with different parameters $V_{i,j}^b$) and represents an excellent ansatz for the bosonic ground state. [28] In all cases, the variational parameters are fully optimized, by minimizing the variational energy with the method of Ref. [128].

The fermionic correlation technique remains efficient up to relatively large system sizes (i.e., $L = 50 \div 100$) and allows us to reach numerical results, which are exact within statistical accuracy. In the following, we present the results for different magnetizations $m = (n_\uparrow - n_\downarrow)/(n_\uparrow + n_\downarrow)$ and densities $n = n_\uparrow + n_\downarrow$. In Fig. 4.2.1, we report our results for $L = 50$ and $N = 42$ electrons, for different values of the magnetization, m. In addition, we also report the results based upon the fixed-node approach. The possibility to obtain numerically exact results on rather large systems allows us to assess the accuracy of the fixed-node method that can be extended to much larger sizes (i.e., $L \lesssim 1000$), without any numerical instability. Thanks to backflow correlations, we get a considerable improvement upon the standard plane waves that has been used in Ref. [12]. There is a small difference between the fixed-node results and the energies obtained by the imaginary-time correlations, indicating a very small residual fixed-node error. In Fig. 4.2.2 we show a comparison between the fermionic correlation energies and the fixed-node approximation, close to the transition density. It can be noticed that the estimated error for the fixed-node energies (which are the dashed horizontal lines) is safely estimated to be $\Delta E/t \lesssim 0.01$.

In Fig. 4.3.1, we report the overall phase diagram obtained by considering large-scale fixed-node calculations. A saturated ferromagnetic phase is stable for $n \gtrsim 0.75$, while for smaller densities a paramagnetic ground state is found. The narrow shaded region denotes the incertitude due to the residual numerical error, which can be estimated by comparing the fixed-node energies with the *exact ones* (obtained from the fermionic correlations) on smaller clusters, see

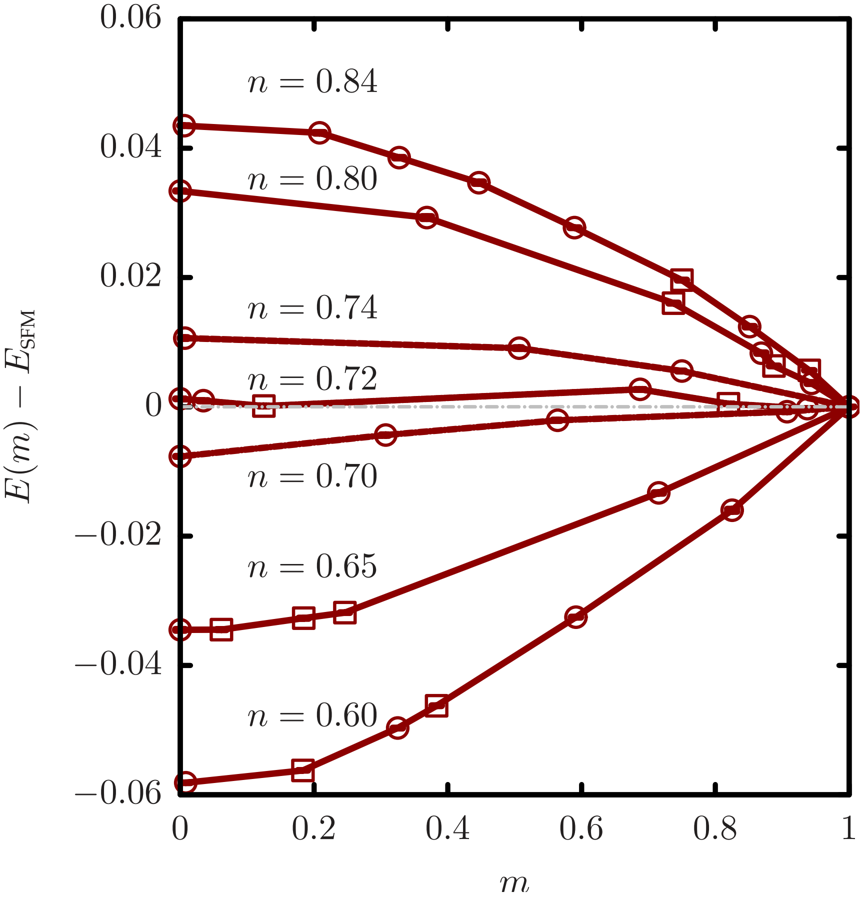

Fig. 4.3.2 Difference between the energy per site of different magnetizations and the one of the saturated ferromagnet as a function of the density n. The cases with $L = 200$ (squares) and $L = 400$ (circles) are reported; lines connecting points are a guide for the eye.

Fig. 4.2.1. This direct comparison puts us on secure grounds as concerns the robustness of the dependence of the ground-state magnetization on the electron density.

In Fig. 4.3.2 we display the dependence of the ground-state energy upon magnetization, for different values of the electron density. The remarkable feature emerging from this figure is the strong flattening of the energy as a function of the magnetization (i.e., the spin) close to the transition between the fully-polarized ferromagnet and the paramagnetic state. Indeed, at low and high densities the energy has a monotonic behavior as a function of the magnetization m. At low density a clear minimum exists at $m = 0$, typical of a paramagnetic phase, where the curvature of the energy-versus-magnetization curve witnesses to a finite spin susceptibility. On the other hand, in the high-density ferromagnetic phase, $E(m)$ displays a well defined minimum for $m = 1$. By approaching the transition, $E(m)$ becomes flatter and flatter, suggesting that the susceptibility may diverge at the critical point. Although we cannot exclude a tiny region with a finite but non-saturated magnetization, these results would suggest that the paramagnetic-to-ferromagnetic transition is not due to a simple level crossing, namely to the creation of a local minimum in $E(m)$ at $m = 1$ that eventually prevails over the paramagnetic one, but rather to the progressive flattening of the *whole* $E(m)$ curve.

4.3.2 Infinite-Order Phase Transition

Our scenario is compatible with an infinite-order phase transition, which, in general, is described by $E(m) = (g - g_c)m^2 + bm^{2r}$, where $r \to \infty$; a phase transition is obtained by varying the order parameter g (in our case the electron density) across its critical value g_c. The critical exponent of the order parameter is $\beta = 1/(2r - 2)$, generating a jump from zero to the saturation value for $r \to \infty$. Moreover, the susceptibility $\chi \sim A_\pm/|g - g_c|^\gamma$ has an exponent $\gamma = 1$ independent of r, with an amplitude ratio A_-/A_+ that vanishes for $r \to \infty$. [15] Even though the order parameter shows a finite jump, like in ordinary first-order phase transitions, there is no hysteresis. We have indeed verified that the ground-state energy is a convex function of the electron density (see Fig. 4.3.3), implying a finite compressibility in the neighborhood of the ferromagnetic-paramagnetic transition. This picture implies that spin-flip excitations over the fully-polarized state are non-interacting at the transition point. In fact, we find that, at small distances, the minority spins repel each other, whereas at large distances they do not interact. In the variational wave function, this fact generates a sizable repulsive short-range Jastrow factor, while at long range the $V^f_{i,j}$ *pseudopotential* vanishes.

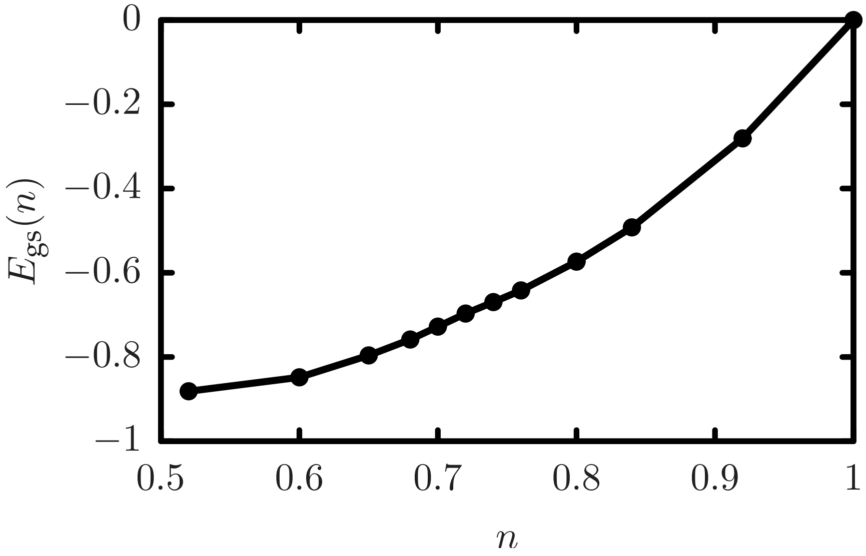

Fig. 4.3.3 Ground-state energy of the infinite-U Hubbard model on the square lattice as a function of the electron density.

4.4 Effect of a Density Interaction

In pursuing the program to describe ferromagnetism within a purely spin rotationally invariant Hamiltonian, it is natural to envisage a more realistic situation in which the electrons experience a mutual density-density interaction too. With this in mind, we have studied the stability of the Nagaoka state with respect to a nearest-neighboring interaction, namely the extended-Hubbard Hamiltonian in the infinite-U limit $\mathcal{H}_{\text{ext}} = -\sum_{\langle i,j \rangle} \sum_{\sigma} \mathcal{P}_G c^{\dagger}_{i\sigma} c_{j\sigma} \mathcal{P}_G + \text{h.c.}, +V \sum_{\langle i,j \rangle} n_i n_j$ where V is the strength of the density-density potential. This Hamiltonian preserves the $SU(2)$ spin rotational invariance and it has been conjectured to have a stable ferromagnetic phase, from purely perturbative arguments. Moreover, it is a prominent candidate for future experimental studies with two component Fermi gases in optical lattices with tunable intra-species interactions.[72, 21]

To study the physics of this system we choose a variational back-flow wave-function of the same form of (4.3.1) and checked whether a possibly strong interaction could destroy ferromagnetism in its region of stability at $V = 0$. In Figure 4.4.1 we show the fixed-node energies as a function of the polarization, at the density $n = 0.84$ for different values of V. It is quite noticeable that even a strong interaction leaves the ferromagnetism stable, emphasizing the role of the infinite on-site Coulomb repulsion as a crucial ingredient for the itinerant ferromagnetism in absence of frustration.

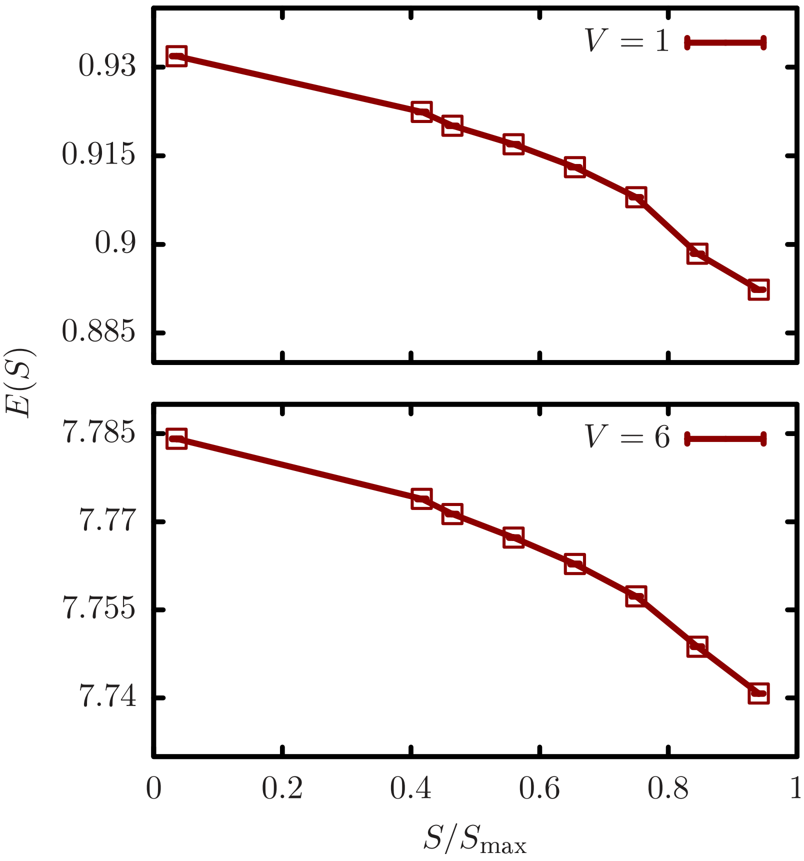

Fig. 4.4.1 Ground-state energy as a function of the total spin and for different values of the interaction strength V at density $n = 0.84$. Lines connecting points are a guide for the eye, the lattice size is $L = 200$ sites.

4.5 Conclusions

In this Chapter we have shown that unbiased ground-state properties of a fermionic system can be studied by means of imaginary-time correlations of an auxiliary bosonic problem. As an application, we have analyzed with high accuracy the magnetic phase diagram of the fermionic Hubbard model on the square lattice in the limit of infinite on-site repulsion U. By the combination of different quantum Monte Carlo methods, we have been able to give a very precise determination of the transition between the ferromagnetic and the paramagnetic states.

Interestingly,we have found that all spin excitations become essentially gapless at the transition, possibly indicating that the transition is of infinite order. Compared to previous calculations, this is the first time that such a behavior has been observed. Indeed, given the extreme difficulty to treat this highly-correlated system, most of the theoretical efforts were limited to study very high densities or a single spin flip. [48, 127, 151, 57] Our results pave the way to a better understanding of itinerant ferromagnetic phenomena in both traditional condensed matter systems and in recent and forthcoming realizations of such phases in cold atomic gases. Indeed, the recent achievements for the realization of interacting fermionic systems trapped in optical lattices [72] will most likely lead to experimentally probe the strongly-correlated regime of the Hubbard model at sufficiently low temperatures. Lastly, the generality of the numerical methods introduced in [34] and hereby reviewed, will also offer new insights in other strongly correlated fermionic systems where currently available analytical and numerical treatments may fail to offer a quantitative or even qualitative account of the relevant physical properties.

Chapter 5

Finite-Temperature Susceptibilities

Bose-Einstein Condensation in Quantum Glasses

The emergence of an ordered pattern in a sample of matter is often an indication of the tendency of the system to break some physical symmetry and give rise to a phase transition. However, as much as for ferromagnetic order in absence of an external field and for other forms of spontaneous symmetry breaking, these phenomena cannot be directly observed on any *finite* sample but only in the thermodynamic limit. The characterization of a given phase transition and the determination of the properties of the phases themselves, is therefore in numerical simulation left to a careful analysis of other properties which are well defined indicators of the intrinsic phase change on a finite system.

We have shown in 1.3.2 that imaginary-time dynamics allows for the study of static susceptibilities, which represent both theoretical and experimental precious tools to characterize the response of a quantum system to an external (small) perturbation and can be carefully used to determine the tendency of a system to break some symmetry associated to the external perturbing field. In this Chapter we show an application of imaginary-time dynamics to the finite-temperature study of a very intriguing novel phase of matter characterized by both amorphous, glassy, order and Bose-Einstein condensation. In particular we have characterized and demonstrated the existence of a novel quantum phase featuring both Bose-Einstein condensation and spin-glass behaviour [35]. The mechanism inducing the coexistence of these two orders is very different from the one inducing localization in the insulating “Bose-glasses” and could be experimentally probed in future experiments.

In Sec. 5.1 we introduce both a finite-temperature quantum Monte Carlo method and a mean-field numerical tool particularly useful for our analysis of quantum glasses. In Sec. 5.2 the experimental findings and the theoretical problems concerning the current understanding of “superglasses” are introduced and in Sec. 5.3 our model for the existence of Bose-Einstein condensation in quantum glasses is presented. We account for and demonstrate the spin-glass nature of this model in 5.4; in Sec. 5.5 we discuss recently obtained related results and finally draw our conclusions.

5.1 Finite-Temperature Methods for Strongly Correlated Systems

In order to characterize the finite-temperature equilibrium properties of a quantum system, the canonical partition function $\mathcal{Z} = \mathbf{Tr}\, e^{-\beta\mathcal{H}}$ at finite temperature $T = 1/\beta$ can be considered. The basic structure of the canonical partition function is that of an imaginary-time projection in which the inverse temperature plays the role of the total imaginary projection time. Therefore, stochastic methods devised to simulate the imaginary-time dynamics of quantum systems can be conveniently modified and successfully applied to the study of finite-temperature properties. In this Section we first present a quantum Monte Carlo method which, in general, provides numerically exact properties of any finite bosonic system on an arbitrary lattice. We later consider also a recently introduced method which is exact only on particular class of graphs, such as the Bethe lattices, which has nonetheless the advantage of giving physical properties already in the thermodynamic limit. Both methods have a wide range of applicability and, in particular, they have been used in our study of quantum glasses.

5.1.1 Stochastic Sampling of the Canonical Partition Function

The stochastic sampling of the quantum partition function can be conveniently exploited to obtain numerically exact properties of a generic bosonic Hamiltonian $\mathcal{H} = -\mathcal{T} + \mathcal{V}$, where we have isolated the kinetic $\mathcal{T}$ and the potential terms $\mathcal{V}$. Finite-temperature quantum Monte Carlo schemes based on the original Worm algorithm idea [106] have been recently extended to Canonical ensemble simulations [112, 115]. These methods offer an efficient scheme based on the sampling of the configuration space spanned by the extended partition function $\mathcal{Z}_{\mathcal{W}}(\beta,\tau) = \mathbf{Tr}\, e^{-(\beta-\tau)\mathcal{H}}\mathcal{W}e^{-\tau\mathcal{H}}$, where $\mathcal{W}$ is a suitable *worm* operator determining an imaginary-time discontinuity in the world-lines. For our analysis, we have chosen the worm operator introduced in [115], which is a linear superposition of n-body Green functions, avoiding the complications arising in [112] where the commutability of the worm operator with the non-diagonal part of the Hamiltonian is required. The extended partition function is in turn expanded by means of a finite-temperature Dyson expansion, which guarantees the lack of time-discretization error and reads

$$\mathcal{Z}_{\mathcal{W}}(\beta,\tau) = \sum_{n}\sum_{\mathbf{x}_0\cdots\mathbf{x}_n}\int_{0<\tau_1<\cdots<\tau_n<\beta} e^{-\beta\mathcal{V}(\mathbf{x}_0)} \langle\mathbf{x}_0|\,\mathcal{T}(\tau_n)\,|\mathbf{x}_{n-1}\rangle \langle\mathbf{x}_{n-1}|\,\mathcal{T}(\tau_{n-1})\,|\mathbf{x}_{n-2}\rangle \times \ldots$$

$$\langle\mathbf{x}_L|\,\mathcal{W}(\tau)\,|\mathbf{x}_R\rangle \times \ldots \langle\mathbf{x}_2|\,\mathcal{T}(\tau_2)\,|\mathbf{x}_1\rangle \langle\mathbf{x}_1|\,\mathcal{T}(\tau_1)\,|\mathbf{x}_0\rangle\,. \quad (5.1.1)$$

The configurational space spanned by the Dyson paths are depicted in Fig. 5.1.1, where each dot represents a many-body configuration at a given imaginary-time and periodic boundaries are due to the cyclic properties of the trace. An important difference between the Dyson series approach and the path-integral one, is that in the first case an additional summation over the perturbative order (i.e. the number of dots in Fig. 5.1.1) is required. Apart from this difference, which has to be carefully treated when devising a stochastic method, the general formalism and potentialities are otherwise identical with the path-integral case. For example, two-points imaginary-time correlations can be indeed easily obtained upon considering the value of the observable at distinct pair of points in the periodic imaginary times spanned by the Dyson configurations.

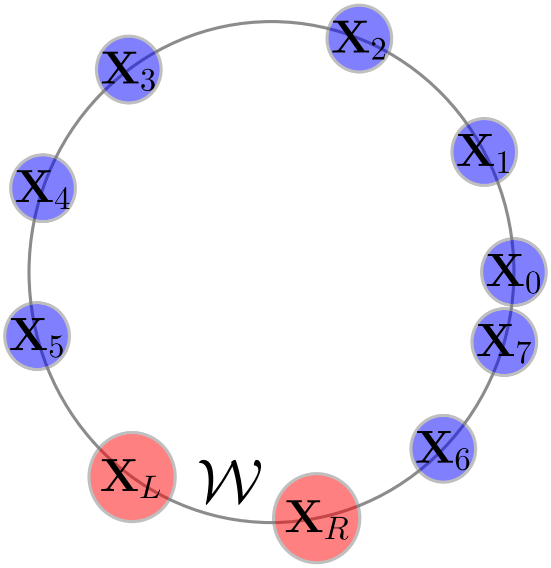

Fig. 5.1.1 Graphical representation of the configurational space of the Dyson series for the the extended partition function at finite temperature. Dots represent many-body configurations at given imaginary times in the interval $[0, \beta)$. Blue points are connected by the off-diagonal part of the Hamiltonian, whereas the worm operator connects the two red points.

Full details of the sampling strategy adopted by the Stochastic Green Function (SGF) method are given in Ref. [115], we only stress here that this particular algorithm gives full access to exact equal-time thermal averages of n-body Green functions as well as to thermal averages of imaginary-time correlation functions of local, i.e. diagonal in the occupation numbers representation, quantum operators.

5.1.2 The Quantum Cavity Method

A different and complementary approach to models defined on Bethe lattices, or, their topologically equivalent random graphs, consists in solving them exactly in the thermodynamic limit $L \to \infty$, by means of the *cavity method* [89]. Since local observables are self-averaging in this limit, this results in automatically taking into account the average over the different realizations of the random graphs which is particularly useful for model with disordered interactions. For bosonic systems, the cavity method allows to reduce the solution of the model to the problem of finding the fixed point of a functional equation for the local effective action, in a similar spirit to bosonic DMFT. All the details of the computation have been discussed in [125], where it has been shown that the method allows to compute the average of all the relevant observables. However, in the simplest version discussed in [125], the cavity method can only describe homogeneous pure phases such as the low-density liquid. In order to describe exactly the high density glassy phase, where many different inhomogeneous states coexist, one has to introduce a generalization of the simplest cavity method which goes under the name of *replica symmetry breaking* (RSB). Unfortunately, this is already a difficult task for classical models, in particular in spin-glass like phases [89]. Hence, we describe the glassy phase using the simplest version of the method, the so-called replica symmetric (RS) one. This yields an approximate description of the glassy phase which we expect to be qualitatively correct. In the glassy phase, the RS cavity method is only approximate, an exact solution for $L \to \infty$ requiring the introduction of RSB. On the other hand, quantum Monte Carlo methods are limited for large L by the unavoidable divergence of equilibration times due to the glassy nature of the system. Still, we have generally found a very good agreement between the results obtained by means of the unbiased Stochastic Green Function method for fairly large L, where the system can still be equilibrated, and the RS cavity method for $L \to \infty$.

5.2 Quantum Glasses, Localization and the Superglass Phase

Quantum particles moving in a disordered environment exhibit a plethora of non-trivial phenomena. The competition between disorder and quantum fluctuations has been the subject of vast literature [2, 51] in past years, with a renewed interest following from the exciting frontiers opened by the experimental research with cold-atoms [111, 16]. One of the most striking features resulting from the presence of a disordered external potential is the appearance of localized states [2]. Localization happens both for fermions and bosons [51], but in the latter case one has to introduce repulsive interactions to prevent condensation of particles in the lowest energy state. This results in the existence of an *insulating* phase called “Bose glass”, characterized by a finite compressibility and gapless density excitations in sharp contrast to the Mott insulating phase [51, 77].

On the other hand, latest research stimulated by the discovery of a supersolid phase of Helium has brought to the theoretical foresight of a “superglass” phase [23, 17], corroborated by recent experimental evidence [69], where a metastable amorphous solid features both condensation and superfluidity, *in absence of any random external potential*. The apparent irreconcilability, between the current picture of insulating “Bose glasses" and the emergence of this novel phase of matter, calls for a moment of thought. Although it has been recently demonstrated that *attractively* interacting lattice bosons can overcome the localization induced by an external random potential and feature a coexistence of superfluidity and amorphous order [44], a general understanding of the physics of Bose-Einstein condensation in quantum glasses and in the presence of purely repulsive interactions is still in order. In particular, we wonder what could be the possible microscopic mechanism leading to super-glassines and if the external disorder, current paradigm in the description of quantum glasses, could be replaced by some other mechanism.

In [35] we have shown that geometrical frustration is the missing ingredient. Geometrical frustration is a well recognized feature of disordered phases in which the translational symmetry is not explicitly broken by any external potential. Examples are spin liquids phases of frustrated magnets [29], valence-bond glasses [138] and the *order-by-disorder* mechanism inducing supersolidity on frustrated lattices [148]. Another prominent manifestation of frustration is the presence of a large number of metastable states that constitutes the fingerprint of spin-glasses. When quantum fluctuations and geometrical frustration meet, their interplay raises nontrivial questions on the possible realization of relevant phases of matter. Most pertinently to our purposes: can quantum fluctuations stabilize a superglass phase in a *self-disordered* environment induced by geometrical frustration? Hereby we review our proposed answer to this question, demonstrating that repulsively interacting bosons can feature a low-temperature phase characterized both by spin-glass order and Bose-Einstein condensation. Such a frustration induced superglass sheds light onto a novel mechanism for glass formation in bosonic systems noticeably different from the localization effects leading to “Bose glass" insulators and paving the way to a better understanding of this new phase of the matter.

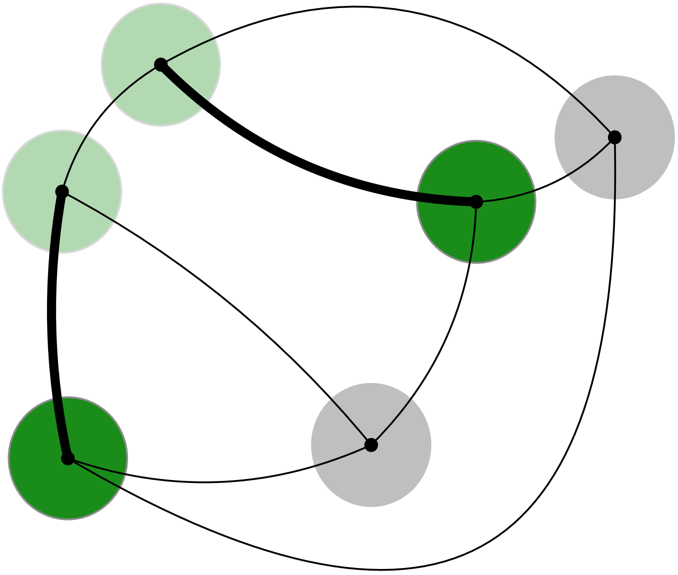

Fig. 5.2.1 Example of a small random graph with connectivity $z = 3$ and for hard-core bosons at half filling. Full green circles represent occupied sites. Due to geometrical frustration there is more than one configuration that minimize the potential energy. In this example, the highlighted nearest-neighboring bonds are frustrated in either of the two configurations represented in the picture (light green circles).

5.3 A Model for the Superglass Phase and the Role of Frustration

Strongly interacting bosons on a lattice can be conveniently described by means of the extended Hubbard Hamiltonian, namely

$$\mathcal{H} = -t \sum_{\langle i,j \rangle} \left[b_i^\dagger b_j + b_i b_j^\dagger \right] + V \sum_{\langle i,j \rangle} n_i n_j, \tag{5.3.1}$$

where $b_i^\dagger (b_i)$ creates (destroys) a hard-core boson on site i, $n_i = b_i^\dagger b_i$ is the on-site density and the summations over the indexes $\langle i,j \rangle$ are extended to nearest-neighbor vertices of a given lattice with L sites. In the following we will set $t = 1$, i.e. we will measure all energies in units of t.

In order to capture the essential physics of the problem in exam, we adopt a minimal and transparent strategy to induce geometrical frustration in the solid. We therefore consider the set of *all possible graphs* of L sites, such that each site is connected to *exactly* $z = 3$ other sites, and give the same probability to each graph in this set. We will discuss average properties over this *ensemble* of random graphs in the thermodynamic limit $L \to \infty$.

The motivations for this choice are the following:

- On a square lattice, model (5.3.1) is known to produce a solid insulating phase at high enough density, where the particles are arranged in a checkerboard pattern [126]. This is due to the fact that all loops have even length. On the contrary, typical random graphs are characterized by loops of even or odd length; in the classical case $t = 0$, this frustrates the solid phase enough to produce a *thermodynamically stable* glass phase at high density [89]. An exemplification of the geometrical frustration induced by the topology of the graph and the density-density interaction is shown in Fig. 5.2.1.
- Typical random graphs have the important property that they are locally isomorphic to trees, since the size of the loops scales as $\ln L$ for large L: indeed, this is a consistent way of defining Bethe lattices without boundary [89]. This locally tree-like structure allows to solve the model exactly, at least in the liquid phase, by means of the cavity method [80, 125].
- These lattices are quite different from square lattices. Yet, it has been shown in the classical case, and for some more complicated interactions, that the phase diagram is qualitatively very similar for the model defined on a random graph and on a square lattice [19, 39]. Hence, we believe that it is possible to find a model similar to Eq. (5.3.1), defined on a square lattice but with slightly more complicated interactions (probably involving many-body terms) that will show the same qualitative behaviour of the model investigated here.

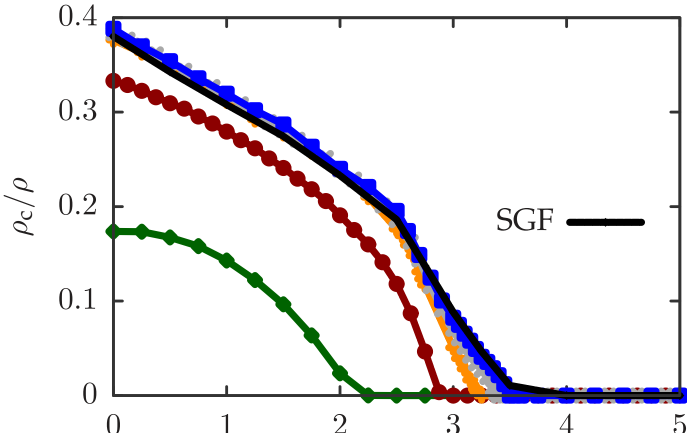

Fig. 5.3.1 Condensate fraction ρ_c/ρ as a function of the interaction strength V at half-filling, computed via the cavity method at different values of β. Results for ρ_c/ρ as obtained by the Stochastic Green Function (SGF) at $\beta = 5$ are reported.

5.3.1 Results

The presence of off-diagonal long range order and therefore the onset of Bose-Einstein condensation can be conveniently detected by considering the large separation limit of the one-body density matrix, i.e. the condensate density reads

$$\rho_c = \lim_{|i-j|\to\infty} \overline{\left\langle b_i^\dagger b_j \right\rangle} = \overline{|\langle b_i \rangle^2|}\,, \tag{5.3.2}$$

where the square brackets indicate a quantum and thermal average and the bar indicates averages over independent realizations of the random graphs. The cavity method works in the grand-canonical ensemble and gives direct access to the average of b, while canonical ensemble simulations done with the Stochastic Green Function method give easy access to the one-body density matrix. On the other hand, spin-glass order is signaled by the breaking of translational invariance, namely $\langle n_i \rangle \neq L^{-1} \sum_{i=1}^{L} \langle n_i \rangle = \rho$ which, strictly speaking, can take place only in the thermodynamic limit. Introducing $\delta n_i = (n_i - \rho)$, the on-site deviation from the average density, spin-glass order can be quantified by the Edwards-Anderson order parameter

$$q_{\text{EA}} = \frac{1}{L} \sum_{i=1}^{L} \overline{\langle \delta n_i \rangle^2}, \tag{5.3.3}$$

which can be easily computed by the cavity method in the thermodynamic limit.

The emergency of a spin-glass behavior on a finite system is, on the other hand, conveniently identified by the divergence of the associated spin-glass susceptibility

$$\chi_{\text{SG}} = \frac{1}{L} \int_0^\beta d\tau \sum_{i,j} \overline{\langle \delta n_i(0) \delta n_j(\tau) \rangle^2}, \tag{5.3.4}$$

which, as per usual susceptibilities introduced before, has the form of a two-point imaginary-time correlator and it is accessible with a suitable finite-temperature quantum Monte Carlo method as the Stochastic Green Function. It is possible to show [65] that χ_{SG} is the susceptibility naturally associated to the order parameter q_{EA}, because it can be defined as the derivative of q_{EA} with respect to an external field coupled to the order parameter itself (as in standard critical phenomena).

At half-filling factor $\rho = 1/2$, the condensate fraction, the Edwards-Anderson order parameter, and the scaled spin-glass susceptibility are shown respectively in Figs. 5.3.2-5.3.3. In Fig. 5.3.2 we also show a comparison between the values of the condensate fraction obtained via the cavity method and via Stochastic Green Function in a linear extrapolation to $L \to \infty$. The very good coincidence of these results supports our conjecture that the approximate RS description of the glass phase we adopted here is quantitatively and qualitatively accurate. At the lowest temperature, the system becomes a glass around $V \sim 2.7$ while it still displays BEC; the con-

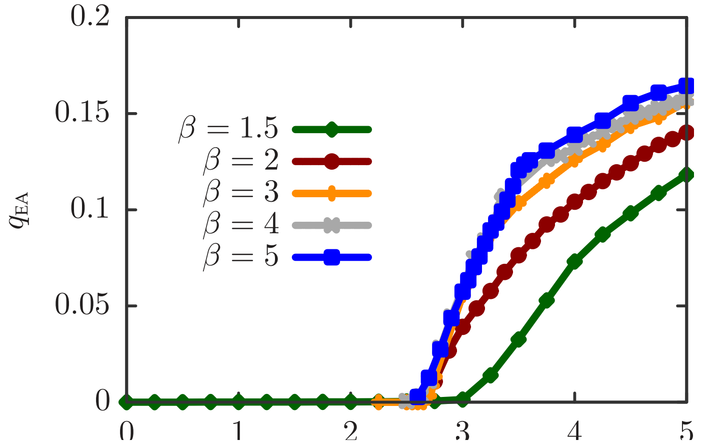

Fig. 5.3.2 Edwards-Anderson order parameter as a function of the interaction strength V at half-filling, computed via the cavity method at different values of β.

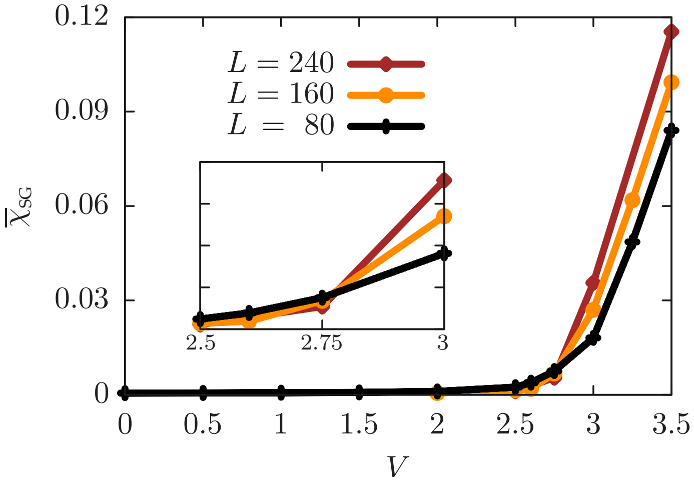

Fig. 5.3.3 Scaled spin-glass susceptibility $\overline{\chi}_{\mathrm{SG}} = \chi_{\mathrm{SG}}/L^{5/6}$ reported as a function of the interaction strength V. Standard finite-size-scaling arguments [65] show that the different curves must intersect at the spin-glass transition. Results are obtained by the Stochastic Green Function method.

densate fraction only vanishes at $V \sim 3.5$ inside the glass phase. This clearly establishes the existence of a zero-temperature superglass phase in the region $2.7 \lesssim V \lesssim 3.5$. Note additionally that both transitions are of second order, hence the condensate fraction is a continuous function; since the latter stays finite on approaching the spin-glass transition from the liquid side (where the cavity method gives the exact solution), it must also be finite on the glass side just after the transition. In Fig. 5.3.4 we report the finite-temperature phase diagram of the model at half-filling. It is defined by two lines: the first separates the non-condensed ($\langle b \rangle$=0) from the BEC ($\langle b \rangle \neq 0$) phase, the second separates the glassy ($q_{\mathrm{EA}} \neq 0$) from the liquid ($q_{\mathrm{EA}} = 0$) phase.

The intersection between these two lines determines the existence of four different phases (normal liquid, superfluid, normal glass, superglass).

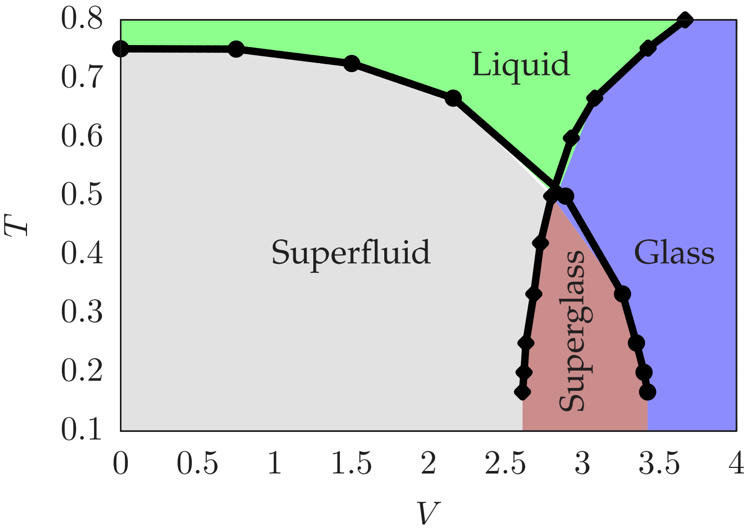

Fig. 5.3.4 finite-temperature phase diagram of the extended Bose-Hubbard Hamiltonian on a $z = 3$ random graph at half-filling, where V is the density-density interaction strength. A finite region characterized by the coexistence of Bose-Einstein condensation and glassy behavior is clearly visible.

5.4 Ground-State Degeneracy and Spin-Glass Nature

Geometrical frustration induces the existence of a highly degenerate set of ground states, each of them characterized by a different average on-site density, which is absent in glassy phases induced by localization in disordered external potentials such as the Bose glass. To demonstrate this peculiar feature, it is instructive to consider a variational wave-function explicitly breaking the translational symmetry of the lattice

$$\langle \mathbf{n} \,|\Psi_\alpha\rangle \propto \exp\left[\sum_i \alpha_i n_i\right], \qquad (5.4.1)$$

where the variational parameters α_i are explicitly site-dependent and tend to (dis)-favour the occupation of a given site. In the spin-glass phase of the bosons, the optimal set of the variational parameters is highly dependent on the initial conditions associated with the α_i, whereas all the variational states, even with different parameters, have almost degenerate variational energies. Each set of optimized variational parameters is then representative of one of the many degenerate ground states of $\mathcal{H}$. As an example, we show in Fig. 5.4.1 the variational expectation values of the site densities for two different solutions resulting from the minimization of the variational energy with the SRH method [128], a robust stochastic variant of the Newton Method. We further checked, using the zero-temperature Green Function Monte Carlo method [130], that if one applies the imaginary-time evolution $|\phi_\alpha\rangle = \exp(-\tau\mathcal{H})\,|\Psi_\alpha\rangle$ to one of these states, the density profile remains amorphous for a time τ that is divergent with the size of the system.

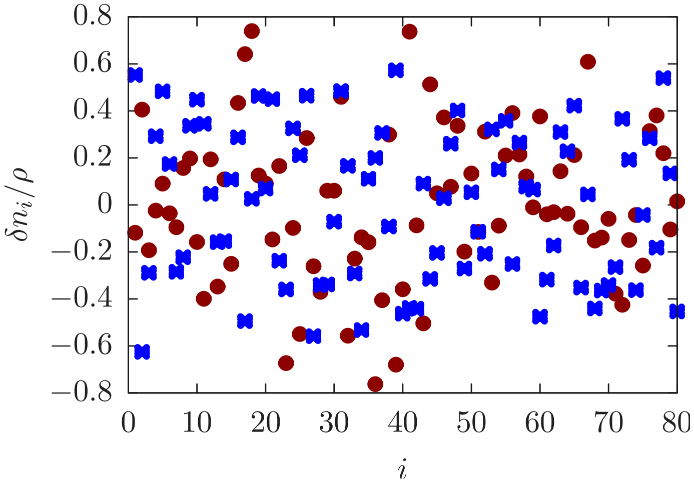

Fig. 5.4.1 Variational expectation values of the site density for different sets of the optimized parameters at half-filling density for $L = 80$ and $V = 4$.

5.5 Conclusions

The aim of this Chapter was to show a successful application of finite-temperature methods and imaginary-time correlations to the characterization of a novel phase of matter. In particular we have established the existence of a stable superglass phase in a lattice model of geometrically frustrated bosons, in absence of quenched disorder in the Hamiltonian. This has been done by combining the analytical solution of the model via the quantum cavity method and numerical simulations via Quantum Monte Carlo. The glass phase we found is very different from the usual Bose glass, since the latter is driven by localization effects in presence of an external disorder and is then insulating, while the former is driven by self-induced frustration on a disordered lattice and displays Bose-Einstein condensation. This results in a coexistence of a large number of degenerate amorphous ground states, whose existence we showed by a variational argument corroborated by quantum Monte Carlo. We expect, by analogy with the classical case [19], that the glassy phase found here will exist also on regular finite dimensional lattices, provided the interactions are modified to induce sufficient geometrical frustration. In that case, its properties should be very similar to the one showed by metastable superglasses observed both in numerical simulations [23] and experiments [69] on Helium 4. The main difference is that, due to the randomness of the underlying lattice, the superglass studied here is a *truly stable equilibrium state*, allowing for a much more precise characterization of its properties.

We conclude the discussion on the existence of superglass phases induced by geometrical frustration noticing that a similar scenario is realized when random interactions on a regular lattice are chosen. In particular, the interesting outcome of Ref. [136] is that a random two-body density-density interaction on a cubic lattice can stabilize a superglass phase and give rise to a finite-temperature phase diagram qualitatively close to the one we have obtained and shown in Fig. 5.3.4. Classical (magnetic) realistic systems realizing effectively random two-body interactions are known and have been studied as prototypical examples of spin-glasses. Their quantum counterparts are still to be identified but a number of possible candidates both in the field of frustrated quantum magnets and trapped cold-atoms exist and future research will be devoted to their identification.

Part II

Real Time Dynamics

Out-of-Equilibrium Properties

> Τοὺς δὲ μέθ᾽ ὁπλότατος γένετο Κρόνος ἀγκυλομήτης,
> δεινότατος παίδων· θαλερὸν δ᾽ ἤχθηρε τοκῆα.

Hesiod, “*Theogony*” verses 137-138

Chapter 6

Exact Dynamics After A Quantum Quench

Localization and Glassy Dynamics of Many-Body Quantum Systems

Isolated physical systems are an idealization which is practically never perfectly realized in nature. Matter is indeed regularly driven out of equilibrium and its physical properties are consequently affected. Perturbations to an underlying state of equilibrium of a physical system can be of diverse nature and can be often regarded as an external disturbance. The external disturbance is the effective result of the complex interactions taking place between a large environment and the small portion of which we are examining.

It is however often the case that either the external disturbance acts for a relatively short amount of time or that the external environment acts in a rather smooth and controlled way. In such a circumstance, even though the physical system is not isolated from the external environment, it nonetheless reaches a kind of stationary state in which physical quantities of interest are expected not to exhibit large fluctuations in time. A characterization of the macroscopic properties of the system in terms of an equilibrium, time-independent, picture is often very accurate and of paramount importance in the study of classical physical systems ranging from simple fluids to complex biological matter.

At the very roots of the possibility to provide a stationary description of these phenomena there is the ergodicity axiom in classical statistical mechanics, brought by the intuition of Ludwig Boltzmann in the nineteenth century. The ergodicity axiom states that, during its time evolution, a macroscopic system uniformly explores the entire phase space compatible with conservation laws, so that the time average of any observable comes to coincide with the micro-canonical ensemble average and, when the observable is local, also with the canonical Gibbs ensemble average. Nonetheless, ergodicity can be violated in classical systems, a noticeable example being glasses. [98] Quantum effects might also spoil ergodicity by preventing the wave function from diffusing within all available configurations. This phenomenon is actually known to occur in the presence of disorder and manifests itself either by single-particle [2] or many-particle [9, 95, 96] wave function localization. However, alike classical models for glassy behavior, ergodicity breakdown in the quantum dynamics may not necessarily require disorder and it could instead be entirely due to frustrating dynamical constraints. [19, 52]

An extremely important difference between the classical and the quantum case is that, from a practical point of view, the validity of the ergodicity axiom can be extensively assessed in the first case whereas it cannot be assessed in an exact fashion for a generic (non-integrable) quantum system. The very difference between the two cases is indeed in the manifestly different nature of the mathematical description of the physical time evolution. In the classical case, the Newton equations of motion do not present, in principle, any conceptual problem in their exact numerical solution and, in practice, the current evolutionary state of technology allows for the simulation of even very intricate and large systems in a controlled amount of computational time. On the other hand, the mathematical description of the quantum dynamics and the large physical (Hilbert) space in which a quantum state is described, are intrinsically more demanding objects. This complexity hinders the possibility to specifically assess the validity of the ergodicity principle and poses serious and restrictive limitations on the dimensions of the systems whose exact dynamics can be studied.

In this Chapter we present some existing numerical methods that are able to treat, with some important restrictions that will be highlighted, the dynamical properties of quantum one-dimensional systems and we will review some of the numerical evidences we have presented in Ref. [31]. In particular we will show that an isolated system of strongly interacting bosons, modeling atoms in optical lattices, can be trapped during its evolution into long-lived inhomogeneous metastable states, provided that its internal energy exceeds a certain threshold. We argue that the slowing down of high-energy incoherent excitations in the strongly correlated system is the key feature responsible for this dynamical arrest, much resembling a kind of glass transition. By formulating the problem in a different language, we also explicitly show that a system initially prepared in a inhomogeneous state is unable to diffuse within the entire configurational space; such a dynamical localization in the many-body Hilbert space looks intriguing and may represent a kind of many-body Anderson localization [9] that occurs without disorder. The above phenomenon is put in further relation with and deemed responsible for the lack of ergodicity observed in large finite size systems.

6.1 Exact Methods for the Quantum Dynamics

The dynamical evolution of a wave-function induced by a quantum Hamiltonian $\mathcal{H}$ is governed by the the Schrödinger equation

$$\frac{d}{dt}\Psi(\mathbf{x},t) = -i\sum_{\mathbf{y}}\mathcal{H}_{\mathbf{x},\mathbf{y}}\Psi(\mathbf{y},t), \tag{6.1.1}$$

where bold variables denote many-body configurations in a (discrete) Hilbert space. Eq. (6.1.1) is a system of first-order ordinary differential equations and, in principle, does not present any difficulty in its solution, whenever the initial condition $\Psi(\mathbf{x},0)$ is provided. However, the number of coupled differential equations grows with the dimensionality of the Hilbert space of the problem which in turn has typically an exponential growth in the system size. This circumstance poses serious restrictions on the affordable system sizes that can be studied and limits the numerical study mainly to one dimensional geometries, for which the dimensionality of the Hilbert space is smaller than higher dimensional counterparts.

The first method we describe here, in 6.1.1, is based on the exact solution of the bare Schrödinger equation (6.1.1), which, apart from the restriction on the possible system sizes accessible, does not suffer from any approximation. The second method outlined in the following,in 6.1.2, is based on a different idea, namely on the possibility in most low-dimensional systems to reduce the full size of the Hilbert space into a much smaller effective space, which encodes all the relevant physical information. This approach is not limited to small systems but suffers from other important drawbacks that will be explained. A third scheme, which will be particularly useful in the following, is instead based on the construction of a particular basis of orthonormal vectors in which the Hamiltonian has a simple tridiagonal form and it is described in 6.1.3.

6.1.1 Series Expansion for the Schrödinger Evolution

One of the major problems arising in the numerical solution of the system of ordinary differential equations (6.1.1) is that an intrinsic discretization of time is needed which leads to a systematic error that grows with time. Even though the error can be controlled with appropriate high order integration schemes such as the Runge-Kutta methods, we describe here an alternative higher order method which offers great stability and accuracy thus allowing to follow the dynamical evolution up to very long times.

Upon time integration of the Schrödinger Equation, we get a closed form for the exact time evolution of an initial quantum state $|\Psi(0)\rangle$

$$|\Psi(t)\rangle = e^{-i\mathcal{H}\,t}|\Psi(0)\rangle, \tag{6.1.2}$$

where the exponential unitary evolution of the Hamiltonian operator manifests itself. At each time, we can make an evolution for a time step Δt by considering a truncated Taylor expansion of the unitary evolution:

$$|\Psi(t+\Delta t)\rangle = e^{-i\mathcal{H}\,\Delta t}|\Psi(t)\rangle \simeq \sum_{k=0,k_{max}} \frac{(-i\Delta t)^k}{k!}\mathcal{H}^k|\Psi(t)\rangle. \tag{6.1.3}$$

Here, the series converges very quickly with k and the cutoff k_{max} must be chosen to obtain the desirable convergence for a given Δt. Therefore, the evolved wave function $|\Psi(t+\Delta t)\rangle$ can be easily obtained by summing terms that can be in turn recovered by repeatedly applying the Hamiltonian $\mathcal{H}$ to $|\Psi(t)\rangle$. The full time evolution at long times can be achieved by subsequent small-time evolutions.

Moreover, time-dependent correlation functions of the form $\mathcal{C}_A(t) = \langle\Psi|A^\dagger(t)A(0)|\Psi\rangle$, where $\mathcal{A}$ is an arbitrary operator, can be as well obtained by first applying A to $|\Psi\rangle$, then performing the time evolution $|\Psi_A(t)\rangle = e^{-i\mathcal{H}\,t}A|\Psi\rangle$, and finally computing $\mathcal{C}_A(t) = \langle\Psi(t)|A^\dagger|\Psi_A(t)\rangle$, where $|\Psi(t)\rangle = e^{-i\mathcal{H}\,t}|\Psi\rangle$.

The numerical accuracy of the unitary evolution can be verified by checking the conserved quantities of the time-evolution (for example the total energy) which in our calculations remain to all purposes constant up to the longest considered evolution times.

6.1.2 Time-Evolving Block Decimation

The general idea of the Time-Evolving Block decimation algorithm [145, 147] is to consider a particular representation of a generic many-body state defined in a Hilbert space of dimension $\mathcal{D}^N$, where $\mathcal{D}$ is the dimension of a certain local-basis. Such a generic state is fully described in terms of the local quantum numbers i_k as

$$|\Psi\rangle = \sum_{i=1}^{\mathcal{D}} c_{i_1 i_2 .. i_N}|i_1, i_2, .., i_{N-1}, i_N\rangle,$$

and in the Vidal's representation the coefficients $c_{i_1 i_2 .. i_N}$ are taken to be

$$c_{i_1 i_2 .. i_N} = \sum_{\alpha_0,..,\alpha_N}^{\chi} \lambda^{[1]}_{\alpha_0}\Gamma^{[1]i_1}_{\alpha_0\alpha_1}\lambda^{[2]}_{\alpha_1}\Gamma^{[2]i_2}_{\alpha_1\alpha_2}\lambda^{[3]}_{\alpha_2}\Gamma^{[3]i_3}_{\alpha_2\alpha_3}\lambda^{[4]}_{\alpha_3}\cdot .. \cdot \lambda^{[N]}_{\alpha_{N-1}}\Gamma^{[N]i_N}_{\alpha_{N-1}\alpha_N}\lambda^{[N+1]}_{\alpha_N}, \tag{6.1.4}$$

where the local tensors Γ and the *bond* matrices λ constitute a set of $\mathcal{D}\chi^2 N + \chi\,(N+1)$ parameters that specify the state in this representation. The time evolution of a given initial state is obtained upon considering a small time-step Δt, and a repeated application of the real-time propagator $e^{-i\mathcal{H}\Delta t}$ within a Suzuki-Trotter approximation scheme, inducing systematic errors of magnitude $\mathcal{O}\left(\Delta t^3\right)$. When the infinitesimal unitary evolution is applied the decomposition (6.1.4) is consistently updated. The other major and most limiting source of systematic errors is however intrinsically due to the finite amount of entanglement retained by Vidal's representation. It can be indeed shown that the total truncation error is exponentially growing with time and it therefore severely limits the accessible time scales. Upon varying the bond dimensionality χ a control of this systematic error can be achieved, even though other computational limitations coming from the general scaling of the algorithm, which is of $\mathcal{O}(\mathcal{D}^4\chi^3)$, have to be faced.

6.1.3 Lanczos Basis

The Lanczos method [79] is a general and very important strategy to recursively generate a basis in which a given Hamiltonian takes a tridiagonal form. This method and its variants are typically used to study the spectrum of a sparse Hamiltonian matrix, to which its application is particularly tailored. Moreover, the particular tridiagonal form of the Hamiltonian can be also used to provide a sometimes faster convergent expansion of the short-time propagator than the Taylor expansion of Eq. (6.1.3).

The Lanczos basis is characterized by a set of orthonormal states $|0\rangle, |1\rangle, \ldots |L\rangle$ in which the full Hamiltonian takes a reduced tridiagonal form:

$$\mathcal{H}_L = \begin{pmatrix} \epsilon_0 & t_{0\to1} & 0 & \vdots & 0 \\ t_{1\to0} & \epsilon_1 & t_{1\to2} & \vdots & 0 \\ 0 & t_{2\to1} & \epsilon_2 & \vdots & 0 \\ 0 & 0 & \ldots & \ddots & t_{L-1\to L} \\ 0 & 0 & \ldots & t_{L\to L-1} & \epsilon_L \end{pmatrix} \tag{6.1.5}$$

The basis set is constructed in a recursive way starting from an initial vector $|0\rangle$ upon repeatedly applying the Hamiltonian

$$t_{n\to n+1}\,|n+1\rangle = \mathcal{H}\,|n\rangle - \epsilon_n\,|n\rangle - t_{n-1\to n}\,|n-1\rangle\,, \tag{6.1.6}$$

with the coefficients of the tridiagonal matrix given by

$$t_{n\to n+1} = \langle n+1|\,\mathcal{H}\,|n\rangle \tag{6.1.7}$$
$$\epsilon_n = \langle n|\,\mathcal{H}\,|n\rangle\,.$$

For sparse matrices, the recursive calculation of the Lanczos elements is eased by the local structure of the Hamiltonian operator, for which a number of operations *linear* in the size of the Hilbert space is required.

When the initial state vector is $|\Psi(t)\rangle$, the evolved state at a given time, then the unitary evolution for a time step Δt reads [83]

$$|\Psi(t+\Delta t)\rangle \simeq \mathcal{V}_L(t)e^{-i\Delta t\mathcal{H}_L(t)}\mathcal{V}_L^T(t)|\Psi(t)\rangle, \tag{6.1.8}$$

where $\mathcal{V}_L(t)$ is the matrix containing all the Lanczos vectors and the exponential of the tridiagonal matrix is considered. This approach therefore constitutes a viable alternative to the bare Taylor expansion previously introduced, even though a satisfactory error control can be achieved with both methods. The Taylor expansion is nonetheless more straightforward to be numerically implemented and it has been the preferred method for our studies.

However, we have considered an alternative use of the Lanczos method in order to characterize the ergodic properties of the dynamics. Indeed, once for an initial many-body state $|0\rangle$ the tridiagonal matrix is constructed we are in condition to consider a time-dependent problem of a particle initially localized on site $|0\rangle$ whose dynamics is governed by $\mathcal{H}_L$. This mapping is particularly useful, as it will be shown later, to quantitatively characterize the many body diffusion (or its lack) in the Hilbert space by means of a simple one particle problem.

Deferring the reader to the application of this method to a later part of the Chapter, we make however a final important remark concerning the practical numerical evaluation of the Lanczos states. Indeed when the tridiagonal matrix elements have to be computed on calculators with a finite-precision arithmetic an extremely careful treatment of numerical truncation errors has to be envisaged. Truncation errors are due to the finiteness of the numerical representation of rational numbers on any calculator and do generally propagate in any arithmetic operation performed. The error accumulation can indeed quickly lead the most recently generated Lanczos vector not to be orthogonal to the previously generated ones and possibly yields spurious results for the eigenvalues and eigenvectors of the Hamiltonian. This is commonly know as the “ghost eigenvalues” problem. To overcome this problem, we have carefully analyzed the dependence of the results on the machine precision, considering up to 10^4 bits of floating point arithmetic, for which no significant truncation error manifests up to the largest value of the Lanczos basis dimension ($L \sim 5000$) we have considered. A normal calculation with standard double precision arithmetic is instead strongly biased by the ghost eigenvalues and leads to wrong results.

6.2 The Bose-Hubbard Model

The validity and the limitations of the ergodicity axiom for quantum matter is currently attracting great interest, [109, 105] since well controlled realizations of closed quantum systems have become feasible upon trapping cold atomic species. [21] Indeed, the evolution of the experimental techniques has led to the possibility to prepare atoms in a given initial state and probe their time evolution under a Hamiltonian whose parameters are fully under control. It is therefore for the first time in the history of physics that we are given the opportunity to directly monitor the ergodicity principle at work in the quantum realm. [146]

One of the simplest models that can be realized in experiments is the Bose-Hubbard Hamiltonian: [21, 70]

$$\mathcal{H} = -J \sum_{\langle i,j \rangle} \left(b_i^\dagger b_j + \text{h.c.} \right) + \frac{U}{2} \sum_i n_i (n_i - 1), \tag{6.2.1}$$

characterized by the amplitude J for an atomic bosonic species to hop between nearest-neighboring wells of an optical lattice and by a *local* repulsion U among atoms localized in the same potential well. The operators $b_i^\dagger$ and b_i create and destroy, respectively, a boson on site i, and $n_i = b_i^\dagger b_i$ is the density operator. [1] Experiments are often performed with anisotropic lattices that realize a collection of almost uncoupled chains, a fortunate case for numerical simulations that we shall mainly consider hereafter.

In one dimension, obstacles to ergodicity can arise in integrable models. [26] However, the Hamiltonian (6.2.1) is not integrable and there are evidences that its dynamical evolution succeeds in fast relaxing to a *thermal* state. In the experiment reported in Ref. [142], a system of ^{87}Rb atoms well described by the Hamiltonian (6.2.1) is prepared in a state in which the sites of the optical lattice are alternatively empty and singly occupied. [142] This state is let evolve with the Hamiltonian (6.2.1) for several ratios U/J. Even at the largest value $U/J \simeq 10$, the initial density profile $(\dots 1, 0, 1, 0, \dots)$ rapidly relaxes to the homogeneous *thermal* one $(\dots \frac{1}{2}, \frac{1}{2}, \frac{1}{2}, \frac{1}{2}, \dots)$, much faster than the integrable counterparts of non-interacting or infinitely-interacting (i.e., hard-core) bosons and consistently with the increased number of relaxation channels that opens once integrability is lost.

When the number of bosons is multiple of the number of sites, the Hamiltonian (6.2.1) is known to describe a Mott insulator for sufficiently large U/J, whereas for small values the system is superfluid. In the gapless phase next to the Mott transition, we may expect that low-energy itinerant Bogoliubov modes coexist with high-energy incoherent excitations. It is well possible that the former relax much faster than the latter, so that the overall relaxation is controlled just by the concentration of the high-energy incoherent excitations stored in the initial state. For densities $n \leq 1$ and $U/J \gg 1$, one may roughly identify those excitations as sites that

---

[1] In the experimental setup, an additional confining potential is usually present. We do not expect the latter to play a major role in what we shall discuss.

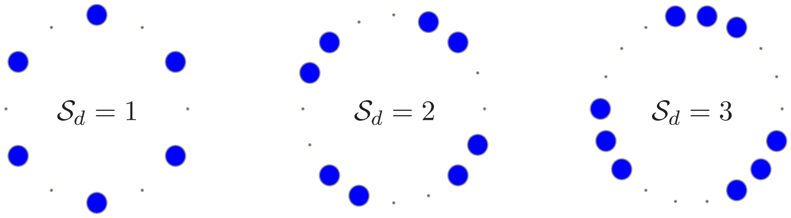

Fig. 6.3.1 Inhomogeneous initial states constituted by clusters of doubly occupied sites (large blue circles) and empty sites (small dots). The size of each cluster is denoted by $\mathcal{S}_d$.

are occupied by two or more bosons. From this perspective, the initial state in the experiment of Ref. [142] is not the best choice for probing how high-energy excitations contribute to the relaxation. Here, we shall consider different initial states that instead include a finite density of high-energy excitations, and simulate their time evolution by means of numerical tools such as exact diagonalization, the Lanczos method and the time-evolving block decimation [145] previously introduced.

6.3 Inhomogeneous Initial States and Dynamical Localization

We start from analyzing the model at density $n = 1$, when at equilibrium a Mott transition occurs at a critical $(U/J)_c \simeq 3.5$. [78] We imagine to prepare an initial state where all the sites are either empty or doubly occupied. In particular we consider the states depicted in Fig. 6.3.1, namely with clusters of doubly occupied sites of variable size $\mathcal{S}_d$. These states are let evolve with the spatially homogeneous Hamiltonian (6.2.1) for different U/J, below and above the critical value. While for small U/J the density profile rapidly reaches the equilibrium configuration $(\dots 1, 1, 1, 1, \dots)$, for large U/J, it stays close to its initial value for a remarkably long time. Eventually, since the system is finite, the density profile approaches the homogeneous plateau, with small residual oscillations that get damped as the system size increases.

We can define a relaxation time τ_R (whose inverse is shown in Fig. 6.3.2, for $\mathcal{S}_d = 1$), as the first time for which the local density approaches its homogeneous value. We highlight that τ_R, at a specific $(U/J)_c^{dyn}$, has a sudden step up, which becomes sharper and sharper as the system size increases. The above results show that above $(U/J)_c^{dyn}$ the system has the tendency to stay dynamically trapped into long-lived inhomogeneous configurations.

For large values of U/J, we can better understand this surprising behavior by means of an effective Hamiltonian that can be derived following the same reasoning of Refs. [101, 113]. For a sufficiently large interaction, it is justified to project the evolution onto states with the same potential energy per site $U/2$, at least for time scales shorter than U^2/J^3. One realizes that states with the same potential energy but with triply and singly occupied sites start to contribute only at order J^4/U^3, so that, with accuracy J^2/U, the number of doubly occupied

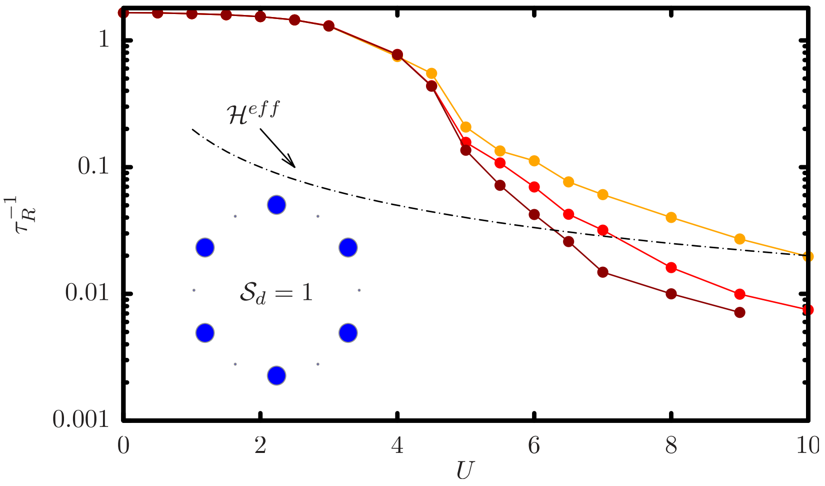

Fig. 6.3.2 Inverse relaxation times τ_R^{-1} of the local density for the initial state $(\ldots 2, 0, 2, 0, \ldots)$. Exact diagonalization results with darker points marking larger systems, respectively $N = 8$, 10 and 12. The dashed line sets the corresponding inverse decay times calculated within the dynamics obtained from the effective Hamiltonian of Eq. (6.3.1).

sites is conserved. If we associate a fictitious spin up or down to a doublon (doubly occupied site) or a holon (empty site), respectively, we find that the effective Hamiltonian that controls the evolution reads:

$$\mathcal{H}^{eff} = \frac{2J^2}{U} \sum_{\langle ij \rangle} \left[-8\, S_i^z\, S_j^z + \left(S_i^+\, S_j^- + S_i^-\, S_j^+ \right) \right], \tag{6.3.1}$$

which describes a hard-axis ferromagnetic Heisenberg model. [101] In Fig. 6.3.3, we show the time-dependence of the clusters density in the large U regime, evolved according to the effective Hamiltonian (6.3.1). Remarkably we see that, even for very small clusters, the system fails to restore the spatial homogeneity up to very long time scales, which turns to be far beyond those currently accessible in typical experimental setups.

To understand the slowing down of the dynamics in this framework we notice that the effective interaction among doublons turns to be *attractive*. This fact, together with the finite density of high energy excitations in the initial state, makes the decay of locally ferromagnetic clusters very unlikely and it is responsible for the effective lack of ergodicity on extremely long time scales. Indeed we have checked that in the large U regime the system has the tendency to get dynamically stuck into clusters of doublons of finite size, whereas a much faster annihilation and recombination rate is observed in the small U limit.

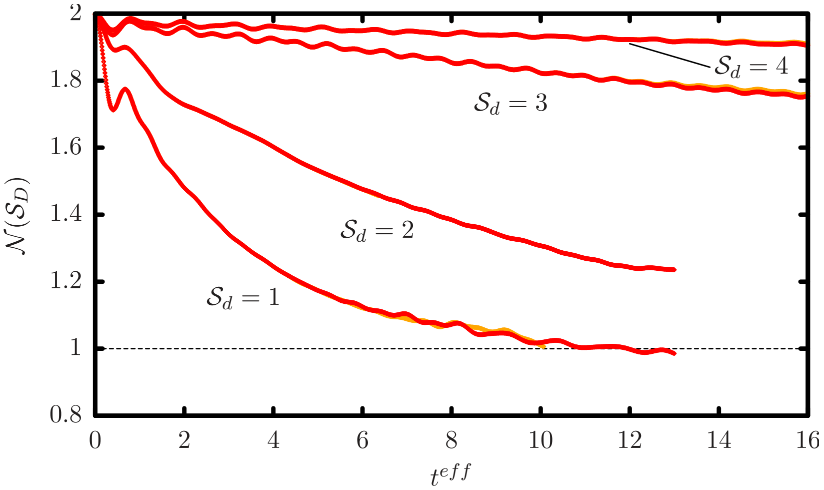

Fig. 6.3.3 Effective-Hamiltonian evolution of the average density within a cluster of different size $\mathcal{S}_d$, where the dimensionless time is defined as $t^{eff} = \frac{2J^2}{U}t$. We show results for $N = 72$ and 96 sites, obtained by the time-evolving block decimation technique. [147] We note that even small clusters of doubly occupied sites can effectively freeze the dynamical evolution in the large-U regime.

6.3.1 Lanczos-Basis Analysis

To get further insights into the dynamical behavior of the system, we recast the problem in a different language. Starting from the initial state, denoted as $|0\rangle$, we can generate an orthogonal basis set $|i\rangle$, $i = 0, 1, \ldots$, by repeatedly applying the Hamiltonian. In this Lanczos basis of many-body wave functions, the Hamiltonian has the form of a tight-binding model on a semi-infinite chain. Each site $i = 0, 1, \ldots$ corresponds to a many-body state, it has an on-site energy $\epsilon_i = \langle i|\mathcal{H}|i\rangle$ and is coupled only to its nearest neighbors by hopping elements $t_{i\to i+1}$ and $t_{i\to i-1}$. [79] It is easy to realize that the unitary evolution of the original many body problem is thus fully equivalent to the dynamics of a single particle, initially sitting at site 0, that is then let propagate along such a tight-binding chain of many-body states. We note that, both ϵ_i and $t_{i\to i+1}$ largely fluctuate from site to site, therefore resembling an effective Anderson model, even though those parameters are in reality deterministic, see Fig. 6.3.4. In Figure 6.3.5, we also show the mean distance traveled by the particle after time t starting from the first site of the chain, which corresponds to an initial state $|0\rangle \equiv (\ldots 2, 0, 2, 0, \ldots)$, and for different U/J. We observe that, for small values of U/J, the particle diffuses and its wave-packet finally spreads over the whole chain, in a rather uniform way. On the contrary, above a certain critical value of the interaction $(U/J)_c^{dyn}$, the particle stays localized near the origin for arbitrarily long times.

A closer look to the structure of the on site energies reveal the existence of a potential well at the edge of the chain. This is crucial in order to understand the observed localization transition. Since the potential well cannot induce a true bound state below the bottom of the spectrum, at most a resonance will form in the spectrum, from which the particle could in principle escape in a finite time. This indeed happens at small U but apparently not at large U, where the increased depth of the well and the effective randomness of the on-site energies conspire together to keep the particle localized close to the edge, preventing the the states in the well to hybridize with other states along the chain. We now see how this result connects with the previous analysis on the density relaxation times. In the small U/J regime the particle is able to escape from the well and to explore larger portions of the chain, thus resulting into a fast density relaxation. As opposite, for large U/J, the particle bounces back and forth inside the well, finding hard time to escape from it. This lack of diffusion results into a very long-time scale for the density to relax to its homogeneous value.

The above results show explicitly that some kind of localization in the many-body configurational space does occur, at least in the finite system. [9, 27] While such an intriguing behavior might well be a subtle effect due to the finite size spectrum, it could also signal the onset of a genuine localization that survives in the thermodynamic limit.

6.3.2 Lanczos-Basis Analysis of an Integrable Model

To better elucidate the many-body localization phenomenon suggested by the Lanczos-basis analysis of the Bose-Hubbard model, we hereby show that localization is *not* strictly implied by integrability. To this purpose, we consider a model of one-dimensional hard-core bosons prepared in an initial inhomogeneous state with an alternating density profile $(\dots 1, 0, 1, 0, \dots)$ and let it evolve in the Lanczos basis with their non-interacting (integrable) kinetic Hamiltonian. In Fig. 6.3.6, we show both the Lanczos hopping elements and the expectation value of

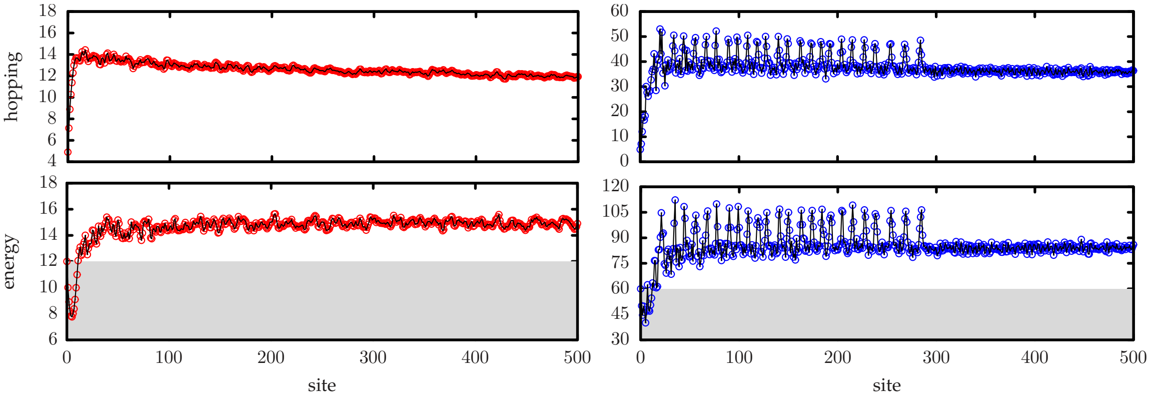

Fig. 6.3.4 On site energies and nearest-neighbor hoppings of the effective chain that represents the Hamiltonian in the Lanczos basis starting from the state $(\dots, 2, 0, 2, 0, \dots)$, the site 0. Red points refer to $U = 2J$, when the particle does diffuse starting from site 0, while blue points to $U = 10J$, when it does not. The shaded regions correspond to energies less or equal that of the initial state.

the Lanczos particle traveling in the many-body space. The effect of integrability is to reduce the number of allowed Lanczos states with respect to the total Hilbert space. Indeed, we find that the hopping is a strongly decreasing function of the iterations, approaching zero after a certain number of states $\nu(N)$ that is a finite fraction of the full Hilbert space. Noticeably, the average position traveled by the particle increases accordingly, leading, therefore, to a full delocalization in the thermodynamic limit. This analysis shows that a localization in the Lanczos basis is not necessarily due to integrability – whose effect only amounts to reduce the number of active many-body states – whereas it is due to the effective dynamical constraints brought by the interaction.

6.3.3 Inhomogeneous States Dynamics at $\mathrm{n} = 2/3$

Until now, we have concentrated our attention on the unitary-filling density, where at equilibrium a Mott transition takes place upon increasing the interaction strength. To better realize the importance of the density on our considerations on the large-U relaxation times, we now show the exact time evolution of inhomogeneous states at $n < 1$. For example, we consider $n = 2/3$ and an initial density profile $(\dots 2, 0, 0, 2, 0, 0, \dots)$. As shown in Fig. 6.3.7, we find quite a different behavior for the density relaxation times with respect to the unitary-filling case, with a much smoother crossover from small to large values of U_f. Moreover, there is no evidence of any increase in the relaxation times with the system size. This fact suggests that the dynamical constraints brought by the effective interaction among doublons are much stronger

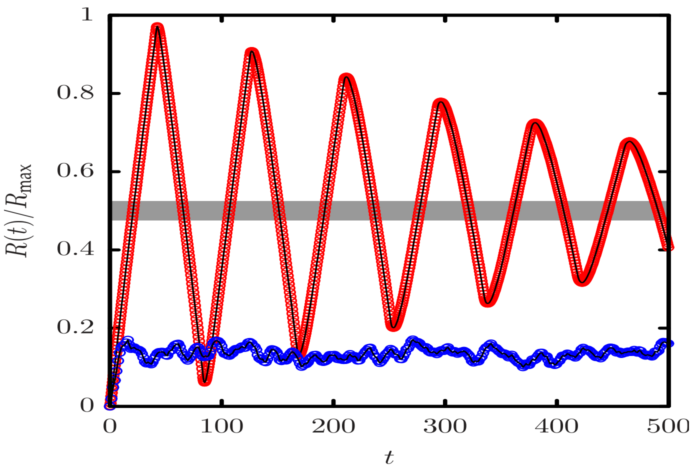

Fig. 6.3.5 Time-dependent expectation value of the wave-packet position of the effective particle traveling in the Hilbert space generated by a chain of $R_{\max} = 1000$ Lanczos states. The red points correspond to $U = 2J$ and the blue points to $U = 10J$ (the original lattice size of the Bose-Hubbard model is $N = 12$). The shaded region marks the center of the Lanczos chain, which is not reached in the localized regime.

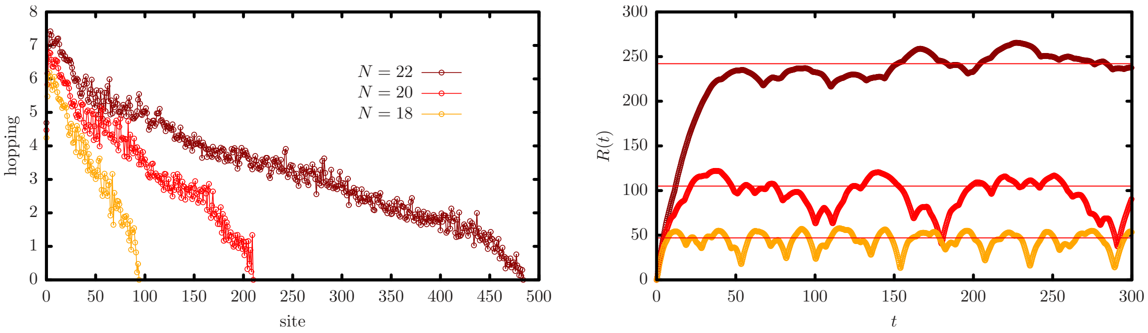

Fig. 6.3.6 *Left panel* – Nearest neighbor hopping of the effective chain that represents the non-interacting hard-core bosons Hamiltonian in the Lanczos basis starting from $(\ldots 1, 0, 1, 0, \ldots)$ ***Right panel*** – Time-dependent expectation value of the wave-packet position traveling in the Hilbert space generated by a chain of $\nu(N)$ Lanczos states. The horizontal lines correspond to $\nu(N)/2$ and show that delocalization takes place.

at $n = 1$, where a sharp crossover in the relaxation times is observed. We finally remark that, even at non unitary fillings, we expect larger clusters of doublons to have larger relaxation times than the simple initial state we have considered here. The possibility of a non-thermal behavior at non-unitary filling cannot be excluded, even though the strongest manifestation of the dynamical arrest is expected to happen at $n = 1$. This fact suggests a deeper connection between the observed dynamical behavior and the zero temperature Mott transition that occurs at equilibrium and at integer filling, as suggested by calculations with infinite-coordination lattices. [119, 123]

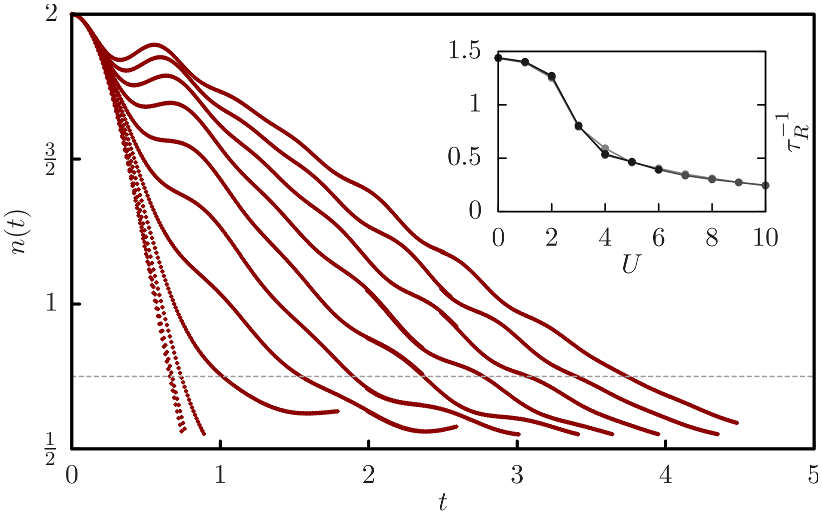

Fig. 6.3.7 Exact time evolution of the densities on initially doubly occupied sites at filling $n = 2/3$ for an $N = 15$ chain. Different curves from left to right correspond to increasing values of the final interaction at $U/J = 0, 1, \ldots 10$. Inset: corresponding inverse relaxation times τ_R^{-1} for increasing lattice size $N = 9$, 12, and 15.

6.4 Homogeneous Initial States and Quantum Quenches

In light of the previous results, one may question that by choosing an inhomogeneous configuration of doublons we pick up a rather specific initial state in the Hilbert space. We are now going to show that the above findings strongly affect the dynamics starting from a perfectly homogeneous state. In this respect, a particularly interesting class of initial states are the ground states of $\mathcal{H}$ for given values of the interaction U_i, which are let evolve under the Hamiltonian dynamics after a sudden increase of the interaction to a final value $U_f > U_i$, the so-called quantum quench. Kollath and coworkers [76] reported evidence for the existence of two separated regimes in which either thermal or non-thermal behavior is observed for local observables. The origin of the non-thermal behavior in the large U_f region and the possibility of an ergodicity breaking in the thermodynamic limit is still highly debated [116, 18].

In the following, we focus on an average density $n = 1$ and we show that signatures of long lived metastable states of doublons can be identified in the dynamics after a quantum quench. At variance with the previous numerical experiments, now both the initial state and the quantum Hamiltonian do preserve the spatial homogeneity and, therefore, the quest for possible signatures of ergodicity breaking requires a different approach. Since we have identified density relaxation as the slowest process in the problem, we monitor the dynamics of the system by measuring the auto-correlation of the density averaged over all sites, namely through

$$\mathcal{C}(t) = \frac{1}{N}\sum_i \langle n_i(t) n_i(0)\rangle - \langle n_i(t)\rangle \langle n_i(0)\rangle \, . \tag{6.4.1}$$

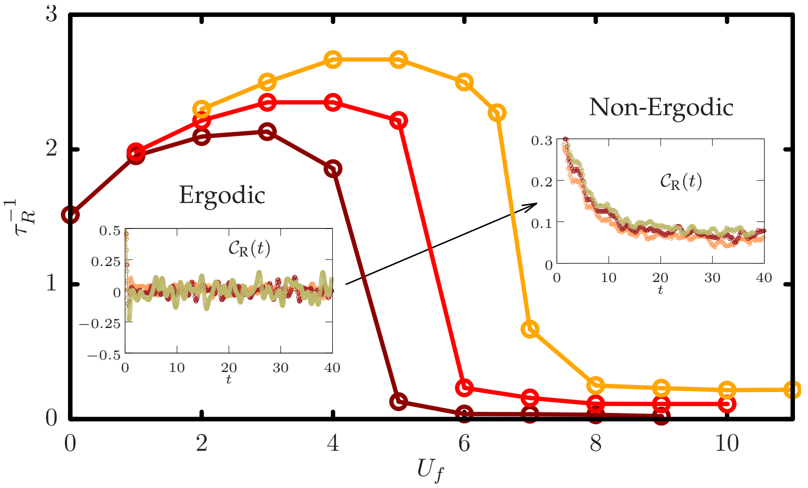

Fig. 6.4.1 Inverse relaxation times of density excitations in the homogeneous system, see Eq. (6.4.1). From left to right, different curves correspond to different initial states at $U_i/J = 0$, 1, and 2. Insets: real part of the density correlations $\mathcal{C}(t)$ in the ergodic and in the non-ergodic region. Data are obtained with exact-diagonalization on a lattice with $N = 12$.

For any finite size system, due to the homogeneity of both the initial and the quantum evolution, $\mathcal{C}(t)$ must have a vanishing long-time average. Indeed, as shown in Fig. 6.4.1, for small $U_f \ll U_i$ this quantity has a very fast transient to zero. On the contrary, for $U_f \gg U_i$ the density auto-correlation $\mathcal{C}(t)$ gets stuck into a long-lived finite value plateau $\mathcal{C}_\star \neq 0$, before approaching zero only on a much longer time scale. If we extract a relaxation time from $\mathcal{C}(t)$, we find a similar behavior as in Fig. 6.3.2, i.e., a dramatic increase of the relaxation times above a threshold value of the final interaction strength.

In agreement with the previous analysis, the appearance of such a long-lived metastable state characterized by a finite plateau $\mathcal{C}_\star$ of the density auto-correlation function might indicate an excess of double occupancies that have no channel to relax. In other words, the dynamical constraints brought by the interaction severely slow down density excitations, whose characteristic time scales increase abruptly after a critical threshold. The main phenomenological traits of this *dynamical arrest* characterized by long-lived inhomogeneous states closely remind the physics of glassy materials.

6.5 Discussion

In conclusion, we have found that the dynamical constraints brought by a strong interaction can trap the evolution of repulsive bosons hopping on a lattice into metastable states that lack translational symmetry, provided that the energy stored into the initial state is above a threshold. We pointed out that a self-induced effective attraction among doublons is one of the major processes that can effectively freeze the dynamics on long time scales. Such a mechanism is recognized to play a role in the density relaxation processes of purely homogeneous systems through a dynamical arrest visible in time-dependent density correlations. The main features of this intriguing behavior, namely the slowing down of density excitations and the long-lived inhomogeneous pattern, resembles closely a kind of glass transition.

Moreover, we have shown that the time evolution of the many-body problem can be mapped onto that of a particle moving from the edge of a semi-infinite tight-binding chain with nearest-neighbor hopping, where each site represents a many-body wave function. This model looks like an Anderson model, since both the on-site energy and the hopping vary from site to site, with a potential well at one edge due to the high-energy content of the initial state. Interestingly, we find a delocalization-localization transition in this problem, with the particle being unable to diffuse on the whole chain above a certain value of the well depth. We consider this analogy quite suggestive and potentially constitutes an even stronger indication of ergodicity breaking in the many-body space which is worth to be further investigated.

Chapter 7

Time-Dependent Variational Monte Carlo

Non-Thermal Behavior of the Bose-Hubbard Model After a Quench

Since the early days of quantum mechanics, variational methods have played a central role in the progress of our understanding of the ground-state properties of many body interacting systems. The variational principle in quantum mechanics indeed often allows to validate or disprove the physical description encoded in a particular functional form of the ground-state wave-function. Due to their physical appeal and their intrinsic non perturbative nature, variational methods are still largely used, either with further analytical (mean-field like) approximations or in connection with very efficient numerical algorithms to optimize the wavefunction.[128, 143] Indeed, our ability to describe ground-state properties of strongly correlated systems has largely increased thanks to the possibility to consider improved correlated wave-functions with a large number of variational parameters. The role of Monte Carlo methods has been of particularly relevant for this program to be realized. Indeed, the very nature of correlated wave functions and their intrinsically many body structure do not allow for an analytical treatment of the variational problem. Since the early works by McMillan[87] it has soon recognized the natural connection between the square modulus of a given wave function with a probability density in the many-body configurational space that could be sampled by means of stochastic methods.

The extension of those successful ideas to the dynamics of strongly correlated systems is a natural goal to be pursued which has however not found until now a decisive advancement. Indeed, in recent years mean-field-like variational methods have been developed and largely applied to the real-time dynamics of correlated bosonic systems, mainly in the spirit of the simple Gutzwiller approximation.[88, 119] Although they may capture some general physical features, they are known to miss crucial ingredients such as damping and relaxation due to quantum interference effects. The extension of these methods to time-dependent correlated wave-functions is therefore an essential requirement for the advancement of our understanding of quantum dynamics as much as it has been with the introduction of correlated wave-functions for ground-state properties.

In this Chapter we show that the out-of-equilibrium properties of a closed quantum systems can be accurately described by means of a time-dependent variational scheme supported by a very general class of wave-functions.[32] The functional form of the wave-function is presented and justified in 7.1. In particular, we show that the exact dynamics of a quantum system can be mapped onto an instantaneous ground-state problem. This ground-state problem is in turn shown to be well approximated, in appropriate circumstances, by a specific generalization of the Jastrow factors. In 7.2 we complete the description of the scheme upon introducing the variational equations of motion for the wave-function parameters and underlying the essential role of Monte Carlo methods in their solution. The scheme we introduce here is applicable to systems of arbitrary dimensionality and does not suffer from the limitations arising in renormalization-based methods that have been discussed in the previous Chapter.

In the last part of the Chapter we present a specific application of the method to the previously introduce problem of the quantum quenches in the Bose Hubbard model, showing that canonical thermalization is not achieved in the large interaction quench regime. By means of the physical insight offered by the variational wave function we further show that this lack of thermalization can be explained in terms of long-lasting metastability of density inhomogeneities, therefore providing a further consistency check for the previously discussed phenomenological issues.

7.1 Time-Dependent Ground states

When a system is driven out of equilibrium, at each time its wave-function evolves under the action of the unitary evolution induced by its Hamiltonian $\mathcal{H}$. In particular, without loss of generality, we can imagine that the initial quantum state $\Phi(t=0)$ coincides with the ground state of a given Hamiltonian $\overline{\mathcal{H}}(t=0)$. Under reasonable assumptions of smoothness of the evolution, at *each* time the exactly evolved wave-function $\Phi(t)=e^{-i\mathcal{H}t}\Phi(t=0)$ can be in turn identified with the ground state of an auxiliary time-dependent Hamiltonian

$$\overline{\mathcal{H}}(t)=\mathcal{H}+\mathcal{V}(t), \tag{7.1.1}$$

where $\mathcal{V}(t)$ is a complex-valued time-dependent operator which is generally unknown. We also introduce the instantaneous eigenstates of $\overline{\mathcal{H}}(t)$, namely $\overline{\psi}_k(t)$ with energies $\overline{E}_k(t)$. In general, apart from possible representability issues, it is always possible to choose $\mathcal{V}(t)$ in such a way that the instantaneous ground state of $\overline{\mathcal{H}}(t)$ corresponds to the exactly evolved state $\Phi(t)$ as obtained by the unitary Schrödinger evolution. Therefore, at $t=0$ by construction $\overline{\psi}_0(t=0)\equiv\Phi(t=0)$ is just the known ground state of the initial Hamiltonian.

Even though the operator $\mathcal{V}(t)$ is generally unknown at an arbitrary time, we can nonetheless ask ourselves whether its time evolution can be determined. The problem to be addressed is therefore to identify the equations of motion for $\mathcal{V}(t)$ that determines the correct evolution. To this end, we consider the ground state of $\overline{\mathcal{H}}(t+\epsilon)$ due to an infinitesimal change of the unknown time-dependent "potential". This ground state, according to first-order perturbation theory is given by

$$\overline{\psi}_0(\mathbf{x},t+\epsilon)=\overline{\psi}_0(\mathbf{x},t)+\epsilon\sum_{k\neq 0}\frac{\langle\overline{\psi}_k(t)|\,\dot{\mathcal{V}}(t)\,|\overline{\psi}_0(t)\rangle}{\overline{E}_0(t)-\overline{E}_k(t)}\overline{\psi}_k(\mathbf{x},t)+\mathcal{O}(\epsilon^2), \tag{7.1.2}$$

and it is therefore due to the small perturbation $\mathcal{V}(t+\epsilon)-\mathcal{V}(t)=\epsilon\dot{\mathcal{V}}(t)+\mathcal{O}(\epsilon^2)$. The above equation contains the instantaneous excited states of the auxiliary Hamiltonian. Even though such excited states are generally unknown, it is generally possible to write them in terms of some "excitation operators" in the spirit of Feynman construction. An assumption that we do at this stage is that the instantaneous excited-states of $\overline{\mathcal{H}}(t)$ can be written in terms of some local excitation operators $\mathcal{O}_k(x)$, in such a way that

$$\overline{\psi}_k(\mathbf{x},t)\simeq\frac{\delta\mathcal{O}_k(x)}{\mathcal{N}_k}\overline{\psi}_0(\mathbf{x},t), \tag{7.1.3}$$

where $\delta\mathcal{O}_k(x) = \mathcal{O}_k(x) - \langle\mathcal{O}_k\rangle$. The presence of the ground-state expectation values fluctuations guarantees the orthogonality condition $\langle\overline{\psi}_k \,|\overline{\psi}_0\rangle = 0$, whereas the quantities $\mathcal{N}_k^2 = \langle\mathcal{O}_k\mathcal{O}_k\rangle - \langle\mathcal{O}_k\rangle^2$ guarantee that the eigenstates are properly normalized.

Notice that the chosen expression for the excited states, Eq. (7.1.3), does assume that the excitation operators are time-independent. This assumption is, in general, well justified on physical grounds whenever the dynamics of the system is characterized by a well defined set of low-energy excitations. Such low-energy excitations are however not necessarily low-energy excitations of the full Hamiltonian $\mathcal{H}$ but of the auxiliary Hamiltonian $\overline{\mathcal{H}}(t)$. Therefore we do not require the dynamics of the system to be confined in the low energy manifold of the full Hamiltonian, which would otherwise be a restrictive limitations for the study of the dynamics far from equilibrium.

Within this assumption, we are now in position to rewrite the perturbed ground state at time $t+\epsilon$ as

$$\overline{\psi}_0(\mathbf{x}, t+\epsilon) = \overline{\psi}_0(\mathbf{x}, t)\left[1 + \epsilon\sum_{k\neq 0}\frac{\langle\overline{\psi}_0(t)|\,\delta\mathcal{O}_k\dot{\mathcal{V}}(t)\,|\overline{\psi}_0(t)\rangle}{\left[\overline{E}_0(t) - \overline{E}_k(t)\right]\mathcal{N}_k}\delta\mathcal{O}_k(\mathbf{x})\right] + \mathcal{O}(\epsilon^2), \tag{7.1.4}$$

where the values of the matrix elements $\langle\overline{\psi}_0(t)|\,\delta\mathcal{O}_k\dot{\mathcal{V}}(t)\,|\overline{\psi}_0(t)\rangle$ implicitly contain the time evolution of the auxiliary potential. Defining the unknown quantities

$$\dot{\alpha}_k(t) \equiv \frac{\langle\overline{\psi}_0(t)|\,\delta\mathcal{O}_k\dot{\mathcal{V}}(t)\,|\overline{\psi}_0(t)\rangle}{\left[\overline{E}_0(t) - \overline{E}_k(t)\right]\mathcal{N}_k}, \tag{7.1.5}$$

we immediately notice that the time evolution of the instantaneous ground state is given by

$$\overline{\psi}_0(\mathbf{x}, t+\epsilon) = \overline{\psi}_0(\mathbf{x}, t)\left\{1 + \epsilon\sum_{k\neq 0}\left[\dot{\alpha}_k(t)\right]\delta\mathcal{O}_k(\mathbf{x})\right\} + \mathcal{O}(\epsilon^2), \tag{7.1.6}$$

which corresponds to a time-dependent wave-function of the form

$$\psi(\mathbf{x}; \alpha(t)) = \exp\left\{\sum_k\left[\delta\mathcal{O}_k(\mathbf{x})\right]\alpha_k(t)\right\} \times \Phi(x, t=0). \tag{7.1.7}$$

The above obtained functional form, which relies on the assumption (7.1.3), is a generalized Jastrow factor in which the complex-valued parameters $\alpha_k(t)$ are coupled to the excitation operators.

Equation (7.1.3) also enlightens on the range of validity of the introduced approximation. Namely, if equation (7.1.3) were true, then the inter-orthogonality condition of the eigenstates $\langle\overline{\psi}_k \,|\overline{\psi}_k\rangle = \delta_{k,k'}$ would imply that

$$\langle \mathcal{O}_k \mathcal{O}_{k'} \rangle - \langle \mathcal{O}_k \rangle \langle \mathcal{O}_{k'} \rangle = \delta_{k,k'} \mathcal{N}_k^2, \tag{7.1.8}$$

or, in other words, that off-diagonal fluctuations of these operators are exactly vanishing. Therefore, a measure of the quality of the approximation is given by the magnitude of the off-diagonal elements of the above-defined correlation matrix as a function of time.

7.2 Real-Time Evolution of the Variational Parameters

In order to complete our description of the dynamics in terms of the previously obtained wave-functions, it is crucial to obtain the equations of motion for the set of complex parameters $\alpha_k(t)$. The variational parameters time trajectories $\alpha_k(t)$ that best reproduce the exact quantum dynamics can be found in a number of different ways, all providing different insights into the present time-dependent variational scheme. In the following we show both an optimization argument, based on the minimization of the Hilbert space distance between the approximate and the exact states, and a purely variational argument both leading to the same equations of motion.

7.2.1 Minimal Hilbert Space Distance

Let us consider a time-dependent state of the form

$$\psi(x; \alpha(t)) = \exp\left[\sum_k \mathcal{O}_k(\mathbf{x}) \alpha_k(t)\right], \tag{7.2.1}$$

where $\alpha_k = \alpha_k^R + i\alpha_k^I$ are complex variational parameters coupled to the real local excitation operators $\mathcal{O}_k(\mathbf{x})$. A physical justification for this particular form of the variational wave-function has been given in the previous section and relies on the assumption that the instantaneous eigenstates of $\tilde{H}(t)$ relevant for the dynamics take the “Feynman-like” form (7.1.3). Moreover, for simplicity we also assume in the following that the initial ground state $\varPhi(\mathbf{x}, t = 0)$ has the same exponential form, therefore setting the initial conditions for the parameters $\alpha_k(t = 0)$. This latter assumption is very well verified in all the physical systems we will study but it is not crucial for the applicability of the method.

The exact infinitesimal real-time evolution of $\psi(t)$ is given by

$$\varPhi(\mathbf{x}, t + \epsilon) = \psi(\mathbf{x}; \alpha(t)) \left[1 - i\epsilon \mathcal{E}(\mathbf{x}, \alpha(t)\right], \tag{7.2.2}$$

where $\mathcal{E}(\mathbf{x},\alpha(t)) = \frac{\langle \mathbf{x}|H|\psi(t)\rangle}{\psi(\mathbf{x},t)}$ is the complex-valued "local energy" for a given set of variational parameters and for a given configuration x. An infinitesimal variation of the variational wave-function due to the change of parameters is instead given by

$$\psi(\mathbf{x};\alpha(t+\epsilon)) = \psi(\mathbf{x},\alpha(t)) \left[1 + \epsilon \sum_k \dot{\alpha}_k \mathcal{O}_k(\mathbf{x})\right]. \tag{7.2.3}$$

In order to have the best possible variational description of the real-time dynamics we want to minimize the total rate of departure of the variational state from the exact state, i.e. the Euclidean norm of the first-order differences, namely

$$\varDelta_1^2(t) = \sum_x \left| \frac{d\psi(\mathbf{x},t)}{dt} - \frac{d\varPhi(\mathbf{x},t)}{dt} \right|^2. \tag{7.2.4}$$

The rate of change is conveniently written as an expectation value over the square modulus of the wave-function as

$$\varDelta_1^2(t) = \sum_{\mathbf{x}} |\psi(\mathbf{x};\alpha(t))|^2 \left[Z_1^R(\mathbf{x},t)^2 + Z_1^I(\mathbf{x},t)^2 \right], \tag{7.2.5}$$

where we have introduced the quantities

$$Z_1^R(\mathbf{x},t) = \sum_k \dot{\alpha}_k^R \mathcal{O}_k(\mathbf{x}) - \mathcal{E}^I(\mathbf{x},\alpha(t)) \tag{7.2.6}$$

$$Z_1^I(\mathbf{x},t) = \sum_k \dot{\alpha}_k^I \mathcal{O}_k(\mathbf{x}) + \mathcal{E}^R(\mathbf{x},\alpha(t)). \tag{7.2.7}$$

At a given time, the rate of change is in turn a function of the time derivatives of the variational parameters, $\dot{\alpha}_k(t)$ which we therefore determine imposing that $\varDelta_1^2(t)$ is as small as possible. To this purpose, we look for the solutions of the equations obtained setting the gradient components to zero, which lead to

$$Z_1^R(\mathbf{x},t)\frac{\partial}{\partial_{\dot{\alpha}_k^R}} Z_1^R(\mathbf{x},t) = \left(\sum_{k'} \dot{\alpha}_{k'}^R \mathcal{O}_{k'}(\mathbf{x})\mathcal{O}_k(\mathbf{x})\right) - \mathcal{E}^I(\mathbf{x},\alpha(t))\mathcal{O}_k(\mathbf{x}) \tag{7.2.8}$$

$$Z_1^I(\mathbf{x},t)\frac{\partial}{\partial_{\dot{\alpha}_k^I}} Z_1^I(\mathbf{x},t) = \left(\sum_{k'} \dot{\alpha}_{k'}^I \mathcal{O}_{k'}(\mathbf{x})\mathcal{O}_k(\mathbf{x})\right) + \mathcal{E}^R(\mathbf{x},\alpha(t))\mathcal{O}_k(\mathbf{x}). \tag{7.2.9}$$

The stationary solution that minimizes the variational error then can be found upon explicitly considering the derivatives of the $Z_1(t)$ and read

$$\sum_{k'} \dot{\alpha}^R_{k'} \left\langle O_k O_{k'} \right\rangle = \left\langle \mathcal{E}^I O_k \right\rangle , \tag{7.2.10}$$

$$\sum_{k'} \dot{\alpha}^I_{k'} \left\langle O_k O_{k'} \right\rangle = - \left\langle \mathcal{E}^R O_k \right\rangle , \tag{7.2.11}$$

where the expectation values are summation over the square-modulus measure of the variational wave-function.

An interesting point to be noticed is that the solution of Equations (7.2.10) also guarantees the best possible expectation values of the "observables" $\mathcal{O}_k(\mathbf{x})$ for small propagation times. Indeed, if we consider the difference between the exact and the variational expectation values at order ϵ,

$$\left(\Delta \dot{O}_k\right)(t) = \frac{d}{dt} \left\langle O_k \right\rangle - \frac{d}{dt} \left\langle O_k \right\rangle_{\text{exact}} , \tag{7.2.12}$$

we find that for the optimal solution the condition $\Delta \dot{O}_k(t_0) = 0$ is always verified.

Until now we have neglected the explicit time dependence of the complex phase of the wave-function, which however can be also recovered from the previous equations. Indeed, we now notice that the time-derivative of the phase of the wave-function can be explicitly found considering as an observable $O_\phi = 1$. Thus, factoring the phase of the time-evolved variational state, we have that

$$\psi(\mathbf{x}, t) = e^{\phi(t)} e^{\sum_k O_k(\mathbf{x}) \alpha_k(t)}, \tag{7.2.13}$$

with the optimal values of the time-derivatives given by

$$\sum_{k'} \dot{\alpha}^R_{k'} \left[\left\langle \mathcal{O}_k \mathcal{O}_{k'} \right\rangle - \left\langle \mathcal{O}_k \right\rangle \left\langle \mathcal{O}_{k'} \right\rangle \right] = \left\langle \mathcal{E}^I \mathcal{O}_k \right\rangle \tag{7.2.14}$$

$$\sum_{k'} \dot{\alpha}^I_{k'} \left[\left\langle \mathcal{O}_k \mathcal{O}_{k'} \right\rangle - \left\langle \mathcal{O}_k \right\rangle \left\langle \mathcal{O}_{k'} \right\rangle \right] = - \left\langle \mathcal{E}^R \mathcal{O}_k \right\rangle + E \left\langle \mathcal{O}_k \right\rangle , \tag{7.2.15}$$

while the explicit time-derivatives of the phase factor read

$$\dot{\phi}^R(t) = - \sum_{k'} \dot{\alpha}^R_{k'} \left\langle \mathcal{O}_{k'} \right\rangle \tag{7.2.16}$$

$$\dot{\phi}^I(t) = -E - \sum_{k'} \dot{\alpha}^I_{k'} \left\langle \mathcal{O}_{k'} \right\rangle . \tag{7.2.17}$$

The optimal value of the square-displacement associated with the solution of the equations (7.2.14-7.2.15) is

$$\Delta^2_1(t) = \left\langle H^2 \right\rangle - E^2 - \left[\sum_{k,k'} \left(\dot{\alpha}^R_k \dot{\alpha}^R_{k'} - \dot{\alpha}^I_k \dot{\alpha}^I_{k'} \right) S_{k,k'} \right] , \tag{7.2.18}$$

having introduced the matrix of the fluctuations $S_{k,k'} = \langle \mathcal{O}_k \mathcal{O}_{k'} \rangle - \langle \mathcal{O}_k \rangle \langle \mathcal{O}_{k'} \rangle$ which corresponds to the left hand side of (7.1.8) and it is therefore also a crucial quantity for the validity of the approximation.

7.2.2 Variational Principle

The equations of motion for the wave-function parameters can be also derived from an alternative approach directly based on the variational principle. In order to proceed, we introduce the action

$$\mathcal{S} = \int dt \, \langle \psi | \, i \frac{\partial}{\partial t} - H \, | \psi \rangle \, , \tag{7.2.19}$$

which is a functional of the variational parameters $\alpha_k(t)$. The variational principle states that the stationary solution for the variations of the action determines the optimal set of parameters. The action explicitly reads

$$\mathcal{S} = \int dt \left[\sum_k i \dot{\alpha}_k \langle \mathcal{O}_k \rangle - E(\alpha_k^R, \alpha_k^I) \right] , \tag{7.2.20}$$

where E is the expectation value of the energy on the variational state. We first notice that the action must be real, therefore we must have $\sum_k \dot{\alpha}_k^R \langle \mathcal{O}_k \rangle = 0$, this condition being equivalent to the norm conservation and can be satisfied taking a constant observable associated to the normalization, namely $\mathcal{O}_\phi = 1$ leading to the following time-evolution for the real part of the phase $\dot{\phi}^R = -\sum_k \dot{\alpha}_k^R$, which is completely equivalent to (7.2.17). Therefore the action is

$$\mathcal{S} = -\int dt \left[\sum_k \dot{\alpha}_k^I \langle \mathcal{O}_k \rangle + E(\alpha_k^R, \alpha_k^I) \right] , \tag{7.2.21}$$

and can be minimized with respect to $\langle \mathcal{O}_k \rangle$ leading to

$$\dot{\alpha}_k^I = -\frac{\partial E}{\partial \langle \mathcal{O}_k \rangle}, \tag{7.2.22}$$

moreover by integration by parts we find

$$\mathcal{S} = \int dt \left[\sum_k \langle \dot{\mathcal{O}}_k \rangle \alpha_k^I - E(\alpha_k^R, \alpha_k^I) \right] , \tag{7.2.23}$$

a further minimization of the action with respect to α_k^I then leads to the equations

$$\left\langle \dot{\mathcal{O}}_k \right\rangle = \frac{\partial E}{\partial \alpha_k^I}. \tag{7.2.24}$$

Equations (7.2.22,7.2.24) are completely equivalent to the one found previously, as, concerning Eq. (7.2.24) we have

$$\left\langle \dot{\mathcal{O}}_k \right\rangle = 2\sum_{k'} \dot{\alpha}_{k'}^R \left\langle \mathcal{O}_k \mathcal{O}_{k'} \right\rangle \tag{7.2.25}$$

$$\frac{\partial E}{\partial \alpha_k^I} = 2\left\langle \mathcal{E}^I \mathcal{O}_k \right\rangle. \tag{7.2.26}$$

Concerning Eq. (7.2.22), we have that

$$\frac{\partial E}{\partial \left\langle \mathcal{O}_k \right\rangle} = \sum_{k'} \frac{\partial E}{\partial \alpha_{k'}^R} \frac{\partial \alpha_{k'}^R}{\partial \left\langle \mathcal{O}_k \right\rangle}, \tag{7.2.27}$$

therefore, inverting this relation and pushing it in Eq. (7.2.22) we get

$$\sum_{k'} \dot{\alpha}_{k'}^I \frac{\partial \left\langle \mathcal{O}_k \right\rangle}{\partial \alpha_{k'}^R} = -\frac{\partial E}{\partial \alpha_k^R}, \tag{7.2.28}$$

which is again equivalent to Eq. (7.2.10) as

$$\frac{\partial \left\langle \mathcal{O}_k \right\rangle}{\partial \alpha_{k'}^R} = 2\left\langle \mathcal{O}_k \mathcal{O}_{k'} \right\rangle \tag{7.2.29}$$

$$\frac{\partial E}{\partial \alpha_k^R} = 2\left\langle \mathcal{E}^R \mathcal{O}_k \right\rangle. \tag{7.2.30}$$

7.2.3 Norm and Energy Conservation

The equations introduced define a real-time dynamics of the variational states that preserves both the norm and the energy. This can be verified noticing that the norm

$$N(t) = \sum_{\mathbf{x}} |\psi(\mathbf{x},t)|^2 = \sum_{\mathbf{x}} e^{2\phi^R(t)} e^{2\sum_k \mathcal{O}_k(\mathbf{x})\alpha_k^R(t)}, \tag{7.2.31}$$

is conserved, as

$$\dot{N}(t) = \sum_{\mathbf{x}} \Bigg[\left(\frac{\partial}{\partial \phi^R} e^{2\phi^R(t)} \right) e^{2\sum_{k'} \mathcal{O}_{k'}(\mathbf{x})\alpha_{k'}^R(t)} \dot{\phi}^R + \\ + \sum_k e^{2\phi^R(t)} \frac{\partial}{\partial \alpha_k^R} e^{2\sum_{k'} \mathcal{O}_{k'}(\mathbf{x})\alpha_{k'}^R(t)} \dot{\alpha}_k^R \Bigg], \tag{7.2.32}$$

is equivalent to

$$\dot{N}(t)=\sum_x 2\left|\psi(x,t)\right|^2\left[\dot{\phi}^R+\sum_k \mathcal{O}_k(x)\dot{\alpha}_k^R\right]=0. \tag{7.2.33}$$

Moreover, the time-derivative of the energy reads

$$\dot{E}(t)=2\sum_k\left(\dot{\alpha}_k^R\left\langle \mathcal{O}_k\epsilon^R\right\rangle+\dot{\alpha}_k^I\left\langle \mathcal{O}_k\epsilon^I\right\rangle\right). \tag{7.2.34}$$

Contracting Eqs. (7.2.10) we get $\sum_k \dot{\alpha}_k^I\left\langle \mathcal{O}_k\epsilon^I\right\rangle=-\sum_k \dot{\alpha}_k^R\left\langle \mathcal{O}_k\epsilon^R\right\rangle$, therefore the energy is conserved as $\dot{E}(t)=0$.

7.2.4 Real-Time Variational Monte Carlo

In the previous discussions we have derived both the variational ansatz and the equations of motion for its complex-valued parameters. A crucial point for the scheme to be effective is therefore to provide a reliable solution of those equations in a general case where the correlated structure of the wave-function does not allow for analytical solutions. When this is the case, the variational Monte Carlo method allows for an exact solution for the variational trajectories. Indeed, at each time, the square modulus of the wave-function $|\psi(\mathrm{x},t)|^2$can be straightforwardly interpreted as a probability distribution over the Hilbert space spanned by the configurations x and a Markov process can be devised whose stationary equilibrium distribution coincides with the desired measure.

To this purpose, we consider transitions in the Hilbert space driven by the probabilities

$$T_{\mathbf{x}\rightarrow\mathbf{x}'}=\frac{1}{w(\mathbf{x},t)}\frac{|\psi(\mathbf{x}',t)|}{|\psi(\mathbf{x},t)|}, \tag{7.2.35}$$

where $w(\mathrm{x},t)$ is normalization factor and the candidate states x' are restricted to the finite set of configurations such that $\mathcal{H}_{x,x'}\neq 0$. Within such a choice, a new configuration x′ is accepted or rejected according to the Metropolis algorithm with probability $P=\min\left\{1,w(\mathbf{x})/w(\mathbf{x}')\right\}$. The particular choice for the transition probabilities allows for an effective importance sampling, in which configurations with a greater modulus of the wave-function are more often proposed than less likely ones.

At each time, expectation values of both the correlation matrix $S_{k,k'}=\left\langle \mathcal{O}_k\mathcal{O}_{k'}\right\rangle-\left\langle \mathcal{O}_k\right\rangle\left\langle \mathcal{O}_{k'}\right\rangle$ and the local energy parts entering the right hand-sides of (7.2.14-7.2.15) are computed as statistical averages over the random walk. The linear system of equations (7.2.14-7.2.15) can be therefore solved in order to obtain at each time the first-order derivatives of the variational parameters, which can be in turn integrated by means of standard algorithms for first-order differential equations.

7.3 Examples of Exactly Solvable Quantum Dynamics

Before showing an application of the above introduced method to a realistic system, it is instructive to analyze some simple situations in which the generalized Jastrow ansazt provides an exact dynamics.

7.3.1 Harmonic Oscillator

We first start considering a simple one dimensional quantum oscillator described by the Hamiltonian

$$\mathcal{H} = -\frac{1}{2}\frac{\partial^2}{\partial x^2} + \frac{1}{2}x^2. \tag{7.3.1}$$

A normalized state (which resides in the cathegory of the generalized Jastrow factors) of the form

$$\psi(x;\alpha) = \sqrt[4]{\frac{\alpha^R}{\pi}} e^{-\alpha\frac{x^2}{2}}, \tag{7.3.2}$$

is also considered, where $\alpha = \alpha^R + i\alpha^I$ is complex parameter whose real part is strictly positive. Fixing the parameter to a real value $\alpha = \alpha_0 > 0$, we now consider the exact time evolution of this state under the action of the Hamiltonian (7.3.1). The evolved state can be obtained in many different ways, in particular it can be computed in the path-integral formalism as

$$\psi(x,t) = \int G_t(x,x')\psi(x',0)dx', \tag{7.3.3}$$

where the propagator $G_t(x,x')$ reads

$$G_t(x,x') = \sqrt{\frac{1}{2\pi i \sin(t)}} \exp\left[-\frac{x^2\cos(t) - 2xx' + x'^2\cos(t)}{2i\sin(t)}\right]. \tag{7.3.4}$$

The evolved state can be then exactly computed performing the integration (7.3.3) and can conveniently expressed as

$$\psi(x,t) = e^{i\phi(t)}\left\{\sqrt[4]{\frac{\alpha^R(t)}{\pi}} e^{-\alpha(t)\frac{x^2}{2}}\right\}, \tag{7.3.5}$$

i.e. the time evolution leaves the functional form of the wave-function *unchanged* (apart from a global phase factor) while leading to a time dependence of the complex parameter which read

$$\alpha^R(t) = \frac{\alpha_0}{\alpha_0^2 \sin^2(t) + \cos^2(t)} \tag{7.3.6}$$

$$\alpha^I(t) = \frac{(\alpha_0^2 - 1)\sin(t)\cos(t)}{\alpha_0^2 \sin^2(t) + \cos^2(t)}, \tag{7.3.7}$$

while the phase factor is

$$\phi(t) = \arg\left\{1/\sqrt{\cos(t) + i\alpha_0 \sin(t)}\right\}. \tag{7.3.8}$$

Notice that when $\alpha_0 = 1$ the wave-function is the ground state with energy $E_0 = 1/2$ and the time-evolved parameters have the constant values $\alpha^R(t) = \alpha_0$, $\alpha^I(t) = 0$ while the phase factor is $\phi = -t/2 = -E_0 t$.

Due to the fact that the time evolution preserves exactly the functional form of the wave-function, the same equations for the dynamics can be obtained considering the time-dependent variational scheme for a state of the form (7.3.2). The differential equations for the variational parameters can be obtained considering the observable $\mathcal{O}(x) = -\frac{x^2}{2}$ coupled to the complex parameter $\alpha(t)$ and are

$$\dot{\alpha}^R(t) = -2\alpha^R(t)\alpha^I(t) \tag{7.3.9}$$

$$\dot{\alpha}^I(t) = \alpha^R(t)^2 - \alpha^I(t)^2 - 1, \tag{7.3.10}$$

which, as it can be proven by inspection, are satisfied by Eqs. (7.3.6,7.3.7). In conclusion, the variational real-time dynamics is *exact* for coherent states evolving with the quantum harmonic oscillator Hamiltonian.

7.3.2 Tomonaga-Luttinger Liquid

A non-trivial model for the low-interacting regime of one dimensional fermions is described by the well known Tomonaga-Luttinger Hamiltonian, which in momentum space reads

$$\mathcal{H}_{TL} = \frac{v_F}{2} \sum_q \left(K\, \mathit{\Pi}_q\, \mathit{\Pi}_{-q} + \frac{q^2}{K}\, \mathit{\Phi}_q\, \mathit{\Phi}_{-q} \right), \tag{7.3.11}$$

where we have introduced the bosonic fields

$$\mathit{\Phi}_q = \frac{1}{\sqrt{2|\,q|}} \left(a_q^\dagger + a_{-q}\right) \tag{7.3.12}$$

$$\mathit{\Pi}_q = i\sqrt{\frac{|\,q|}{2}} \left(a_{-q}^\dagger - a_q\right), \tag{7.3.13}$$

K is the strength of the interaction between q-modes and v_F is the Fermi velocity.

For any interaction strength, this model can be exactly diagonalized by means of a standard Bogoliubov rotation (see for example [58]). An interesting point is however that its ground state can also be exactly expressed as a Jastrow factor of the form

$$|\Psi\left(J_q\right)\rangle = e^{-\frac{1}{2}\sum_{q>0} J_q\, N_q\, N_{-q}}\, |\Psi_0\rangle \,, \tag{7.3.14}$$

where the Fourier transforms of the density N_q have been introduced, the Jastrow pseudo-potential J_q and $|\Psi_0\rangle$ is the non-interacting ground state of (7.3.11) for $K = 1$. It can be shown [139] that the ground-state energy of the model is $E_{GS} = \sum_q \frac{v_F}{2}|q|$ which is obtained imposing

$$J_q = \frac{\pi}{q}\left(\frac{1}{K} - 1\right). \tag{7.3.15}$$

The functional Jastrow form however does not only correctly describes the ground state of the Tomonaga-Luttinger model but also its dynamics. To demonstrate this very interesting feature, we consider for simplicity a quantum quench in which the system is initially prepared in the non-interacting Fermi sea and it is let evolve with the fully interacting Tomonaga-Luttinger Hamiltonian, namely

$$|\Psi(t)\rangle = e^{-i\mathcal{H}_{TL}t}|\Psi_0\rangle. \tag{7.3.16}$$

In this case, the exactly evolved state reads

$$|\Psi(t)\rangle = e^{\phi(t)}e^{-\frac{1}{2}\sum_{q>0} J_q(t)\, N_q\, N_{-q}}\, |\Psi_0\rangle \,, \tag{7.3.17}$$

with the time-dependent Jastrow pseudo-potential being equal to [41]

$$J_q(t) = \frac{\pi}{q}\left(\frac{1-K^2}{K^2 - iK\cot(\epsilon_q t)}\right), \tag{7.3.18}$$

where ϵ_q are the excited states energies of the Tomonaga-Luttinger Hamiltonian and $\phi(t)$ is a time-dependent phase factor.

The above presented result in turn implies that the Jastrow ansatz for the quantum dynamics is expected to be a generally good approximation in the low-interacting regime. We will however highlight in the following that a generalized Jastrow description of the dynamics is accurate also in the strong-interacting regime, therefore providing a satisfying and flexible description of the two opposite limiting cases.

7.4 Quantum Quenches in the Bose-Hubbard Model

As a non trivial application of the time-dependent Variational Monte Carlo method, we now consider the dynamics of a correlated bosonic system driven out of equilibrium. More specifically, we aim to provide a satisfactory description of the phenomenological issues described in the previous Chapter. We concentrate again on a system which we imagine to be well described by the Bose-Hubbard Hamiltonian

$$\mathcal{H} = -J \sum_{\langle i,j \rangle} \left(b_i^\dagger b_j + \text{h.c.} \right) + \frac{U}{2} \sum_i n_i (n_i - 1), \tag{7.4.1}$$

and consider initial states which correspond to the ground state of such Hamiltonian for a given value of the interaction, U_i. The initial, spatially homogeneous, prepared state is then let evolve with another interaction strength $U_f > U_i$. This sudden quench in the interaction is indeed practically achievable in experiments with cold atoms, as for example in [142].

In the previous discussion on the metastable states of the Bose-Hubbard model, we have revealed the existence of a threshold energy above which a steep increase of the relaxation time of density fluctuations takes place. In order to assess the relevance of this phenomenon for the dynamics of larger systems or even for higher spatial dimensions, it is desirable to devise a comprehensive alternative framework able to catch its very characteristics. The real-time variational Monte Carlo approach has, from this perspective, two important advantages: it allows us to follow the evolution for times comparable to those accessible experimentally, which are much longer than t-DMRG; [149, 43] it can be easily extended to higher dimensions. Moreover, the physical insight offered by the possibility to have an explicit wave-function at any time of the quantum evolution is certainly another important step towards a satisfactory theoretical understanding of the circumstances in which the ergodicity principle is violated in closed quantum systems. Indeed, even though theoretical achievements in this direction have been possible in recent years thanks to mean-field-like variational analysis, [119, 123] a plethora of questions concerning the very validity of these approaches is under debate. Although the mean-field-like description seems to capture well the main features of the dynamical evolution, these methods are unable to describe very important aspects such as damping and relaxation.

In the following we present variational results for the dynamics of the Bose-Hubbard model as obtained by means of both a simple variational Gutzwiller Wave Function and a more accurate Jastrow factor with long-range density interactions.

7.4.1 Gutzwiller Wave Function

Many basic concepts in the theory of strongly correlated systems, like e.g. the Brinkman-Rice scenario for the Mott transition, have been originated from calculations based on a very simple and physically transparent variational approach introduced in the 60th's by Gutzwiller [66]. Its extension to out of equilibrium phenomena has been however only recently realized with evidences of a dynamical transition for both fermions [88, 119] and bosons[123] being reported.

In simply Hubbard like models, the Gutzwiller approximation amounts to consider on-site correlations induced by the interplay between the potential and the kinetic energies. In our analysis we choose a wave-function of the form

$$|\Psi(t)\rangle = \exp\left(\sum_i g(t)n_i(n_i-1)\right)|\Psi_0\rangle, \tag{7.4.2}$$

where the complex time-dependent variational parameter $g(t)$ is coupled to the double occupancy and $|\Psi_0\rangle$ is the best Gutzwiller variational description for the ground state of (7.4.1) at a given U_i. In the static case, the double occupancies are exponentially suppressed in the Mott phase (large negative values of g), whereas kinetic fluctuations and superfluidity are favored for small values of g. In the general formalism of the wave-functions ansatz introduced with (7.2.13), the excitation operator of the Gutzwiller wave-function is simply the double occupancy, namely $\mathcal{O}_g(\mathbf{x}) = \sum_i n_i(n_i-1)$.

We analyze the out of equilibrium dynamics of the Bose-Hubbard Hamiltonian at unitary filling $n=1$ and for a one dimensional geometry. Being the excitation operator related to the potential energy of the Hamiltonian, it is natural to analyze its time-dependency after a quantum quench. In Figure 7.4.1 we show the time-dependent expectation value of the potential energy after a quantum quench in which the initial state is taken to be the best Gutzwiller variational state at $U_i = 2J$. One of the main features emerging from this variational results is that the potential energy does not relax to an equilibrium value after a certain equilibration time. The time-dependent expectation values indeed continuously oscillate in a limited band. This lack of damping is in turn due to the lack of explicit density correlations in the wave-function and it is indeed far from the exact behavior,[76] in which damping and relaxation are observed.

The Gutzwiller treatment however features a suggestive dynamical phase transition which is expected to hold in higher dimensions. In our treatment of the Gutzwiller ansatz we observe such a transition at the critical energy threshold $E_c(U_f) = 0$, i.e. when the internal energy of the quench is vanishing. As shown in Figure 7.4.2, below the critical energy or equivalently, the critical interaction U^c_{dyn}, the imaginary part of the Gutzwiller parameter $g(t)$ is oscillating. On the contrary, above the critical energy the imaginary part of $g(t)$ starts preceding with an almost ballistic behavior. Both the critical interaction values and the precession

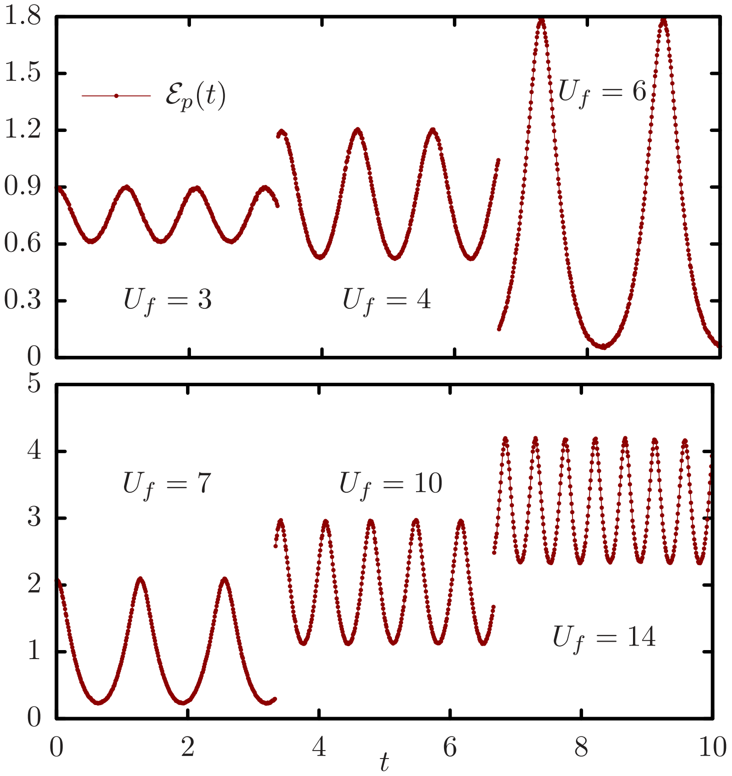

Fig. 7.4.1 Time-dependent expectation values of the on-site potential energy $\mathcal{E}_p(t) = \frac{U_f}{2} \langle n_i(n_i - 1)\rangle$, different values of U_f are shown in different time windows for clarity. The initial state is the optimal Gutzwiller variational ground state of the Bose-Hubbard Hamiltonian with $U_i = 2J$. Real-time Variational Monte Carlo results with a Gutzwiller wave function are obtained for an $N = 100$ chain with periodic boundaries.

of complex phase associated to the double occupancy, are features consistent with previous Gutzwiller calculations[119, 123]. However, an important difference we find is in the lack of damping of the double occupancy at the critical interaction point. This feature, clearly emerged in the fermionic case and in the bosonic case when a maximum number of particles per site was imposed. We instead find that, upon lifting the maximum occupation number constraint, the peculiar relaxation of the double occupancy at the transition point is no longer observed, whereas the critical transition is still well evident in the imaginary part of the Gutzwiller parameter.

7.4.2 Jastrow Wave Function

A substantial improvement over the Gutzwiller wave-function for strongly correlated systems is realized in the context of the Jastrow correlated wave-functions. The equilibrium phase

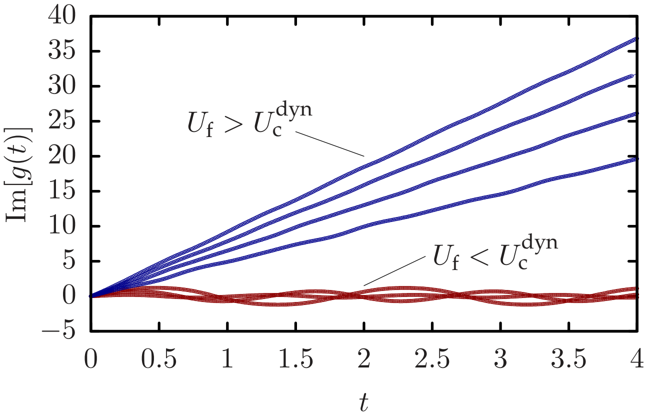

Fig. 7.4.2 Imaginary part of the Gutzwiller parameter as a function of time. Under the critical point the parameter oscillates while above the critical energy threshold a precession is observed. The initial state is the optimal Gutzwiller variational ground state of the Bose-Hubbard Hamiltonian with $U_i = 2J$. Real-time Variational Monte Carlo results with a Gutzwiller wave function are obtained for an $N = 100$ chain with periodic boundaries.

diagram of the Bose-Hubbard model and the quantitative description of the Mott phase are some of the major physical properties that are well described by the Jastrow ansatz.[28] Long-range density correlations are included in a consistent way in the Jastrow wave functions and allow for a description of the static Mott phase in which kinetic fluctuations are not completely suppressed as per the Gutzwiller ansatz.

In the following, we introduce an extension to time dependent problems of the Jastrow wave-functions, namely we consider :

$$|\Psi(t)\rangle = \exp\left(\sum_{ij} V_{ij}(n_i, n_j; t)\right) |\Psi_0\rangle, \tag{7.4.3}$$

where $|\Psi_0\rangle$ is the initial state and $V_{ij}(n_i, n_j; t)$ is a Jastrow factor that depends on the occupancies n_i and n_j of two sites i and j and varies with time so to maintain the time evolution as close as possible to the true evolution via the Schrödinger equation.

Results for the time evolution of a local observable, such as the potential energy, after a sudden quench from $U_i = 2J$ to a final U_f are shown in Fig. 7.4.4. The values of the thermal averages have been computed in the grand-canonical ensemble by means of finite-temperature quantum Monte Carlo calculations, [10] with the effective temperature fixed by the average energy of the initial state, which we take as the best variational approximation for the ground state at $U_i = 2J$. Moreover, the comparison between our approach and the t-DMRG [75] is reported in Figure 7.4.3, demonstrating the high accuracy of the time-dependent variational Monte Carlo.

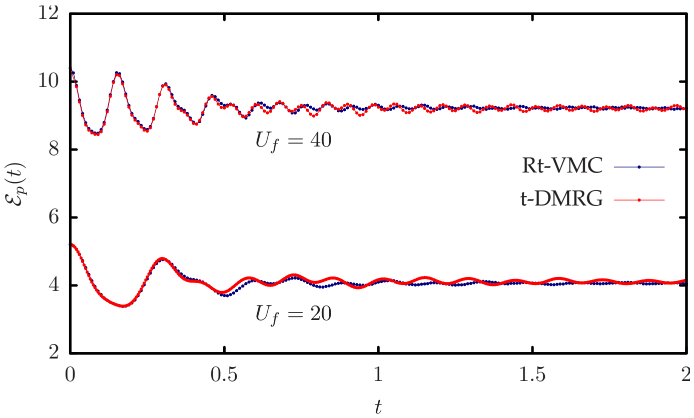

Fig. 7.4.3 Time-dependent expectation values of the on-site potential energy $\mathcal{E}_p(t) = \frac{U_f}{2} \langle n_i(n_i - 1) \rangle$. The initial state is the ground state of the Bose-Hubbard Hamiltonian with $U_i = 2J$. Real-time Variational Monte Carlo results are obtained for an $N = 100$ chain with periodic boundaries. Corresponding data by t-DMRG [75] are the potential energy at the center of an $N = 64$ chain with open boundaries.

As shown in Fig. 7.4.4, in the region of small U_f we observe a damping of the average potential-energy, which approaches a quasi-steady stationary value in contrast to the simple Gutzwiller wave function, [119, 123]. In this regime, damping is mainly due to a density-density Jastrow factor of the form $V_{ij}(n_i, n_j) = v_{ij}\, n_i\, n_j$, which already at equilibrium was shown to provide a satisfactory description of the physical behavior. [28] This fact enlightens the relevance of the Bogoliubov modes whose dephasing during the time evolution allows to approach the stationary state. Remarkably, the steady state averages coincide with the thermal ones; a signal that the dynamics is ergodic.

In the region of large interactions U_f, a simple density-density Jastrow factor does not account for all relaxation pathways, which will now mainly result from specific correlations among doublons, holons and between holons and doublons. The effective Hamiltonian (6.3.1) indeed explicitly shows that doublons attract each other as well as holons do, while doublons repel holons. These correlations, as well as other among higher on-site densities, can be easily implemented via the the Jastrow factor in Eq. (7.4.3) and indeed substantially improve the dynamics. Interestingly, the effective interaction between doblons that results from the dynamical variational calculation turns to be *attractive*, therefore leading to a consistent determination of the anticipated dynamical effects that drive the dynamics in this regime.

As we see from Fig. 7.4.4, in the region of very large U_f the potential-energy expectation values do show a damping to a non-thermal quasi-steady state on a time of the order of $\tau_D \sim 1/U_f$. This fast time scale must be put in comparison with the much longer one, τ_R of Fig. 6.4.1. It is natural to identify τ_R with the time scale that controls the eventual escape from the quasi-steady state, hence the approach to thermal equilibrium. Whether this time scale does truly diverge in the thermodynamic limit, or rather saturates to a very large value which is still out of reach for state of the art numerics, it is certainly an important issue that cannot be definitively

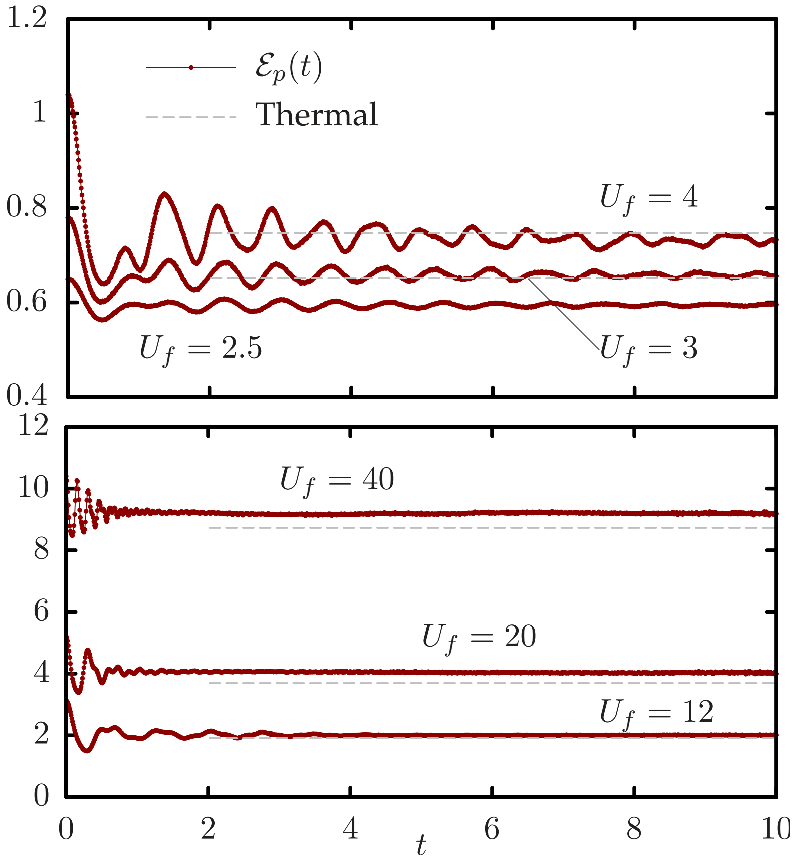

Fig. 7.4.4 Time-dependent expectation values of the on-site potential energy $\mathcal{E}_p(t) = \frac{U_f}{2}\langle n_i(n_i-1)\rangle$ in the ergodic (*upper panel*) and in the non-ergodic regions (*lower panel*). The initial state is the ground state of the Bose-Hubbard Hamiltonian with $U_i = 2J$ and the considered system size is $N = 200$. Grand-canonical thermal averages are shown for comparison as dashed horizontal lines.

solved. However, we can safely state that a large finite system of actual experimental relevance will get stuck for a quite long time into highly inhomogeneous metastable states, which we revealed to be on the verge of a spatial symmetry breaking.

Within the Jastrow variational treatment, the onset of the dynamical transition is in the non-analytic behavior of the dynamical averages at the transition point. As shown in Figure 7.4.5, the long-time averages of the double occupancy have indeed a discontinuous derivative at U^c_{dyn}, where a pronounced cusp is observed.

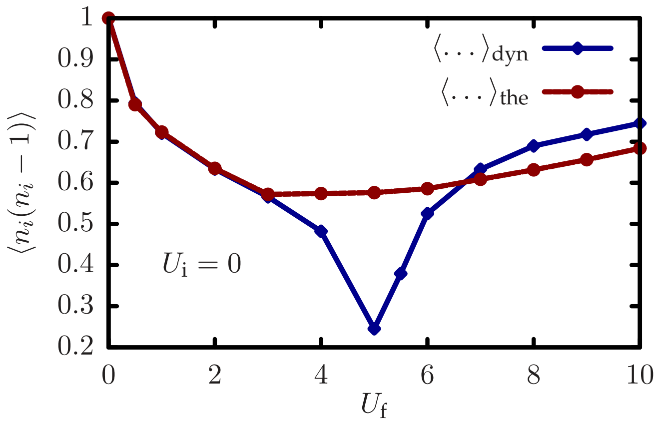

Fig. 7.4.5 Quantum quenches for a one-dimensional Bose-Hubbard chain initially in the non-interacting superfluid phase ($U_i = 0$). The expectation values of the double occupancy are shown as a function of the final interaction strength U_f. The two curves correspond to long-time dynamical averages $\langle \dots \rangle_{\text{dyn}}$ and canonical thermal averages $\langle \dots \rangle_{\text{the}}$ at the corresponding effective temperature.

7.5 Two-Dimensional Systems

The above results have been obtained for out-of-equilibrium one dimensional systems and therefore leave the questions concerning the dependence on the dimensionality of the problem still open. However, the anomalously long-time relaxation of the density auto-correlation points towards a kind of glassy behavior that should be observable even in higher dimensions, provided that the interaction induces sufficiently strong dynamical constraints. In this regard, we have studied the two-dimensional case by means of our time-dependent variational scheme, verifying that a similar behavior occurs even in two dimensions. In Fig. 7.5.1, we show the results of the same experiment simulated previously in one dimension but now in a square lattice. The system is prepared in a non-uniform configuration, with sites on one sublattice occupied by two bosons, and on the other sublattice by none. As before, if the repulsion is weak the density profile equilibrates to a uniform distribution, while for strong repulsion the density stays close to the initial configuration for extremely long times. We therefore argue that the phenomenology we have hereby identified is almost independent on the dimensionality and it is rather due to the existence in strongly correlated systems of high-energy incoherent excitations that do not have channels to relax efficiently. This scenario is also consistent with the observed strong doping dependence of the relaxation time that we have discussed in 6.3.3.

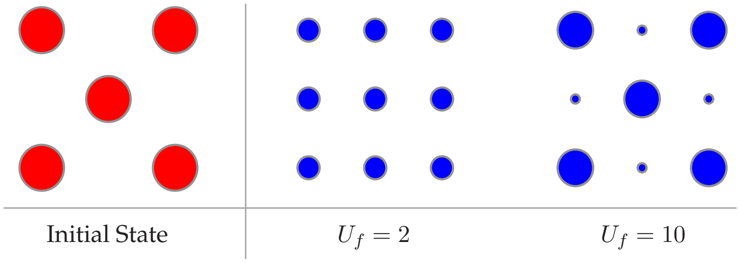

Fig. 7.5.1 Long-time density averages for a two-dimensional square lattice. We show here only a small piece, 9 sites, of the 100-site cluster that we simulated using the real-time variational MC method. The initial state is prepared to have a non-uniform density and it is let evolve with the homogeneous Bose-Hubbard Hamiltonian (6.2.1) for different values of the interaction strength.

7.6 Discussion

In this Chapter we have shown an extension of the static variational method for correlated systems to the out of equilibrium dynamics. A physically sound time dependent ansatz for the evolved wave-function can be derived considering a set of Feynman-like excitation operators that drive the dynamics. Whenever the complex many body dynamics is characterized by a well defined set of relevant excitations, our approach is expected to be particularly accurate. This prescription holds in a number of relatively simple cases in which the dynamics can be studied analytically. We have however demonstrated that this is also the case for more challenging applications such as the experimentally relevant quantum quenches in the Bose-Hubbard model. Concerning the latter, have obtained for the first time a consistent variational description of important physical features such as the damping and the relaxation of local observables, otherwise absent in mean-field treatments. The picture emerging within our generalized Jastrow theory is consistent with the phenomenology introduced in the previous Chapter and points towards a dynamical phase transition characterized by a consistent slowing down of the density excitations.

The extension of the method to other systems of interest, such as fermions and particles on the continuum is a task of sure interest which will be pursued in future studies. Moreover, the systematic determination and inclusion of excitation operators in the correlated wave-functions is a methodological task of primary importance. In the context of the out of equilibrium dynamics of quantum correlated systems, it is indeed particularly welcome to devise novel and accurate numerical methods. The present limitations of the current numerical schemes is certainly one of the most limiting factors in the understanding of fundamental questions concerning the validity of the ergodic hypothesis and the approach to equilibrium. From this perspective, our approach is able to treat with substantially improved accuracy with respect to mean-field treatment the dynamics of correlated systems even in higher dimensionality, where the lack of exact methods constitutes a manifestly limiting factor.

Epilogue

The extensive research work we have presented in this Thesis has focused onto the characterization of the spectral and dynamical properties of strongly correlated systems. This challenging goal has been tackled upon both the introduction and the extension of different and complementary numerical tools. While a general and complete scheme for the study of low and high energy processes due to strong correlations is yet to be realized, we have shown that accurate answers to previously unaccessible problems can be obtained.

The imaginary-time dynamics is one of the crucial means thanks to which spectral properties of quantum systems can be obtained. We have indeed shown that its stochastic sampling allows for the accurate determination of the excited-states traits of particles with bosonic statistics. We have demonstrated the level of accuracy that can be achieved both for paradigmatic models of correlation (in Chapter 2) and for the study of lattice excitations of ^4He (in Chapter 3). In the latter case, it has been possible to provide a sensible improvement over existing approximate results leading to a direct and satisfactory comparison with experimental neutron scattering data.

On very general grounds, the response of a many-body quantum system to an external perturbation is encoded in its excitations spectrum. Therefore the potential fields of applicability of the demonstrated techniques range from more traditionally studied correlated materials to ultra-cold atomic gases for which spectroscopic techniques are increasingly becoming available.

The potentialities of the imaginary-time dynamics are however not limited to systems with bosonic statistics. We have actually explained and demonstrated that imaginary-time dynamics also constitutes an important tool to ease the study of exact fermionic properties. This intriguing possibility has been substantiated by the introduction of a general scheme in which the excited states of an auxiliary bosonic system are used to infer accurate ground-state fermionic properties. While the specific fields of applicability of the fermionic correlations method have been discussed in Chapter 4, we want to remark here possible future applications and developments. In particular, the analysis of highly interacting fermions in low-dimensional geometries is one of the possible topics in which the method could succeed. The study of confined fermions is indeed a very active field in which the ongoing experimental research with cold atoms is rapidly advancing. Developments in the methodology will therefore need to be twofold. One one hand, it will be fundamental to develop accurate correlated wave-functions to ease the physical interpretation of different levels of cooperative phenomena such as magnetism and superconductivity. Within this direction, efforts should be put in the improvement of the backflow correlations introduced in Chapter 4, and their application to other experimentally relevant situations. On the other hand, the introduction of suitably defined auxiliary bosonic systems with higher energy and a smaller energy gap with respect to the fermionic symmetry sector will be a methodological challenge to be undertaken.

In the second part of the Thesis, we have focused our attention onto closed quantum systems driven out of equilibrium. Within this context, fundamental questions arise concerning the approach of physical observables to equilibrium and the very validity of the Statistical Mechanics description. From a more phenomenological point of view, we have shown in Chapter 6 that an intriguing analogy with the glass transition and its breaking of the ergodicity can be identified. A substantial slowing down of density excitations is indeed observed upon the excitation of high energy eigenstates and due to the presence of strong dynamical constraints. The possibility to identify these phenomenological traits in specific experimental realizations with trapped cold atoms has been put forward and it will hopefully guide the experimental validation of the suggested physical picture.

As a methodological step towards a better understanding of this rich phenomenology, we have moreover introduced a novel approach to the real-time dynamics of quantum particles (in Chapter 7). This field, in which traditionally stochastic methods have faced serious limitations, is one of the most promising playgrounds for future methodological developments. We believe that the introduced possibility to lift some previous restrictions concerning the dimensionality (as for renormalization-based methods) and the accuracy (as for mean-field approaches) will constitute an important aid to future theoretical analyses. Challenges in both the improvement and in the extension of the method have however to be faced. In particular, most of the quality of the variational approximation is due to the adopted time-dependent wave-function. It is therefore natural to pursue research towards its systematic improvements, as much as it has been done in the past years for static variational wave-functions.

Possible extensions of the time-dependent variational method are however numerous and promising, ranging from systems with continuous spatial degrees of freedom to the treatment of time-dependent perturbations. Within the last mentioned point, it would be desirable to provide a consistent variational description of the adiabatic processes and of the universal properties exhibited when passing through critical points. Moreover, the ability to accurately characterize the response to a time-dependent perturbation is a strict requirement for the computational spectroscopy of correlated materials to be successful. We believe that our approach will give its contribution to the development of novel research lines in this direction. In particular in the study of two-dimensional geometries and of their specific properties which are currently unaccessible due to the limiting predictive power of the existing approaches.

In conclusion, we believe that future research oriented to the development and to the improvement of numerical methodologies will be a key requirement to progressively unveil the complexity of correlated quantum systems. In this Thesis we have put our efforts in the advancement of this program contributing with both a refinement of existing methodologies and with the conception of new ones. A better understanding of the physics beyond complex phenomena such as the itinerant ferromagnetism, the superfluidity in quantum glasses and the dynamics of correlated atoms, are specific examples of how these efforts have found successful applications.

Acknowledgements

This Thesis is the result of four years of stimulating work and enriching experiences that I have been the pleasure to live in the city of Trieste. The Condensed Matter Theory sector of Sissa has been much more than simply my hosting institution but more like a familiar environment to me. My passion for research has been reinforced and become more mature in these years and this has been solely possible thanks to the numerous interactions with the people I have been the pleasure to work with.

My supervisors have been the competent and friendly guides who have greatly contributed to this process and whose efforts I would like to public acknowledge hereby. They have guided my work with patience and a mature scientific vision, while allowing me for a substantial freedom in the choice of the subjects to study. For all of these and for the sincere mutual trust we have fostered in these years, I want therefore to express all my gratitude to Stefano, Federico and Saverio.

Special acknowledgments deserve Sandro Sorella and Michele Fabrizio, from whom I have learned many of the things that have made this Thesis possible, and whose genuine enthusiasm for research is contagious. More recently, Alberto Parola has also been a precious reference on the subject of strong correlations, to him I therefore want to address my words of thanks.

Francesco Zamponi, Marco Tarzia and Giulio Biroli have been my guides in the fascinating world of glasses and to them I express my sincere gratefulness.

Much of the unique experiences lived in these years have enjoyed the company and the friendship of many amazing people I have had the luck to meet. I would like to thank my friend and colleague Juan Felipe for all our discussions and for the hours we have spent together enjoying Trieste and becoming more adults. My friends and colleagues at Sissa have been always a reference point for me, and here is to them, Marco, Lorenzo, Gabriele, Giovanni.

I would like to thank all the good friends that have been always on my side in the good and in the less-good luck. In particular Pilar, for she has been like a part of my family in these years. Angus, for all the sense of freedom I have grasped from him. Lorenzo and Paola, for their generosity and genuine friendship. Dario, for the hours spent discussing together and for

all his wise words at the end of my outbursts. Marco and Serena for all their good advises and their being-so-couple which is *per se* comforting in many circumstances.

"*Thank you, guys*" to Gaz, Giacomo, Federica, Duvan, Iga and Violeta who have been the best part of the experiences enjoyed together. Thank you to Claudia, Carlo and Bianca who have enlivened many moments of my life in Trieste.

Lastly, there is a person who has been particularly close to me and to whom, after all, I would like to say "grazie" for all the unrepeatable moments we have lived together. This is by far the least scientific acknowledgment, but it is the most heartfelt. And here is to you, Chiara.

References

[1] **Abrikosov A.A.** *Methods of Quantum Field Theory in Statistical Physics*. Selected Russian Publications in the Mathematical Sciences. Dover Publications (1975).

[2] **Anderson P.W.** *Absence of diffusion in certain random lattices*. Physical Review, 109(5):1492 (1958).

[3] **Anderson P.W.** *Local moments and localized states*. Nobel Lecture (1977).

[4] **Anderson P.W.** *The resonating valence bond state in* La_2CuO_4 *and superconductivity*. Science, 235(4793):1196 (1987).

[5] **Aziz R.A., Nain V.P.S., Carley J.S., Taylor W.L. and McConville G.T.** *An accurate intermolecular potential for helium*. The Journal of Chemical Physics, 70(9):4330 (1979).

[6] **Azuah R.T., Stirling W.G., Glyde H.R. and Boninsegni M.** *Momentum distribution and final state effects in liquid neon*. Journal of Low Temperature Physics, 109(1):287 (1997).

[7] **Baroni S. and Moroni S.** In **Nightingale P. and Umrigar C.J.**, editors, *Quantum Monte Carlo Methods in Physics*, volume 525 of *C*, page 313. NATO ASI, Kluwer Academic Publishers, Boston (1999).

[8] **Baroni S. and Moroni S.** *Reptation quantum monte carlo: A method for unbiased ground-state averages and imaginary-time correlations*. Physical Review Letters, 82(24):4745 (1999).

[9] **Basko D., Aleiner I. and Altshuler B.** *Metal-insulator transition in a weakly interacting many-electron system with localized single-particle states*. Annals of Physics, 321(5):1126 (2006).

[10] **Bauer B. et al.** *The alps project release 2.0: Open source software for strongly correlated systems*. Journal of Statistical Mechanics, page P05001 (2011).

[11] **Becca F., Parola A. and Sorella S.** *Ground-state properties of the hubbard model by lanczos diagonalizations*. Physical Review B, 61(24):R16287 (2000).

[12] **Becca F. and Sorella S.** *Nagaoka ferromagnetism in the two-dimensional infinite- u hubbard model*. Physical Review Letters, 86(15):3396 (2001).

[13] **Bednorz J.G. and Müller K.A.** *Perovskite-type oxides - the new appproach to high-t_c superconductivity*. Nobel Lecture (1987).

[14] **Belitz D., Kirkpatrick T.R. and Vojta T.** *How generic scale invariance influences quantum and classical phase transitions*. Reviews of Modern Physics, 77(2):579 (2005).

[15] **Benguigui L.** *Critical point of infinite type*. Physical Review B, 16(3):1266 (1977).

[16] **Billy J., Josse V., Zuo Z., Bernard A., Hambrecht B., Lugan P., Clement D., Sanchez-Palencia L., Bouyer P. and Aspect A.** *Direct observation of anderson localization of matter waves in a controlled disorder*. Nature, 453(7197):891 (2008).

[17] **Biroli G., Chamon C. and Zamponi F.** *Theory of the superglass phase*. Physical Review B, 78(22):224306 (2008).

[18] **Biroli G., Kollath C. and Läuchli A.M.** *Effect of rare fluctuations on the thermalization of isolated quantum systems*. Physical Review Letters, 105(25):250401 (2010).

[19] **Biroli G. and Mézard M.** *Lattice glass models*. Physical Review Letters, 88(2):025501 (2001).

[20] **Bloch F.** *Bemerkung zur elektronentheorie des ferromagnetismus und der elektrischen leitfähigkeit*. Zeitschrift für Physik, 57(7):545 (1929).

[21] **Bloch I., Dalibard J. and Zwerger W.** *Many-body physics with ultracold gases*. Reviews of Modern Physics., 80(3):885 (2008).

[22] **Boninsegni M. and Ceperley D.M.** *Density fluctuations in liquid 4he. path integrals and maximum entropy*. Journal of Low Temperature Physics, 104(5):339 (1996).

[23] **Boninsegni M., Prokof'ev N. and Svistunov B.** *Superglass phase of ^{4}He*. Physical Review Letters, 96(10):105301 (2006).

[24] **Boninsegni M., Prokof'ev N. and Svistunov B.** *Worm algorithm for continuous-space path integral monte carlo simulations*. Physical Review Letters, 96(7):070601 (2006).

[25] **Brockhouse B.N. and Iyengar P.K.** *Normal modes of germanium by neutron spectrometry*. Physical Review, (3):747.

[26] **Calabrese P. and Cardy J.** *Quantum quenches in extended systems*. Journal of Statistical Mechanics, page P06008 (2007).

[27] **Canovi E., Rossini D., Fazio R., Santoro G.E. and Silva A.** *Quantum quenches, thermalization, and many-body localization*. Physical Review B, 83(9):094431 (2011).

[28] **Capello M., Becca F., Fabrizio M. and Sorella S.** *Superfluid to mott-insulator transition in bose-hubbard models*. Physical Review Letters, 99(5):056402 (2007).

[29] **Capriotti L., Becca F., Parola A. and Sorella S.** *Resonating valence bond wave functions for strongly frustrated spin systems*. Physical Review Letters, 87(9):097201 (2001).

[30] **Carleo G., Becca F., Moroni S. and Baroni S.** *Reptation quantum monte carlo algorithm for lattice hamiltonians with a directed-update scheme*. Physical Review E, 82(4):046710 (2010).

[31] **Carleo G., Becca F., Schiró M. and Fabrizio M.** *Localization and glassy dynamics of many-body quantum systems*. ArXiv, (1109.2516) (2011).

[32] **Carleo G., Becca F., Sorella S., Schiró M. and Fabrizio M.** *Time-dependent variational monte carlo*. In Preparation (2011).

[33] **Carleo G., Moroni S. and Baroni S.** *Zero-temperature dynamics of solid ^{4}He from quantum monte carlo simulations*. Physical Review B, 80(9):094301 (2009).

[34] **Carleo G., Moroni S., Becca F. and Baroni S.** *Itinerant ferromagnetic phase of the hubbard model*. Physical Review B, 83(6):060411 (2011).

[35] **Carleo G., Tarzia M. and Zamponi F.** *Bose-einstein condensation in quantum glasses*. Physical Review Letters, 103(21):215302 (2009).

[36] **Ceperley D.M.** *Path integrals in the theory of condensed helium*. Reviews of Modern Physics, 67(2):279 (1995).

[37] **Ceperley D.M. and Bernu B.** *The calculation of excited state properties with quantum monte carlo*. 89(10):6316 (1988).

[38] **Ceperley D.M. and Pollock E.L.** *Path-integral computation of the low-temperature properties of liquid ^{4}He*. Physical Review Letters, 56(4):351 (1986).

[39] **Ciamarra M.P., Tarzia M., de Candia A. and Coniglio A.** *Lattice glass model with no tendency to crystallize*. Physical Review E, 67(5):057105 (2003).

[40] **Clark B.K. and Ceperley D.M.** *Path integral calculations of vacancies in solid helium*. Computer Physics Communications, 179(1-3):82 (2008).

[41] **Coira E.** *Quench dynamics in one-dimensional Luttinger liquids*. Master's thesis, Università Degli Studi Dell'Insubria (2010).

[42] **Conduit G.J., Green A.G. and Simons B.D.** *Inhomogeneous phase formation on the border of itinerant ferromagnetism*. Physical Review Letters, 103(20):207201 (2009).

[43] **Daley A.J. et al.** *Time-dependent density-matrix renormalization-group using adaptive effective hilbert spaces*. Journal of Statistical Mechanics, page P04005 (2004).

[44] **Dang L., Boninsegni M. and Pollet L.** *Disorder-induced superfluidity*. Physical Review B, 79(21):214529 (2009).

[45] **Diallo S.O., Pearce J.V., Azuah R.T. and Glyde H.R.** *Quantum momentum distribution and kinetic energy in solid he*. Physical Review Letters, 93(7):075301 (2004).

[46] **Diallo S.O., Pearce J.V., Azuah R.T., Kirichek O., Taylor J.W. and Glyde H.R.** *Bose-einstein condensation in solid ^{4}he*. Physical Review Letters, 98(20):205301 (2007).

[47] **Dirac P.A.M.** *The lagrangian in quantum mechanics*. Physikalische Zeitschrift der Sowjetunion, 364:72 (1932).

[48] **Doucot B. and Wen X.G.** *Instability of the nagaoka state with more than one hole*. Physical Review B, 40(4):2719 (1989).

[49] **Feynman R.P.** *Forces in molecules*. Physical Review, 56:340 (1939). URL `http://link.aps.org/doi/10.1103/PhysRev.56.340`.

[50] **Feynman R.P.** *Space-time approach to non-relativistic quantum mechanics*. Rev. Mod. Phys., 20:367 (1948).

[51] **Fisher M.P.A., Weichman P.B., Grinstein G. and Fisher D.S.** *Boson localization and the superfluid-insulator transition*. Physical Review B, 40(1):546 (1989).

[52] **Foini L., Semerjian G. and Zamponi F.** *Quantum biroli-mézard model: Glass transition and superfluidity in a quantum lattice glass model*. Physical Review B, 83(9):094513 (2011).

[53] **Fokker A.D.** *Die mittlere energie rotierender elektrischer dipole im strahlungsfeld*. Annalen der Physik, 348(4):810 (1914).

[54] **Foulkes W.M.C., Mitas L., Needs R.J. and Rajagopal G.** *Quantum monte carlo simulations of solids*. Reviews of Modern Physics, 73(1):33 (2001).

[55] **Franjić F. and Sorella S.** *Spin-wave wave function for quantum spin models*. Progress of Theoretical Physics, 97(3):399 (1997).

[56] **Galli D.E. and Reatto L.** *Vacancy excitation spectrum in solid ^{4}He and longitudinal phonons*. Physical Review Letters, 90(17):175301 (2003).

[57] **Gebhard F. and Zotos X.** *Gutzwiller wave-function description of a particle in a fermionic bath*. Physical Review B, 43(1):1176 (1991).

[58] **Giamarchi T.** *Quantum physics in one dimension*. International series of monographs on physics. Clarendon (2004).

[59] **Gillis N.S., Koehler T.R. and Werthamer N.R.** *Calculation of the self-consistent phonon spectrum of hcp ^{4}he*. Physical Review, 175(3):1110 (1968).

[60] **Glyde H.R.** *Impulse approximation in solid helium*. Journal of Low Temperature Physics, 59(5):561 (1985).

[61] **Glyde H.R.** *Excitations in liquid and solid helium*. Oxford Science Publications (1994).

[62] **Glyde H.R.** *Momentum distributions and final-state effects in neutron scattering*. Physical Review B, 50(10):6726 (1994/09/01/).

[63] **Good P.** *Resampling Methods*. Birkhäuser, 3rd edition (2006).

[64] **Gubernatis J.E., Jarrell M., Silver R.N. and Sivia D.S.** *Quantum monte carlo simulations and maximum entropy: Dynamics from imaginary-time data*. Physical Review B, 44(12):6011 (1991).

[65] **Guo M., Bhatt R.N. and Huse D.A.** *Quantum critical behavior of a three-dimensional ising spin glass in a transverse magnetic field*. Physical Review Letters, 72(26):4137 (1994).

[66] **Gutzwiller M.C.** *Correlation of electrons in a narrow s band*. Physical Review, 137:A1726 (1965).

[67] **Hellmann H.G.A.** *Forces in molecules*. Einführung in die Quantenchemie, page 285 (1937).

[68] **Hubbard J.** Proc. R. Soc. London, A 276:283 (1963).

[69] **Hunt B., Pratt E., Gadagkar V., Yamashita M., Balatsky A.V. and Davis J.C.** *Evidence for a superglass state in solid ^{4}He*. Science, 324(5927):632 (2009).

[70] **Jaksch D., Bruder C., Cirac J.I., Gardiner C.W. and Zoller P.** *Cold bosonic atoms in optical lattices*. Physical Review Letters, 81(15):3108 (1998).

[71] **Jo G.B., Lee Y.R., Choi J.H., Christensen C.A., Kim T.H., Thywissen J.H., Pritchard D.E. and Ketterle W.** *Itinerant ferromagnetism in a fermi gas of ultracold atoms*. Science, 325(5947):1521 (2009).

[72] **Jordens R., Strohmaier N., Gunter K., Moritz H. and Esslinger T.** *A mott insulator of fermionic atoms in an optical lattice*. Nature, 455(7210):204 (2008).

[73] **Kalos M.H.** *Monte carlo calculations of the ground state of three- and four-body nuclei*. Physical Review, 128:1791 (1962).

[74] **Karatzas I. and Shreve S.E.** *Brownian Motion and Stochastic Calculus*. Graduate Texts in Mathematics. Springer (1991).

[75] **Kollath C.** Private Communication (2011).

[76] **Kollath C., Läuchli A.M. and Altman E.** *Quench dynamics and nonequilibrium phase diagram of the Bose-Hubbard model*. Physical Review Letters, 98:180601 (2007).

[77] **Krauth W., Trivedi N. and Ceperley D.** *Superfluid-insulator transition in disordered boson systems*. Physical Review Letters, 67(17):2307 (1991).

[78] **Kühner T.D. and Monien H.** *Phases of the one-dimensional bose-hubbard model*. Physical Review B, 58(22):R14741 (1998).

[79] **Lanczos C.** *An iteration method for the solution of the eigenvalue problem of linear differential and integral operators*. Journal of research of the National Bureau of Standards, 45:225 (1950).

[80] **Laumann C., Scardicchio A. and Sondhi S.L.** *Cavity method for quantum spin glasses on the bethe lattice*. Physical Review B, 78(13):134424 (2008).

[81] **Löhneysen H.v., Rosch A., Vojta M. and Wölfle P.** *Fermi-liquid instabilities at magnetic quantum phase transitions*. Reviews of Modern Physics, 79(3):1015 (2007).

[82] **Lucretius Carus T.** *De rerum natura*. Liber VI (circa 55 BCE).

[83] **Manmana S.R., Muramatsu A. and Noack R.M.** *Time evolution of one-dimensional quantum many body systems*. AIP Conference Proceedings, 789(1):269 (2005).

[84] **Manousakis E.** *The spin-1/2 heisenberg antiferromagnet on a square lattice and its application to the cuprous oxides*. Reviews of Modern Physics., 63(1):1 (1991).

[85] **Martel P., Svensson E.C., Woods A.D.B., Sears V.F. and Cowley R.A.** *Neutron scattering from superfluid helium at large momentum transfers*. Journal of Low Temperature Physics, 23(3):285 (1976).

[86] **Mazzi G., Galli D. and Reatto L.** *Transverse phonon frequencies in bcc solid 4he*. AIP Conference Proceedings, 850:354 (2006).

[87] **McMillan W.L.** *Ground state of liquid he*^{4}. Physical Review, 138(2A):A442 (1965).

[88] **Menotti C., Trefzger C. and Lewenstein M.** *Metastable states of a gas of dipolar bosons in a 2d optical lattice*. Phys. Rev. Lett., 98:235301 (2007).

[89] **Mezard M. and Parisi G.** *The Bethe lattice spin glass revisited*. European Physics Journal B, 20(2):217 (2001).

[90] **Minkiewicz V.J., Kitchens T.A., Lipschultz F.P., Nathans R. and Shirane G.** *Phonon spectrum of hcp ^4he*. Physical Review, 174(1):267 (1968).

[91] **Minkiewicz V.J., Kitchens T.A., Shirane G. and Osgood E.B.** *Lattice excitations of the ^4he quantum solids*. Physical Review A, 8(3):1513 (1973).

[92] **Moroni S., Pederiva F., Fantoni S. and Boninsegni M.** *Equation of state of solid 3he*. Physical Review Letters, 84(12):2650 (2000).

[93] **Moroni S., Sarsa A., Fantoni S., Schmidt K.E. and Baroni S.** *Structure, rotational dynamics, and superfluidity of small ocs-doped he clusters*. Physical Review Letters, 90(14):143401 (2003).

[94] **Nagaoka Y.** *Ferromagnetism in a narrow, almost half-filled s band*. Physical Review, 147(1):392 (1966).

[95] **Oganesyan V. and Huse D.A.** *Localization of interacting fermions at high temperature*. Physical Review B, 75(15):155111 (2007).

[96] **Pal A. and Huse D.A.** *Many-body localization phase transition*. Physical Review B, 82(17):174411 (2010).

[97] **Parisi G.** *Statistical Field Theory*. Addison-Wesley, New York (1988).

[98] **Parisi G., Mezard M. and Virasoro M.A.** *Spin glass theory and beyond*. World Scientific, Singapore (1987).

[99] **Park H., Haule K., Marianetti C.A. and Kotliar G.** *Dynamical mean-field theory study of nagaoka ferromagnetism*. Physical Review B, 77(3):035107 (2008).

[100] **Pelleg O., Bossy J., Farhi E., Shay M., Sorkin V. and Polturak E.** *Anharmonic effects in neutron scattering studies ofâlattice excitations in bcc 4he*. Journal of Low Temperature Physics, 151(5):1164 (2008).

[101] **Petrosyan D., Schmidt B., Anglin J.R. and Fleischhauer M.** *Quantum liquid of repulsively bound pairs of particles in a lattice*. Physical Review A, 76(3):033606 (2007).

[102] **Pierleoni C. and Ceperley D.M.** *Computational methods in coupled electron-ion monte carlo simulations*. ChemPhysChem, 6(9):1872 (2005).

[103] **Pilati S., Bertaina G., Giorgini S. and Troyer M.** *Itinerant ferromagnetism of a repulsive atomic fermi gas: A quantum monte carlo study*. Physical Review Letters, 105(3):030405 (2010).

[104] **Planck M.** Sitzungsberichte der Preussischen Akademie der Wissenschaften zu Berlin (1917).

[105] **Polkovnikov A., Sengupta K., Silva A. and Vengalattore M.** *Colloquium: Nonequilibrium dynamics of closed interacting quantum systems*. Reviews of Modern Physics, 83:863 (2011).

[106] **Prokof'ev N.V., Svistunov B.V. and Tupitsyn I.S.** *"worm" algorithm in quantum monte carlo simulations*. Physics Letters A, 238(4-5):253 (1998).

[107] **Putikka W.O., Luchini M.U. and Ogata M.** *Ferromagnetism in the two-dimensional t-j model*. Physical Review Letters, 69(15):2288 (1992).

[108] **Reese R.A., Sinha S.K., Brun T.O. and Tilford C.R.** *Phonon dispersion relations for hcp he*^{4} *at a molar volume of 16 cm*^{3}. Physical Review A, (5):1688.

[109] **Rigol M., Dunjko V. and Olshanii M.** *Thermalization and its mechanism for generic isolated quantum systems*. Nature, 452 (2008).

[110] **Risken H.** *The Fokker-Planck Equation: Methods Of Solutions And Applications*. Springer Series in Synergetics. Springer (1989).

[111] **Roati G., D'Errico C., Fallani L., Fattori M., Fort C., Zaccanti M., Modugno G., Modugno M. and Inguscio M.** *Anderson localization of a non-interacting bose-einstein condensate*. Nature, 453(7197):895 (2008).

[112] **Rombouts S.M.A., Van Houcke K. and Pollet L.** *Loop updates for quantum monte carlo simulations in the canonical ensemble*. Physical Review Letters, 96(18):180603 (2006).

[113] **Rosch A., Rasch D., Binz B. and Vojta M.** *Metastable superfluidity of repulsive fermionic atoms in optical lattices*. Physical Review Letters, 101(26):265301 (2008).

[114] **Rousseau V.G.** *Directed update for the stochastic green function algorithm*. Physical Review E, 78(5):056707 (2008).

[115] **Rousseau V.G.** *Stochastic green function algorithm*. Physical Review E, 77(5):056705 (2008).

[116] **Roux G.** *Quenches in quantum many-body systems: One-dimensional bose-hubbard model reexamined*. Physical Review A, 79(2):021608 (2009).

[117] **Sandvik A.W.** *Stochastic series expansion method with operator-loop update*. Physical Review B, 59(22):R14157 (1999).

[118] **Sarsa A., Schmidt K.E. and Magro W.R.** *A path integral ground state method*. The Journal of Chemical Physics, 113(4):1366 (2000).

[119] **Schiró M. and Fabrizio M.** *Time-dependent mean field theory for quench dynamics in correlated electron systems*. Physical Review Letters, 105(7):076401 (2010).

[120] **Schmidt K. and Kalos M.** *Monte Carlo Methods in Statistical Physics*. Springer, Berlin (1984).

[121] **Schmidt K.E., Niyaz P., Vaught A. and Lee M.A.** *Green's function monte carlo method with exact imaginary-time propagation*. Physical Review E, 71(1):016707 (2005).

[122] **Schmunk R.E., Brugger R.M., Randolph P.D. and Strong K.A.** *Lattice dynamics of beryllium*. Physical Review, 128(2):562 (1962).

[123] **Sciolla B. and Biroli G.** *Quantum quenches and off-equilibrium dynamical transition in the infinite-dimensional bose-hubbard model*. Physical Review Letters, 105(22):220401 (2010).

[124] **Sears V.F., Svensson E.C., Martel P. and Woods A.D.B.** *Neutron-scattering determination of the momentum distribution and the condensate fraction in liquid ^{4}He*. Physical Review Letters, 49(4):279 (1982).

[125] **Semerjian G., Tarzia M. and Zamponi F.** *Exact solution of the bose-hubbard model on the bethe lattice*. Physical Review B, 80(1):014524 (2009).

[126] **Sengupta P., Pryadko L.P., Alet F., Troyer M. and Schmid G.** *Supersolids versus phase separation in two-dimensional lattice bosons*. Physical Review Letters, 94(20):207202 (2005).

[127] **Shastry B.S., Krishnamurthy H.R. and Anderson P.W.** *Instability of the nagaoka ferromagnetic state of the $u = \infty$ hubbard model*. Physical Review B, 41(4):2375 (1990).

[128] **Sorella S.** *Wave function optimization in the variational monte carlo method*. Physical Review B, 71(24):241103 (2005).

[129] **Sorella S.** *Auxiliary-field based simulations of the fermionic hubbard model* (2010). Private communication.

[130] **Sorella S. and Capriotti L.** *Green function monte carlo with stochastic reconfiguration: An effective remedy for the sign problem*. Physical Review B, 61:2599 (2000).

[131] **Sorkin V., Polturak E. and Adler J.** *Path-integral monte carlo study of phonons in the bcc phase of ^{4}He*. Physical Review B, 71(21):214304 (2005).

[132] **Sorkin V., Polturak E. and Adler J.** *Path-integral monte carlo study of phonons in the bcc phase of ^{3}He*. Journal of Low Temperature Physics, 143(3):141 (2006).

[133] **Stoner E.C.** Reports on Progress in Physics, 11(11):43 (1948).

[134] **Syljuasen O.F.** *Plaquette phase of the square-lattice quantum dimer model: Quantum monte carlo calculations*. Physical Review B, 73(24):245105 (2006).

[135] **Syljuåsen O.F. and Sandvik A.W.** *Quantum monte carlo with directed loops*. Physical Review E, 66(4):046701 (2002).

[136] **Tam K.M., Geraedts S., Inglis S., Gingras M.J.P. and Melko R.G.** *Superglass phase of interacting bosons*. Physical Review Letters, 104(21):215301 (2010).

[137] **Tanatar B., Talbot E.F. and Glyde H.R.** *Dynamics of quantum liquids at high momentum*. Physical Review B, 36(16):8376 (1987).

[138] **Tarzia M. and Biroli G.** *The valence bond glass phase*. Europhysics Letters, 82:67008 (2008).

[139] **Tayo B. and Sorella S.** *Exact jastrow-slater wave function for the one-dimensional luttinger model*. Phys. Rev. B, 78:115117 (2008).

[140] **ten Haaf D.F.B., van Bemmel H.J.M., van Leeuwen J.M.J., van Saarloos W. and Ceperley D.M.** *Proof for an upper bound in fixed-node monte carlo for lattice fermions*. Physical Review B, 51(19):13039 (1995).

[141] **Tocchio L.F., Becca F., Parola A. and Sorella S.** *Role of backflow correlations for the nonmagnetic phase of the t– t' hubbard model*. Physical Review B, 78(4):041101 (2008).

[142] **Trotzky S., Chen Y.A., Flesch A., McCulloch I., Schollwöck U., Eisert J. and Bloch I.** *Probing the relaxation towards equilibrium in an isolated strongly correlated 1d bose gas*. arXiv:1101.2659 (2011).

[143] **Umrigar C.J., Toulouse J., Filippi C., Sorella S. and Hennig R.G.** *Alleviation of the fermion-sign problem by optimization of many-body wave functions*. Physical Review Letters, 98:110201 (2007).

[144] **Van Hove L.** *Correlations in space and time and born approximation scattering in systems of interacting particles*. Physical Review, 95(1):249 (1954).

[145] **Vidal G.** *Efficient simulation of one-dimensional quantum many-body systems*. Physical Review Letters, 93(4):040502 (2004).

[146] **von Neumann J.** *Beweis des ergodensatzes und des h-theorems in der neuen mechanik*. Zeitschrift für Physik, 57 (1929).

[147] **Wall M. et al.** *Time-evolving block decimation open source code*. URL `http://physics.mines.edu/downloads/software/tebd/`.

[148] **Wessel S. and Troyer M.** *Supersolid hard-core bosons on the triangular lattice*. Physical Review Letters, 95(12):127205 (2005).

[149] **White S.R. and Feiguin A.E.** *Real-time evolution using the density matrix renormalization group*. Physical Review Letters, 93(7):076401 (2004).

[150] **Whitehead R.R. and Watt A.** *On the lanczos method and the method of moments*. Journal of Physics G: Nuclear Physics, 4(6):835 (1978).

[151] **Wurth P. and Muller-Hartmann E.** *Ferromagnetism in the hubbard model: Spin waves and instability of the nagaoka state*. Annalen der Physik, 507(2):144 (1995).

[152] **Zinn-Justin J.** *Quantum Field Theory and Critical Phenomena*. Oxford University Press, New York (2002).

Appendix A
Directed Updates Probabilities And Efficiency Of The Lattice Reptation Monte Carlo

A.1 Derivation of the Probabilities for the Directed-Update Scheme

In this Appendix we give a detailed derivation of the probabilities for the directed updates. The detailed balance condition guarantees that the given probability distribution $\Pi^\tau(\mathbf{X})$ is sampled if transitions from an initial state $\mathbf{X}^k$ to a final state $\mathbf{X}^{k+s}$ differing for s intermediate updates are accepted according to:

$$A^s = \min\left\{1, \frac{\Pi^\tau(\mathbf{X}^{k+s})}{\Pi^\tau(\mathbf{X}^k)} \frac{\mathcal{T}^s(\mathbf{X}^{k+s} \to \mathbf{X}^k)}{\mathcal{T}^s(\mathbf{X}^k \to \mathbf{X}^{k+s})}\right\}, \tag{A.1.1}$$

$\mathcal{T}^s$ being the overall transition probability between the two states. Let us first consider the case when $s = 1$ and fix the right direction $d = R$ (a similar derivation can be obtained for $d = L$). In this case, the transition probability from the initial state to the final state reads

$$\begin{aligned}\mathcal{T}^1(\mathbf{X}^k \to \mathbf{X}^{k+1}) = P\left(R \,|\, \mathbf{X}^k\right) \times R^\delta(x^k_{2M} \to x^{k+1}_{2M}) \times \\ \times \left[1 - K(R\,,\, \mathbf{X}^{k+1})\right],\end{aligned} \tag{A.1.2}$$

namely, it is the product of the probability of having chosen the right direction, times the transition probability for the new tail of the reptile, times the probability of stopping the updates after one intermediate step. The inverse transition probability instead reads

$$\begin{aligned}\mathcal{T}^1(\mathbf{X}^{k+1} \to \mathbf{X}^k) = P\left(L \,|\, \mathbf{X}^{k+1}\right) \times R^\delta(x^{k+1}_0 \to x^k_0) \times \\ \times \left[1 - K(L\,,\, \mathbf{X}^k)\right],\end{aligned} \tag{A.1.3}$$

which can be obtained reversing the time directions and considering transitions from the head of the reptile instead that from the tail. Therefore, the acceptance factor reads as

$$
\begin{aligned}
A^1 = \min \Bigg\{ 1, \frac{1 - K(L\,,\, \mathbf{X}^k)}{P\,(R\,|\,\mathbf{X}^k)} \times \\
\times \frac{w(x_{2M-1}^{k+1})}{w(x_1^k)} \times \frac{P\left(L\,|\,\mathbf{X}^{k+1}\right)}{1 - K(R\,,\, \mathbf{X}^{k+1})} \Bigg\} .
\end{aligned}
\tag{A.1.4}
$$

For two intermediate transitions instead the transition probabilities are

$$
\begin{aligned}
\mathcal{T}^2(\mathbf{X}^k \to \mathbf{X}^{k+2}) = P\left(R\,|\,\mathbf{X}^k\right) \times R^\delta(x_{2M}^k \to x_{2M}^{k+1}) \times \\
\times K\left(R\,,\, \mathbf{X}^{k+1}\right) \times R^\delta(x_{2M}^{k+1} \to x_{2M}^{k+2}) \times \\
\times \left[1 - K\left(R\,,\, \mathbf{X}^{k+2}\right)\right] ,
\end{aligned}
\tag{A.1.5}
$$

and

$$
\begin{aligned}
\mathcal{T}^2(\mathbf{X}^{k+2} \to \mathbf{X}^k) = P\left(L\,|\,\mathbf{X}^{k+2}\right) \times R^\delta(x_0^{k+2} \to x_0^{k+1}) \times \\
\times K\left(L\,,\, \mathbf{X}^{k+1}\right) \times R^\delta(x_0^{k+1} \to x_0^k) \times \\
\times \left[1 - K\left(L\,,\, \mathbf{X}^k\right)\right] ,
\end{aligned}
\tag{A.1.6}
$$

leading to the acceptance factor

$$
\begin{aligned}
A^2 = \min \Bigg\{ 1, \frac{1 - K\left(L\,,\, \mathbf{X}^k\right)}{P\,(R\,|\,\mathbf{X}^k)} \times \frac{K\left(L\,,\, \mathbf{X}^{k+1}\right)}{K\,(R\,,\, \mathbf{X}^{k+1})} \times \\
\times \frac{w(x_{2M-1}^{k+1})}{w(x_1^{k+1})} \times \frac{P\left(L\,|\,\mathbf{X}^{k+2}\right)}{1 - K\,(R\,,\, \mathbf{X}^{k+2})} \times \frac{w(x_{2M-1}^{k+2})}{w(x_1^k)} \Bigg\} .
\end{aligned}
\tag{A.1.7}
$$

The generalization to generic s intermediate steps is straightforward and can be written as

$$
\begin{aligned}
A^s = \min \Bigg\{ 1, \frac{1 - K\left(L\,,\, \mathbf{X}^k\right)}{P\,(R\,|\,\mathbf{X}^k)} \times \frac{P\left(L\,|\,\mathbf{X}^{k+s}\right)}{1 - K\,(R\,,\, \mathbf{X}^{k+s})} \times \\
\times \frac{w(x_{2M-1}^{k+s})}{w(x_1^k)} \times \left[\prod_{l=1}^{s-1} \frac{K\left(L\,,\, \mathbf{X}^{k+1}\right)}{K\,(R\,,\, \mathbf{X}^{k+1})} \times \frac{w(x_{2M-1}^{k+l})}{w(x_1^{k+l})} \right] \Bigg\} .
\end{aligned}
\tag{A.1.8}
$$

To find a simple solution for the unknown probabilities, we first impose a cancellation for the intermediate acceptance factors, namely

$$
\frac{K\,(L\,,\, \mathbf{X})}{K\,(R\,,\, \mathbf{X})} = \frac{w(x_1)}{w(x_{2M-1})} ,
\tag{A.1.9}
$$

this condition is satisfied by Eqs. (2.2.11) and (2.2.12). Then, we notice that the acceptance factor can be written only in terms of the final and the initial states as

$$A^s = \min\left\{1, \frac{q(L\,,\,\mathbf{X}^{k+s})}{q(R\,,\,\mathbf{X}^k)}\right\}. \tag{A.1.10}$$

Further, we can impose the two factors q to be independent on the direction, i.e., the condition $q(L\,,\,\mathbf{X}) = q(R\,,\,\mathbf{X}) = q(\mathbf{X})$, which is satisfied if

$$\begin{aligned}\frac{P\,(L\,|\,\mathbf{X})}{1 - K\,(R\,,\,\mathbf{X})} \times w(x_{2M-1}) = \\ = \frac{P\,(R\,|\,\mathbf{X})}{1 - K\,(L\,,\,\mathbf{X})} \times w(x_1).\end{aligned} \tag{A.1.11}$$

Since the two time directions are mutually exclusive, it is also true that $P\,(L\,|\,\mathbf{X}) + P\,(R\,|\,\mathbf{X}) = 1$, which allows us to solve Eq. (A.1.11) and obtain Eqs. (2.2.8) and (2.2.9). The same reasoning can be repeated for the left direction and, due to imposed homogeneity for the probabilities, it can be checked that the detailed balance is satisfied for the left direction too.

A.2 Bounce Algorithm, Directed Updates, and Efficiency

In this Appendix we comment on the relationship between the directed-update scheme and the bounce algorithm. If $\alpha = 1$ is taken in Eqs. (2.2.11) and (2.2.12), then after s updates along the direction d, at the end of the Markov step $P(d\,|\,\mathbf{X}^{k+s}) = 0$, i.e., the next Markov step will be taken in the opposite direction, just like the bounce algorithm. Although the two algorithms are similar in this particular limit, there is an important difference which eventually leads to a different computational efficiency. In order to elucidate this point and to show the α-dependence of the efficiency of the directed updates, we have done a systematic comparison of the two algorithms.

In particular, we have compared the efficiency of the directed updates with the bounce algorithm for a one-dimensional Heisenberg model. The computational efficiency is generally defined as

$$\mathcal{E} = \frac{1}{\sigma_O^2 T}, \tag{A.2.1}$$

where σ_O^2 is the square of the statistical error associated to a given observable after a given computational time T. In Fig. A.2.1, we show the ratio between the directed-update scheme efficiency over the bounce algorithm efficiency, for the measurement of the ground-state energy of a one-dimensional chain.

We notice that the two sampling schemes have comparable performances, being both based on a similar approach. As anticipated, it clearly emerges from Fig. A.2.1 that the two algorithms do not have exactly the same behavior at $\alpha = 1$, the maximum efficiency of the directed updates being reached for lower values of α. This feature is due to the fact that when α is very

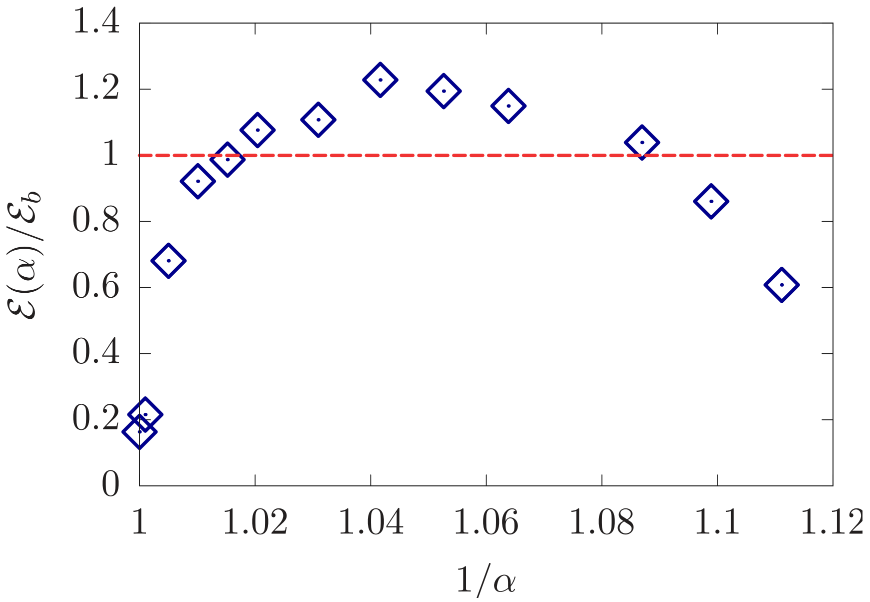

Fig. A.2.1 Relative efficiency of the directed update scheme and the bounce algorithm. The measured quantity is the ground-state energy of the one-dimensional Heisenberg model on a chain of size $L = 80$ sites.

close to its saturation value, then a single Markov step can consist of a conspicuous number of individual "sliding moves". Even if this situation leads to a fast decorrelation of configurations it also leads to a rarefaction of the possibility to measure the desired observables, which can eventually take place only at the end of the Markov step and not during the individual moves. This leads to a worse efficiency if compared to the bounce algorithm, where measurements can be in principle done after every sliding move.

In conclusion, the performances of the two algorithms are very close, although some advantages may arise from the use of the directed-updates. We further notice that the purely Markovian approach discussed in Chapter 2 could be slightly more efficient in cases where the number of rejected configurations by the bounce algorithm is substantial whereas *all* the generated configurations are accepted in the directed update scheme.